Nanostructures for Vacuum Optoelectronic Engineering

by

Yujia Yang

B.S., Zhejiang University (2011)
S.M., Massachusetts Institute of Technology (2013)

Submitted to the Department of Electrical Engineering and Computer Science
in partial fulfillment of the requirements for the degree of

Doctor of Philosophy in Electrical Engineering

at the

MASSACHUSETTS INSTITUTE OF TECHNOLOGY

September 2019

Author……………………………………………………………….
Department of Electrical Engineering and Computer Science
August 30, 2019

Certified by …………………………………………………………
Karl K. Berggren
Professor of Electrical Engineering and Computer Science
Thesis Supervisor

Accepted by…………………………………………………………
Leslie A. Kolodziejski
Professor of Electrical Engineering and Computer Science
Chair, Department Committee on Graduate Students

Nanostructures for Vacuum Optoelectronic Engineering

by

Yujia Yang

Submitted to the Department of Electrical Engineering and Computer Science
on August 30, 2019, in partial fulfillment of the
requirements for the degree of
Doctor of Philosophy in Electrical Engineering

Abstract

The interaction between free electrons and electromagnetic fields enables a wide range of scientific research and technological applications, ranging from electronic, optoelectronic, and microwave vacuum tubes, to electron beams for material processing and analysis, particle accelerators, and free-electron radiation sources. However, for most free-electron-based devices, the compactness, chip-scale integration, ultrafast temporal response, and quantum state manipulation remain impractical or unexplored. Recent advances in nanofabrication have pushed the boundary and extended the operating paradigm of free-electron devices. In this thesis, I will investigate the interplay between free electrons and optical frequency electromagnetic fields mediated by nanostructures. I will show high-yield, ultrafast, surface-plasmon-enhanced photoelectron emitters. With the photoemission driven by the optical field, this technology enables the detection of carrier-envelope-phase of ultrafast optical pulses with solid-state nanoantenna arrays integrated on a chip. Additionally, I will show free-electron-driven plasmon and photon emission from nanophotonic structures, which leads to the characterization of plasmonic nanostructures and the development of nanoscale tunable free-electron light sources. Furthermore, I will show the manipulation of free electrons with nanostructured phase plates, and propose an electron beam splitter design based on the quantum interaction-free measurement and quantum Zeno effect. The work demonstrated in this thesis presents a step towards chip-integrated petahertz optoelectronic devices, compact tunable free-electron radiation sources, as well as quantum devices for free electrons.

Thesis Supervisor: Karl K. Berggren

Title: Professor of Electrical Engineering and Computer Science

Acknowledgments

The work performed in my graduate school career and presented in this thesis was made possible by the support, advice, and contributions of many people. In particular, I would like to thank:

My thesis supervisor, Professor Karl K. Berggren, for his extensive advice and support. His enthusiasm for science, disciplines in academic research, and broad knowledge base has always inspired me.

Professor Dirk Englund, Professor Marin Soljačić, and Dr. Phillip "Donnie" Keathley, for agreeing to be on my thesis committee, and giving me great advice on my work. They have also helped me to expand my knowledge in the area of optics and photonics.

Professor Franz Kärtner and Professor Pieter Kruit, for many helpful guidance and suggestions on our collaborative work.

Dr. Richard Hobbs, Dr. Vitor Manfrinato, Dr. William Putnam, Dr. Chung-Soo Kim, and Dr. Ido Kaminer, for being great mentors and collaborators during my graduate training.

Akshay Agarwal, Navid Abedzadeh, Marco Turchetti, Alberto Nardi, John Simonaitis, Owen Medeiros, Dr. Mina Bionta, Felix Ritzkowsky, Mengjie Zheng, Sarah Goodman, for being great colleagues and giving me a lot of help.

Dr. Andrew Dane, Dr. Di Zhu, Dr. Reza Baghdadi, Dr. Ilya Charaev, Dr. Faraz Najafi, Dr. Qing-Yuan Zhao, Dr. Kristen Sunter, Dr. Adam McCaughan, Marco Colangelo, Emily Toomey, Ashley Qu, Brenden Butters, Murat Onen, for being great "cool" colleagues and teaching me about superconducting single photon detectors.

Many other past and present members of the Quantum Nanostructures and Nanofabrication group.

Charles Roques-Carmes, Aviram Massuda, Yi Yang, Dr. Steven Kooi, Dr. Arya Fallahi, Dr. Lihua Zhang, Dr. Ren-Jye Shiue, Fan Meng, and many collaborators outside our group. A lot of the work would not be possible without their help.

Mark Mondol, Jim Daley, and Tim Savas, for maintaining great nanofabrication facilities that enabled almost all the nanostructures and devices presented in this thesis.

And finally, my mother and father, who have been very supportive in the past years. Since I was a kid, I have taken a lot of inspiration from them and their engineering background. They have encouraged me to pursue my career goals, and given me valuable advice on personal and professional development.

Contents

List of Figures

Chapter 1

Introduction

The interaction between free electrons and electromagnetic fields enables a wide range of scientific research and technological applications. Vacuum tubes are devices based on the generation and control of free-electron currents in a high vacuum between electrodes [1]. Vacuum tube electronic switches enabled the world's first electronic computer ENIAC [2]. Photomultiplier tubes (PMTs) are used for light detection in the visible and ultraviolet spectral range, with a high gain, low noise, and fast response time [3]. Cathode-ray tubes (CRTs) are used to display images in monitors and oscilloscopes [4]. Microwave tubes, including magnetrons, klystrons, and traveling wave tubes, can generate and amplify microwaves and are commonly used in high-power applications such as radar transmitters, satellite communication, particle accelerators, and microwave ovens [5]. Additionally, free-electron beams formed by electric and magnetic fields enable a variety of material processing and analysis technologies including electron-beam furnaces [6], welding [7], lithography [8], and microscopy [9], as well as particle accelerators for particle physics and free-electron radiation sources [10].

There are several problems associated with conventional free-electron-based devices. Firstly, compared with semiconductor devices, free-electron devices are bulky and require a high vacuum, and hence are incompatible with cost-effective mass-fabrication processes, and less suitable for construction of compact systems. Additionally, most free-electron devices rely on thermionic and cold field emission sources, as well as single-photon-emission photocathodes, which are unable to achieve ultrafast, sub-optical-cycle response time when driven by intense ultrafast optical pulses. Furthermore, most microwave tubes operate in the mm-wave and microwave frequency range, while optical wave generation typically requires high-energy electrons at large synchrotron facilities. Lastly, most free-electron devices treat electrons as point-like particles with very few exceptions such as phase-contrast transmission electron microscopy, while the wave nature and quantum properties of electrons are neglected.

The work discussed in this thesis focuses on the interplay between free electrons and optical-frequency electromagnetic fields mediated by nanostructures. Relying on recent advances in nanofabrication, nanoscale structures and devices can be made from various materials. Nanostructures enable the study of the interactions between free electrons and optical fields at the nanoscale. Nanoscale, solid-state vacuum optoelectronic devices can also benefit from small footprint, low cost, and mass-production like their semiconductor counterparts. Furthermore, nanostructures can push the boundaries of free-electron devices, such as enabling the operation in ambient conditions, and extending the operating frequency from microwaves to the optical spectral range. Lastly, due to the short de Broglie wavelength of electrons, nanostructures are necessary to study the wave nature and quantum properties of electrons.

Three main topics will be discussed in this thesis: (i) ultrafast photoelectron emission from nanostructures; (ii) free-electron-driven plasmon and photon emission from nanostructures; and (iii) manipulation of free electrons with nanostructures. These topics fall into the categories of light-to-free-electron conversion, free-electron-to-light conversion, and control of free electrons, respectively.

1.1 Outline of this thesis

This thesis will discuss the three main topics mentioned above, each within two chapters.

Ultrafast photoelectron emission from nanostructures will be discussed in Chapter 2 and Chapter 3. Chapter 2 describes high-yield, ultrafast, surface-plasmon-enhanced optical field emitters. Ultrafast laser induced photoelectron emission is improved by nanostructured emitters supporting surface plasmon resonance. The optical field at the emitter surface is enhanced by the resonance, leading to an improved quantum efficiency and charge yield. This efficient photocathode can be used in free-electron laser (FEL) development. The ultrafast optical-field-driven photoemission is also utilized in solid-state vacuum optoelectronic devices beyond photocathodes. Chapter 3 describes carrier-envelop phase detection with on-chip electrically connected nanoantenna arrays. Photoemission from plasmonic nanoantennas is used to resolve the optical field of the driving laser. By reading out the electronic signal from a connected nanoantenna array, the carrier-envelop phase of the ultrafast laser is detected. This ultrafast nanoscale device presents a step towards chip-scale integrated, optical-field-driven optoelectronic devices operating in the petahertz (PHz) regime.

Free-electron-driven plasmon and photon emission from nanostructures will be discussed in Chapter 4 and Chapter 5. Chapter 4 describes electron-energy loss study of plasmonic modes in aluminum nanodisks. Electron-energy-loss spectroscopy is used to probe the plasmonic properties of nanostructures, based on electron-beam induced plasmon emission. Various plasmonic modes of lithographically defined aluminum nanodisks are experimentally measured and theoretically investigated. The aluminum nanodisks support tunable surface plasmon resonance in the ultraviolet, enabling applications in this spectral range. Besides spectroscopic techniques, the electron-beam induced plasmon or photon emission can be considered as an electromagnetic radiation source. Chapter 5 describes polarization-tunable light emission from free-electron-driven metasurfaces. In line with the development of compact free-electron light sources, nanophotonic metasurfaces are shown to generate light emission in the form of Smith-Purcell radiation when driven by free electrons. The polarization of the emitted light is tuned by the metasurface design, in contrast to the conventional grating-based Smith-Purcell radiation, of which the polarization is predetermined by the electron-beam direction.

Manipulation of free electrons with nanostructures will be discussed in Chapter 6 and Chapter 7. Chapter 6 describes nanostructured-membrane electron phase plates. Nanofabricated material phase plates impose designed phase modulations onto electron beams. Large-area mesh-gratings in a silicon nitride film are fabricated with electron beam lithography and reactive-ion-etching. The phase plates diffract electron beams with various energies and show a tunable diffraction efficiency. Electron phase plates can be used for beam shaping, wavefront engineering, as well as beam splitting. Chapter 7 theoretically describes efficient two-port electron beam splitters via quantum interaction-free measurement. By combining an electron phase grating and an electron resonator, a two-port directional-coupler-like electron beam splitter is achieved. The efficiency of the beam splitter is made close to unity by using quantum interaction-free measurement and quantum Zeno effect.

Finally, some conclusions and outlook will be presented in Chapter 8.

Chapter 2

High-yield, ultrafast, surface-plasmon-enhanced optical field emitters

Ultrafast light-matter interactions enable the study and control of electron dynamics in atomic, molecular, and solid materials. Ultrafast optical pulses can induce photoelectron emission from materials, such as metallic photocathodes, with applications in ultrafast electron microscopy and diffraction, as well as light sources based on free-electron radiation. Metallic photocathodes have a fast response time, but suffer from a low quantum efficiency. This problem can be solved by invoking surface plasmon resonance in metal nanostructures to enhance the optical field. In this chapter, we demonstrate the design, fabrication and characterization of high-repetition rate, ultrafast, surface-plasmon-enhanced Au nanorod optical field emitter arrays. We tune the nanorod surface plasmon resonance to match with the driving laser wavelength and optimize the substrate to obtain the desired near field profile. We also investigate the effects of surface plasmon damping in Au nanorods, induced by metallic interface layers at the substrate, on near-field enhancement and electron emission. The efficient, bright, and ultrafast optical field emitter arrays may facilitate the development of efficient and bright free-electron laser (FEL). Part of the content in this chapter was derived from the work in [11].

This chapter is organized as follows. In Section 2.1, we introduce the surface-plasmon-enhanced photocathodes. In Section 2.2, we describe the fabrication of plasmonic Au nanorod arrays as optical field emitters. In Section 2.3, we discuss the design and electromagnetic simulation of the nanorod arrays. In Section 2.4, we present the spectroscopic characterization of the nanorod arrays. In Section 2.5, we show the photoelectron emission measurement from the nanorod arrays. Finally, Section 2.6 summarizes our results.

2.1 Surface-plasmon-enhanced photocathodes

Ultrafast optical pulses can induce photoelectron emission from materials, which enables high-brightness, pulsed photocathodes, or optical field emitters, with applications in ultrafast electron microscopy and diffraction [12–15], as well as light sources based on free-electron radiation [16–18]. Metallic photocathodes have a fast response time and are relatively insensitive to contaminations. These features make metallic photocathodes ideal candidates for applications in which short photoelectron pulses induced by ultrafast laser pulses are required. Photoelectron emission induced by multiphoton absorption in metals is of particular interest for developing emitter arrays to inject high-brightness electron beams into accelerators for FEL development. Compared to photoemission induced by single-photon absorption, the multiphoton emission does not require UV lasers or crystal-based harmonic generation. The multiphoton character also leads to a more localized electron-emission site compared to a single-photon process, and is desirable as a low emittance electron source. However, compared to semiconductor and alkali halide photocathodes, metallic photocathodes suffer from a low quantum efficiency, especially when a multiphoton process is required. By using nanostructured metals supporting surface plasmon resonance, the optical near field can be enhanced, leading to an improved photocathode efficiency.

Nanostructures exhibiting surface plasmon resonance have been investigated for use in a variety of applications. The local enhancement of optical fields by the collective oscillation of electrons (plasmons) in such particles when illuminated at resonant wavelengths, allows their use for spectroscopy [19,20], imaging [21], metamaterial [22–24], sensor [25,26], nanolithography [27], and photocathode [28] applications. Prior work on photoelectron emission from plasmonic nanoparticles primarily focused on the electron energy spectra [28,29]. Recent works have shown enhanced photocathode efficiency by surface plasmon excitations in nano-hole arrays on Cu surfaces [30] and dielectric grooves in Al and Au [31].

In this chapter we consider the use of plasmonic nanoparticle arrays as high-brightness photoelectron emitters. We fabricated Au nanorods with sub-20 nm critical dimensions, leading to a great localization of the electron-emission site. The localized emission allows for nanoscale density modulation in the electron beam, which is favored in certain FEL applications [18]. We demonstrated photoelectron emission from the multiphoton-absorption regime to the optical-field-driven regime. We also investigated the effect of the dielectric environment, including the substrate and the adhesion-promotion layer used in device fabrication, on the plasmonic resonance and photoelectron emission. The high-yield ultrafast optical field emitter arrays could find applications in the development of efficient and bright FEL.

2.2 Sample fabrication

Nanorod samples were fabricated on either sapphire or Si (n-type, 1-10 Ω·cm) chips. The transparent sapphire substrate was chosen to facilitate transmission measurement. A 50-200 nm thick indium tin oxide (ITO) film was sputtered on the substrate as the cathode electrode and its low index was favored by photocathode application. This conducting film also solved the charging problem in electron beam lithography on an insulating substrate such as sapphire. Then, ~70 nm

PMMA electron-beam resist was spin-coated on the substrates and soft-baked at 180 °C for 2 min. Nanorod array patterns were defined by electron beam lithography with an Elionix F-125 EBL system. The accelerating voltage was 125 kV, electron beam current was 0.5 or 1 nA, and typical exposure dose was ~800 e^-/nm^2. Exposed PMMA was developed in 3:1 IPA:MIBK mixture at 0 °C for 30 s with constant agitation and blow dried by N_2 gas. We used low temperature development to improve the resolution of electron beam lithography with a positive-tone resist. Metals were then deposited via electron-beam evaporation. For Au nanorod arrays with a Ti adhesion layer, 3 nm Ti and 20 nm Au were evaporated at a rate of 0.5 $Ås^{-1}$ in the vacuum chamber (~10^{-6} mbar); while for Au nanorod arrays without an adhesion layer, 20 nm Au was evaporated at a slower rate of 0.1 $Ås^{-1}$ in order to facilitate the adhesion between Au nanorods and the substrate when an adhesion layer is absent. Metal lift-off was performed in n-methylpyrrolidone (NMP) at 55 °C for ~60 min during which the samples were gently rinsed with flowing NMP. A mild temperature and longer than usual lift-off time was used to avoid sonication as it was shown to create vacancy defects in the arrays with an adhesion layer, and destroy almost the entire array without an adhesion layer. The purpose of gentle rinsing was to peel off the metal layer on top of the resist while keeping the nanorods intact. After lift-off, the samples were rinsed with acetone and isopropyl alcohol. Gentle O_2 plasma ashing (50 W, 60 s) was applied to remove residual resist and solvents just before photoelectron emission measurements. No damage on Au nanorods by O_2 plasma was observed in microscopic images and photoemission data.

Figure 2.1 shows the SEM images of fabricated Au nanorod arrays. The nanorod array pitch was 200 nm for most samples. The nanorod width ranged from 10 nm to 20 nm by adjusting the EBL dose, and the nanorod length was varied from 60 nm to 85 nm to tune the surface plasmon resonance wavelength. The nanorod arrays with a Ti adhesion (Figure 2.1a) and without an adhesion layer (Figure 2.1b) both had a unity device yield. When an adhesion layer was absent, the nanorods showed a larger line roughness (Figure 2.1b), potentially caused by the removal of some Au crystal grains during liftoff due to insufficient adhesion to the substrate. Nevertheless, with our fabrication process, nearly all the nanorods yielded without an adhesion layer (Figure 2.1c).

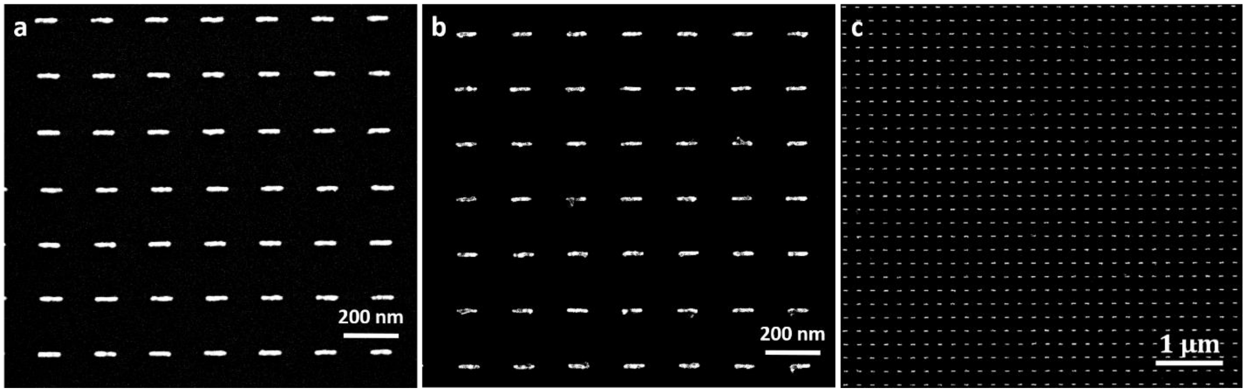

Figure 2.1. SEM images of Au nanorod arrays. (a) Au nanorods with a Ti adhesion layer. (b) Au nanorods without an adhesion layer. (c) A low-magnification image of Au nanorods without an adhesion layer.

2.3 Electromagnetic simulation

Optical responses of the Au nanorod arrays were simulated with finite element method (FEM) electromagnetic solver (*COMSOL Multiphysics*). The calculation domain was a box encapsulating a single Au nanorod, and periodic boundary condition was applied to simulate an array of nanorods. The simulated nanorod had a rectangular transverse cross section and two hemisphere end caps. Sharp edges at the vacuum side were rounded with a 3 nm curvature to avoid singularities in the calculation as well as to better mimic the fabricated structure. The nanorod length, width, and thickness were varied. Different substrate materials were considered: Si, ITO, and ITO thin film on sapphire. To model the adhesion layer, a thin Ti layer was added in between the nanorod and the substrate. The Ti layer thickness was 3 nm unless otherwise specified. The illumination light was incident normally from the top. The light was linearly polarized along the long-axis of the nanorod unless otherwise specified. The light wavelength was varied from 500 nm to 1000 nm, including the excitation wavelength (800 nm) used in experiments. A perfect matched layer (PML) was used to absorb outgoing electromagnetic waves. Boundaries with periodic condition were identically meshed with triangular element with a dimension smaller than one tenth the boundary dimension. The PML was sweeping-meshed to reduce computation complexity. Other objects within the calculation domain were adaptively meshed with free tetrahedral elements of which the sizes were kept small enough so that each edge of the object contained at least twenty elements. The meshing was even finer at the edge curvature and the adhesion layer when present. The optical properties of Au and Ti were taken from the work by Johnson and Christy [32] describing optical constants of the metals fabricated under similar conditions to ours (vacuum-evaporated polycrystalline thin films). The optical constant of ITO was taken from SOPRA database[1]. As the optical constant of ITO could vary due to thin film deposition conditions, we designed and fabricated Au nanorods with various lengths to tune the surface plasmon resonance so that it could match the excitation wavelength.

Figure 2.2 shows the electromagnetic simulation of Au nanorods on different substrates. A 3-nm-thick Ti adhesion layer was included in the simulation. For Au nanorods on the ITO substrate, the field enhancement spectra (Figure 2.2a) show two peaks corresponding to the transverse and longitudinal surface plasmon modes of the nanorod [33]. The transverse surface plasmon mode is centered at ~530 nm, while the longitudinal surface plasmon mode is tunable by changing the

---

[1] Optical properties of coating materials from Sopra S.A., http://www.sspectra.com/sopra.html.

nanorod length. The optical near-field profiles for nanorods on the ITO and Si substrates, under the illumination of 800 nm wavelength light, are shown in Figure 2.2b&c. The 800-nm-wavelength was chosen as it matched with the central wavelength of the Ti:sapphire laser used in photoemission measurements. As expected from the field enhancement spectra, Au nanorods on the ITO substrate show a stronger field enhancement. Si substrate also induces a stronger field localization at the nanorod-substrate interface, due to the high refractive index of Si. For Au nanorods on the Si substrate, the longitudinal mode is strongly suppressed, due to a combined effect of, Si-substrate-induced field localization at the interface, and Ti-layer-induced damping discussed later in this chapter.

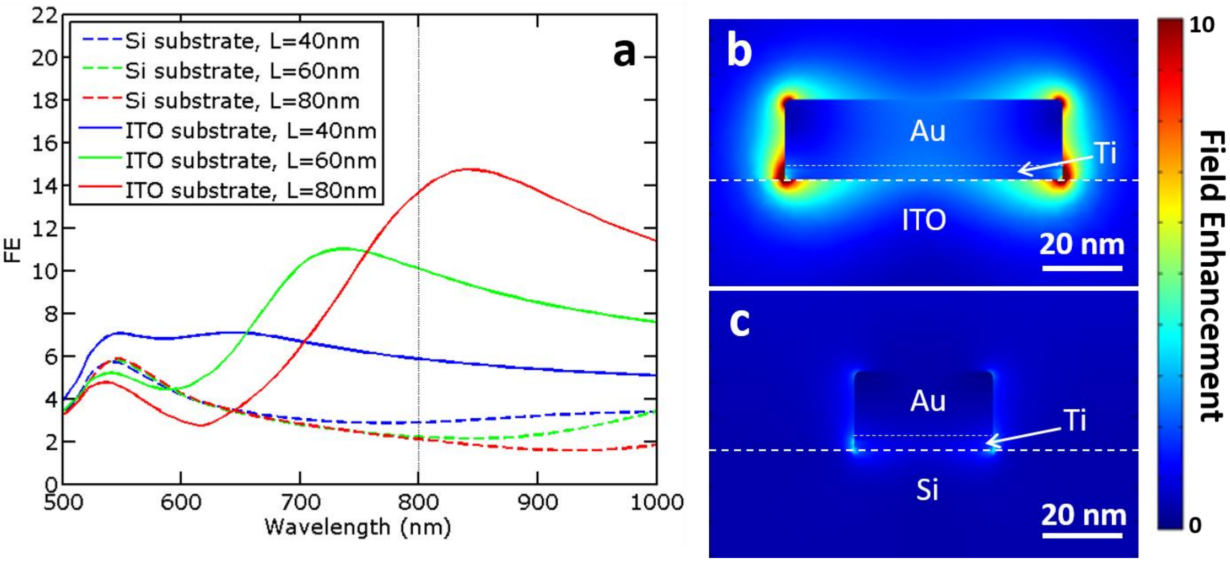

Figure 2.2. Simulated optical response of Au nanorods on different substrates. (a) Field enhancement spectra of Au nanorods with various lengths (40 nm, 60 nm, 80 nm) on Si or ITO substrate. (b) Near-field profile of Au nanorod with 80 nm length on ITO substrate illuminated with 800 nm wavelength light. (c) Near-field profile of Au nanorod with 40 nm length on Si substrate illuminated with 800 nm wavelength light. Scale bar: 20 nm.

2.4 Optical spectroscopy

The Au nanorod arrays were characterized optically with UV-Vis spectroscopy. UV-Vis spectra of the samples were recorded by Cary 500i UV-Vis-NIR spectrophotometer. A depolarizer (*Harrick Scientific Corporation DPS-R4V*) was always attached before the detector to remove the effect of polarization on detected signal level. For polarization-dependent measurement, a polarizer (*Harrick Scientific Corporation PGT-S1V Glan-Taylor*) was attached after the light source to introduce linear polarization with a tunable polarization angle. Samples were mounted upon a holder with a 1 mm circular aperture. Nanorod arrays were aligned to the center of the aperture under an optical microscope. The range of scan was set to 400 nm – 1200 nm. UV-Vis spectroscopy (400 nm – 900 nm) used PMT detector and NIR spectroscopy (900nm – 1200 nm) used InGaAs detector. The scan rate was 200 nm/min, the data interval was 1 nm, and the average time for each data point was 0.3 s.

Figure 2.3 shows the Au nanorod surface plasmon resonance measured with UV-Vis spectroscopy. Figure 2.3a shows the extinction (the sum of light absorption and scattering) spectra of Au nanorod arrays with different nanorod lengths (50 nm, 60 nm, 70 nm, 80 nm), while the nanorod width is fixed at 20 nm. The baseline extinction was measured from ITO-coated sapphire substrates. The extinction peak is induced by the longitudinal surface plasmon mode of the nanorods, and the peak is redshifted with an increasing nanorod length. Figure 2.3b shows the normalized surface plasmon peak intensity for different polarization angles of the linearly polarized incident light. As expected for the nanorod longitudinal mode, the mode is excited when the light is polarized along the long axis of the nanorod. The optical characterization confirmed the surface plasmon excitation of the Au nanorods, and assisted the nanorod design to tune the surface plasmon resonance wavelength.

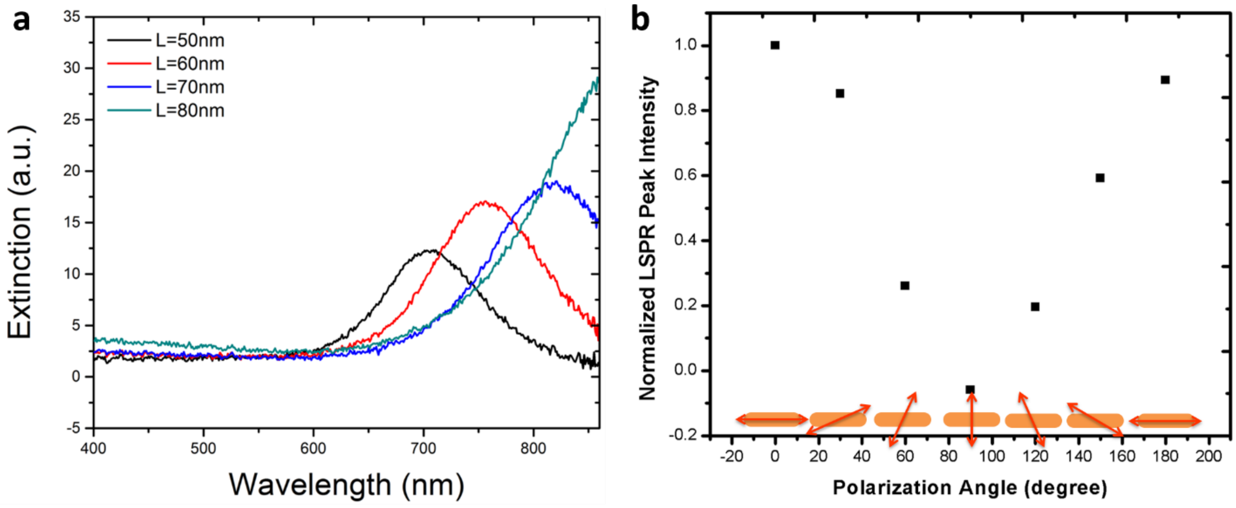

Figure 2.3. UV-Vis spectroscopy of Au nanorod arrays. (a) Extinction spectra of Au nanorod arrays with different nanorod lengths (50 nm, 60 nm, 70 nm, 80 nm). The nanorod width is 20 nm. (b) Normalized localized surface plasmon resonance (LSPR) peak intensity for the incident light with different polarization angles. The schematics show the orientations of the electric field of the linearly polarized light with respect to the nanorod.

Figure 2.4 shows the optical characterization and electromagnetic simulation of Au nanorods with and without a Ti adhesion layer. Both the measured extinction spectra (Figure 2.4a) and simulated field enhancement spectra (Figure 2.4b) show the Ti adhesion layer induces damping of the surface plasmon. The peak field enhancement for Au nanorod without an adhesion layer is approximately twice that of a Au nanorod on a Ti layer. Broadening of the surface plasmon peak in the presence of a Ti layer also indicates Ti-induced damping of the surface plasmon. Figure 2.4c&d show the optical near-field profiles around the nanorod without and with a Ti adhesion layer, illustrating the damping of the surface plasmon and the reduction in the field enhancement induced by the Ti layer. The measured extinction peak (Figure 2.4a) shows a two-fold reduction when a Ti layer is present. The simulated field enhancement (Figure 2.4b) shows a roughly two-fold reduction induced by the Ti layer, which seemingly indicates a four-fold reduction, rather than a two-fold reduction, in intensity extinction. This discrepancy is due to the fact that the field enhancement is evaluated at the nanorod apexes, while the contribution to optical extinction comes from the volume-integrated magnitude-square of the field inside the nanorod. The partial oxidation of the Ti layer in the fabricated samples may also reduce the plasmon damping effect.

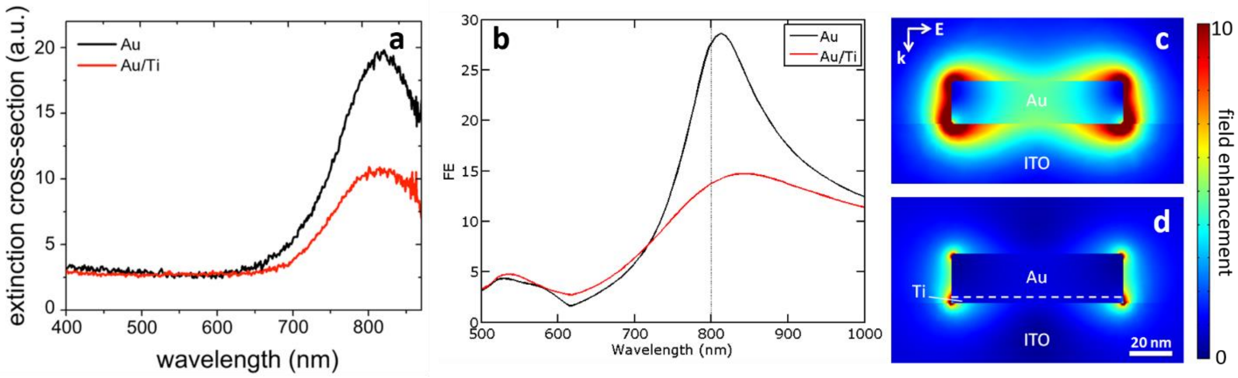

Figure 2.4. Optical characterization and electromagnetic simulation of Au nanorods with and without a Ti adhesion layer. (a) Measured extinction spectra for Au nanorod arrays with (red) and without (black) a Ti layer. (b) Simulated field enhancement spectra for Au nanorod arrays with (red) and without a Ti layer. (c,d) Simulated optical near-field profiles for Au nanorods without (c) and with (d) a Ti layer.

The effect of nanorod array pitch on the field enhancement has also been investigated. Figure 2.5 shows the measured extinction spectra and simulated field enhancement spectra for Au nanorod arrays with 200 nm × 100 nm pitch (200 nm along the nanorod and 100 nm perpendicular to the nanorod) and 200 nm × 200 nm pitch. Both measurement and simulation results indicate denser array leads to lower surface plasmon intensity, caused by near-field coupling. For the 200 nm × 100 nm pitch array, the surface plasmon spectral position is also slightly blue-shifted due to near-field coupling. Therefore, although in general a dense emitter array will produce more charge, this is no longer true when the array pitch becomes very small, as near-field coupling between nanorods suppresses field enhancement and dramatically reduces charge yield per nanorod.

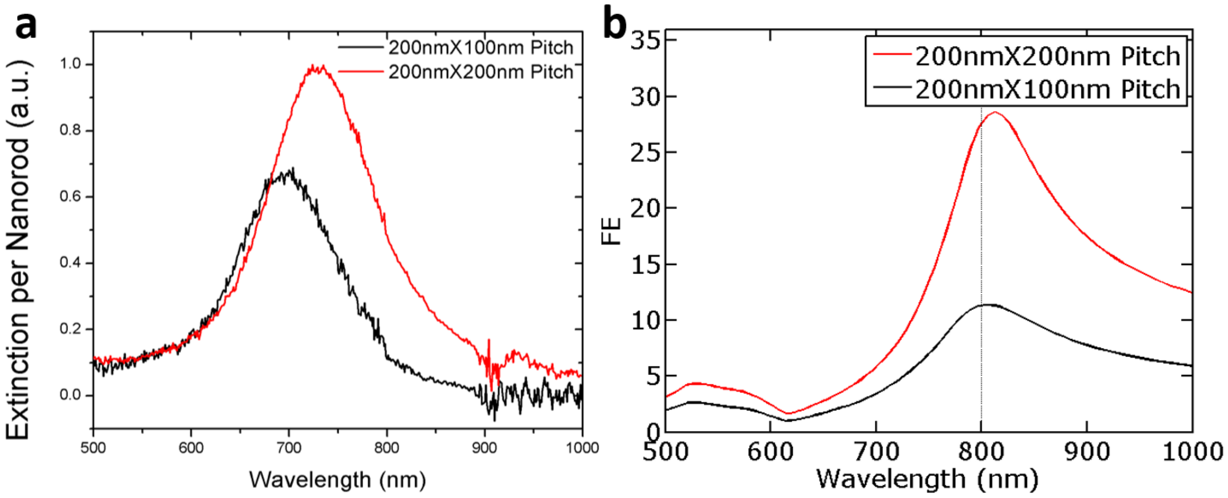

Figure 2.5. Surface plasmon of Au nanorod arrays with different pitches. (a) Measured extinction spectra, and (b) simulated field enhancement spectra of Au nanorod arrays with 200 nm × 100 nm pitch and 200 nm × 200 nm pitch.

2.5 Photoemission measurement

Photoelectron emission from Au nanorod arrays was triggered by 35 fs laser pulses from a Ti:sapphire laser with 800 nm central wavelength[1]. The light was normally incident on the nanorod array and linearly polarized along the nanorod long axis. The light was focused to a 90 μm full-width-at-half-maximum spot on the nanorod arrays. The nanorod samples were mounted in a high vacuum chamber (10^{-8} Torr), and the photoemission current was collected by an aluminum ring-anode placed on the sample chip with a 60-μm-thick mica insulating spacer.

The mechanisms of photoelectron emission can be characterized by the Keldysh parameter, $\gamma = \sqrt{\Phi/(2U_{pon})}$, where Φ is the work function for the material (or the ionization energy for photoelectron emission from atoms) , and $U_{pon} = e^2E^2/(4m_0\omega^2)$ is the ponderomotive energy,

---

[1] Photoemission measurement was performed by Dr. Richard Hobbs at Massachusetts Institute of Technology.

which is the cycle-averaged kinetic energy of an electron in an electromagnetic field with electric field amplitude E at frequency ω. For $\gamma \gg 1$, the photoemission is in the multiphoton regime, while for $\gamma \ll 1$, the photoemission is in the optical field regime. A full theoretical treatment of the multiphoton and optical field emission regimes, together with the transition between the two regimes, requires solving the time-dependent Schrodinger equation and evaluating the dipole transition rate from the initial free electron gas states in the metal to the final Volkov states in free space with an oscillating field [34,35]. With an increasing laser pulse energy, the time-averaged ponderomotive potential of the laser field increases, and it creates a higher potential step in excess of the work function of Au. Hence, more photons are required to be absorbed for electron emission to occur. This requirement leads to the closing of multiphoton emission channels with low photon numbers, while the sum of photoemission in the remaining multiphoton channels reproduces the Fowler-Nordheim tunneling formula that governs the optical field emission regime [35]. When plotting the photoemission current against the laser pulse energy, the transition from the multiphoton regime to the optical field regime leads to a soft kink in the scaling of photocurrent with pulse energy [36].

Figure 2.6 shows the photoemission current versus laser pulse energy for Au nanorod arrays with and without the Ti adhesion layer. At low pulse energy, the photocurrent scales with the 3rd power of pulse energy, suggesting the photoemission is in the multiphoton regime with a 3-photon process. We observed higher photocurrent from the nanorod array without the Ti layer, consistent with the optical characterization and electromagnetic simulation. At 12.1 nJ pulse energy (Keldysh parameter $\gamma \sim 4.5$ considering a plasmonic field enhancement of 20×), the photoemission current from the Au nanorod array is 26 times that of the Au/Ti nanorod array. Being a 3-photon process, the 26-fold increase in photoemission corresponds to a 1.7 times stronger field enhancement for the Au nanorods compared to Au/Ti nanorods, in agreement with the 1.9 times stronger field enhancement observed in simulation. At a high pulse energy such as 100 nJ, the calculated Keldysh parameter γ is about 1.5, indicating the emitters operate in the transition region between the multiphoton regime and the optical field regime. This transition partly contributes to the kink of the photocurrent scaling with pulse energy in Figure 2.6. Additionally, the space-charge effect also limits the photocurrent from the emitter arrays [11].

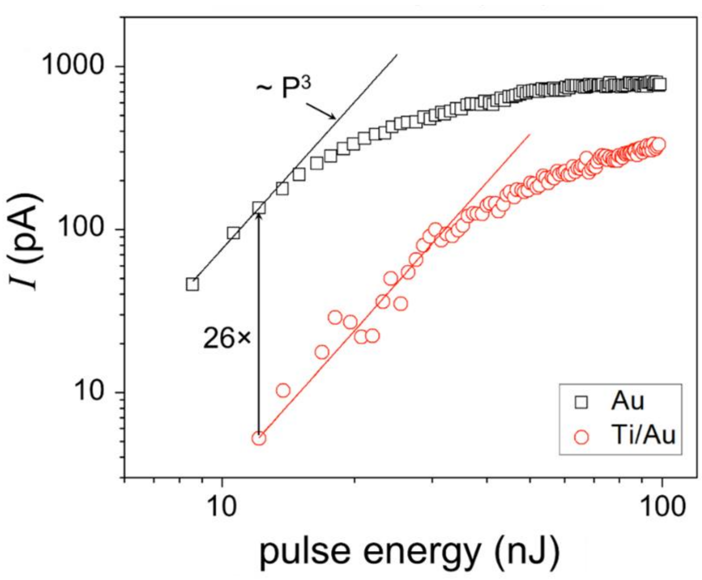

Figure 2.6. Photoelectron emission current for various optical pulse energies. Measurements from Au nanorod samples with and without a Ti layer are shown. At 12.1 nJ pulse energy, the photoemission current from the Au nanorod array is 26 times that of the Au/Ti nanorod array. The applied anode bias is 1 kV, and the nanorod array pitch is 400 nm.

In this work, the typically measured photocathode quantum efficiency (QE) is 1.2×10^{-5} for Au nanorod arrays illuminated with 800 nm wavelength light. This QE is comparable to the 4.7×10^{-5} QE for Au illuminated with 266 nm wavelength UV light [37]. Taking into account the light transmissivity of ~90%, the internal QE of the nanorod arrays is about 1.2×10^{-4}. When further considering a 10% power conversion efficiency from 800 nm wavelength light to 266 nm wavelength light by 3rd harmonic generation, and a factor of 3 difference in photon energy, the plasmonic Au nanorod arrays triggered by 800 nm wavelength light is ~100 times more efficient than UV-triggered Au photocathodes. This efficiency can be further improved by applying a strong static bias voltage to reduce the space-charge effect.

2.6 Summary

To summarize, we demonstrated Au nanorod arrays as optical field emitters. We used surface plasmon resonance to enhance the optical near-field and photoelectron emission yield. The quantum efficiency of our Au nanorod optical field emitters triggered by near-infrared optical pulses is higher than that of UV-triggered Au photocathodes. We also investigated the effect of the dielectric environment, including the substrate and the adhesion-promotion layer used in device fabrication, on the plasmonic resonance and photoelectron emission. Moreover, the Au nanorod optical field emitters can operate in the optical field photoemission regime, which may enable the production of ultra-short electron pulses, and optical-field-driven, ultrafast optoelectronic devices. The high-yield ultrafast optical field emitter arrays could find applications in the development of efficient and bright FEL, as well as time-resolved electron microscopy and spectroscopy experiments.

Chapter 3

Carrier-envelope phase detection with on-chip electrically connected nanoantenna arrays

Optical-field-driven, ultrafast light-matter interactions can be used in metrology and spectroscopy tools, as well as electronic and photonic devices for signal processing in the petahertz regime [38]. Specifically, the detection and control of carrier-envelope-phase (CEP) is important in attosecond science and optical frequency comb applications. Conventionally, CEP can be detected via interferometric techniques in the frequency domain, or above threshold ionization (ATI) in the time domain. The interferometric methods typically require a broadband optical spectrum spanning an octave in frequency, while the ATI methods usually require complicated and bulky vacuum apparatus. Recent reports have demonstrated time-domain CEP detection with optical-field-driven solid-state devices. However, the scaling and on-chip integration of these devices have yet to be shown. In this chapter, we develop CEP detectors using electrically connected bow-tie plasmonic nanoantenna with an array configuration on a chip. Optical-field-driven, CEP-sensitive photoelectron emission is enhanced by surface plasmon resonance. On-chip photoelectron emission and collection across a nanoscale gap leads to a high readout speed and permits high bandwidth operation. Symmetric, balanced detection with the nanoantennas removes the CEP-insensitive photoemission current, enabling high amplifier gains in photocurrent detection and reducing the noise caused by optical pulse energy fluctuation. The nano-gap emitter-collector configuration and distributed electrical connection to individual device relieve the need of a conductive film (e.g. indium tin oxide) and its associated fabrication complexity, and potentially enable multiplexed functions on a chip by using a different interconnect configuration. Our work takes a step towards compact on-chip integration of attosecond science experiments in ambient conditions, as well as future chip-scale integrated, optical-field-driven optoelectronic devices in the petahertz regime.

This chapter is organized as follows. In Section 3.1, we introduce the detection techniques of the carrier-envelope-phase (CEP), and briefly describe our solid-state CEP detectors based on electrically connected nanoantenna arrays. In Section 3.2, we describe the fabrication of the nanoantenna arrays, and demonstrate selective removal of short-circuit with an electromigration process. In Section 3.3, we discuss the design and electromagnetic simulation of the nanoantenna arrays. In Section 3.4, we present the detection of CEP with photoemission in the nanoantenna arrays, and show device degradation during the measurement. Finally, Section 3.5 summarizes our results.

3.1 Carrier-envelope phase detection with solid-state devices

The absolute phase of light is normally not important in continuous-wave optics, but it has vital importance in short optical pulses, for which the slowly varying envelope approximation breaks down. Carrier-envelop-phase (CEP) is the phase delay between the optical-frequency carrier wave and the intensity envelope of an ultrafast optical pulse. CEP is important in nonlinear optical processes. In the time domain, CEP determines the waveforms of ultrashort pulses together with the carrier wave frequency and pulse duration. CEP is crucial for attosecond physics including atom and molecule ionization [39,40], high-harmonic generation [41], and attosecond pulse generation [42,43]. In the frequency domain, periodic pulse train forms a frequency comb. The carrier-envelop-offset (CEO) frequency, the frequency at which the CEP is oscillating, corresponds to an offset of the frequency comb and is important in optical frequency comb applications such as optical frequency synthesis [44,45], high-resolution metrology [46], and quantum information science [47].

CEP detection can be achieved with interferometric techniques in the frequency domain [45,48]. For instance, an f-2f interferometer measures the CEO frequency from the beats between the second harmonic of a low frequency (f) part of the spectrum and a high frequency (2f) part of the spectrum. However, the interferometric techniques requires spectral broadening to achieve an optical octave with a spectrum spanning a factor of 2 in frequency, and nonlinear optical processes for second harmonic generation. Furthermore, the frequency-domain methods require multiple optical elements to perform interferometry. CEP has also been measured with time-domain interferometric methods [49]. However, only the relative change of CEP can be measured, and there is a lack of active feedback and control of the CEP. Additionally, CEP measurement can be performed via photoelectron emission [50–52]. However, complicated and bulky vacuum apparatus is usually needed.

Solid-state devices that can be used for time-domain CEP detection have been reported recently [53–55]. These devices enable time-domain CEP measurement in ambient conditions. Optical-field-induced current in a solid dielectric was used for CEP detection [53]. On-chip photoelectron-emission devices based on a single pair of bow-tie nanoantenna [54] and an array of plasmonic nanoparticles [55] also enable CEP detection. However, the scaling and large-scale on-chip integration of these solid-state devices have yet to be shown. In this chapter, we demonstrate CEP detection using electrically connected bow-tie plasmonic nanoantenna with an array configuration. Photoelectron emission is assisted by the strong optical-field enhancement induced by plasmonic resonance. On-chip electron emission and collection across a nanoscale gap leads to a high readout speed and permits high bandwidth operation. Symmetric, balanced detection with the bow-tie nanoantennas removes the CEP-insensitive photoemission current, enabling high amplifier gains in photocurrent detection and making the CEP detectors robust against optical pulse energy fluctuation [56]. The nano-gap emitter-collector configuration and distributed electrical connection to individual devices remove the need of a conductive film (e.g. indium tin oxide) and its associated fabrication complexity, and potentially enable multiplexed functions on a chip by using a different interconnect configuration. Our work takes a step towards compact on-chip integration of attosecond science experiments in ambient conditions, as well as future chip-scale integrated, optical-field-driven optoelectronic devices in the petahertz regime.

The nanoantenna device is schematically shown in Figure 3.1. An array of plasmonic bow-tie nanoantennas are supported by a transparent insulating substrate. Each bow-tie nanoantenna consists of a pair of nano-triangles. In the current configuration, all left nano-triangles of the bow-ties are electrically connected to a contact pad, while all right nano-triangles are electrically connected to another contact pad, and the device is a parallelized array of the photoelectron tunneling device previously reported [54]. The nanoantenna array is illuminated with an ultrafast optical pulse with a polarization along the bow-tie long-axis, which induces photoelectron emission from nano-triangles on one side to nano-triangles on the other side. For a bow-tie nanoantenna, the two nano-triangles are the cathode and anode for photoelectron emission and collection. Both the anode and the cathode are integrated on a single device chip, with a small separation on the order of 10 nm. The two contact pads are connected to an external circuit in which the photocurrent is measured. The CEP ϕ_{CE} of the pulse affects the photocurrent measured in the external circuit. For $\phi_{\mathrm{CE}} = 0$ (blue trace in Figure 3.1), the pulse has two symmetric optical half cycles, and the photocurrent in the two opposite directions cancel each other, leading to zero net photocurrent. For $\phi_{\mathrm{CE}} = \pi/2$ (red trace in Figure 3.1), the pulse has only one strong optical half cycle, and a net photocurrent can be measured. In the experiment discussed later in this chapter, ϕ_{CE} is modulated by a signal oscillating at a carrier-envelope-offset (CEO) frequency f_{CEO}. This CEO frequency can be measured from the photocurrent spectrum.

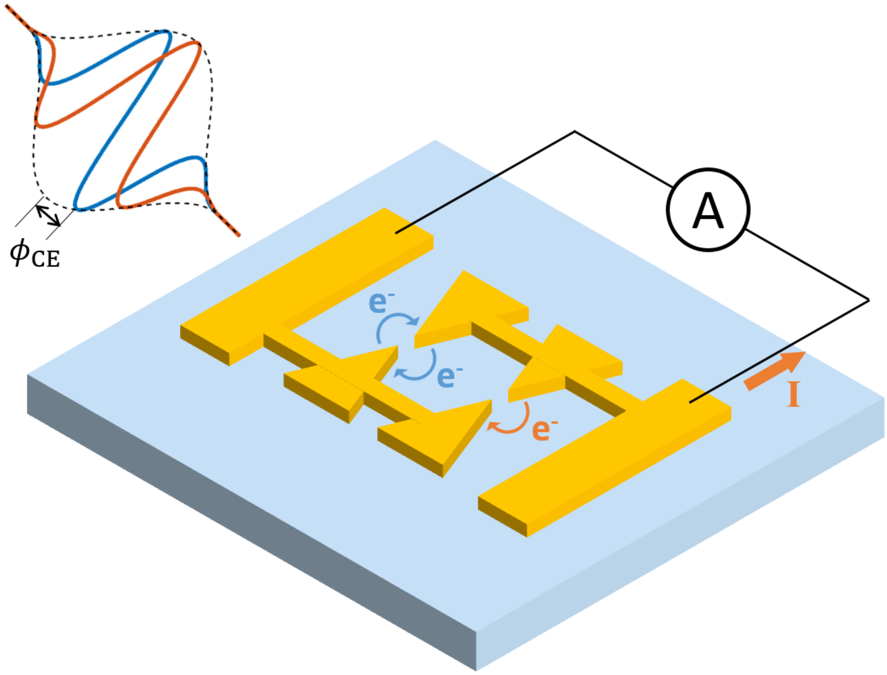

Figure 3.1. Schematic of the nanoantenna devices. An array of plasmonic bow-tie nanoantennas are fabricated on an insulating substrate. All left nano-triangles of the bow-ties are electrically connected to a contact pad, while all right nano-triangles are electrically connected to another contact pad. The nanoantenna array is illuminated with an ultrafast optical pulse, which induces photoelectron emission from nano-triangles on one side to nano-triangles on the other side. The CEP ϕ_{CE} of the pulse affects the photocurrent measured in the external circuit. For $\phi_{\mathrm{CE}} = 0$ (blue trace), the pulse is has two symmetric optical half cycles, and the photocurrent in the two opposite directions cancel each other, leading to zero net photocurrent. For $\phi_{\mathrm{CE}} = \pi/2$ (orange trace), the pulse has only one strong optical half cycle, and a net photocurrent can be measured. In the experiment discussed later in this chapter, ϕ_{CE} is modulated by an oscillating signal with frequency f_{CEO}. This CEO frequency can be measured from the photocurrent spectrum.

3.2 Sample fabrication

The plasmonic bow-tie nanoantenna arrays were fabricated on 10 mm × 10 mm glass (BK7) substrates with electron beam lithography (EBL) and a metal liftoff process. A ~70 nm film of PMMA was spin-coated onto the substrate and then soft-baked at 180 °C. A thin layer of Espacer was then spin-coated for charge dissipation during electron beam lithography. Bow-tie nanoantenna and electrical connection contact wire patterns were produced by an Elionix F-125 electron beam lithography system using an accelerating voltage of 125 kV and a beam current of 500 pA. The bow-tie nanostructures and electrical connection contact wires were defined and fabricated in one EBL step instead of two aligned EBL steps. Fabrication of the two structures together ensured good alignment accuracy between the bow-ties and the contact wires, which is critical for tuning the optical response of the nanoantenna arrays as shown later in this chapter. After exposure, Espacer was removed with 60 s DI water rinse. Exposed PMMA was developed in 3:1 IPA:MIBK at 0 °C for 30 s and then dried with flowing nitrogen gas. Metal layers of 2 nm Ti and 20 nm Au were then deposited via electron-beam evaporation. Metal lift-off was performed in NMP at 60 °C for approximately 60 min during which the sample was gently rinsed with flowing NMP. The lift-off was finished with 15 min sonication. No damage to the nanostructures was observed after sonication, in contrast to the nanorods arrays discussed in Chapter 1. The union of multiple connected bow-ties formed a larger structure compared to the isolated nanorods, making the bow-ties unaffected by sonication. After lift-off, the sample was rinsed with acetone and IPA. Finally, gentle oxygen plasma ashing (50 W, 60 s) was applied to remove residual resist and solvents.

The contact pads were fabricated via a subsequent photolithography step. Positive-tone photoresist S1813 was spin-coated and soft-baked at 110 °C for 4 min. Photolithography was performed with a Heidelberg µPG 101 direct laser writing system. After exposure, the samples were developed in Microposit MF-321 developer for 90 s and in DI water for 15 s. Metal layers of 20 nm Ti and 80 nm Au were then deposited via electron-beam evaporation. Lift-off was performed by soaking the samples in acetone for ~30 min followed by 3 min sonication.

Figure 3.2 shows the SEM images of the nanoantenna arrays. Figure 3.2a&b shows the nanoantennas fabricated on silicon substrates, which are conductive and free from charging issues, under the same conditions for nanoantenna fabrication with glass substrates. The nanoantenna array consists of 24×12 or 24×24 pairs of bow-ties. The array pitch was 800 nm in the x-direction (the direction of the bow-tie long axis), and 800 nm or 400 nm in the y-direction (the direction of the bow-tie short axis), with the full array covering an area of about 20×10 µm^2. The bow-tie gap size was tuned by changing the EBL dose, with the smallest average gap size below 20 nm. Figure 3.2c shows a nanoantenna array fabricated on a glass (BK7) substrate. The image artifacts (distortion, blurring, and varying contrast) are caused by charging during imaging.

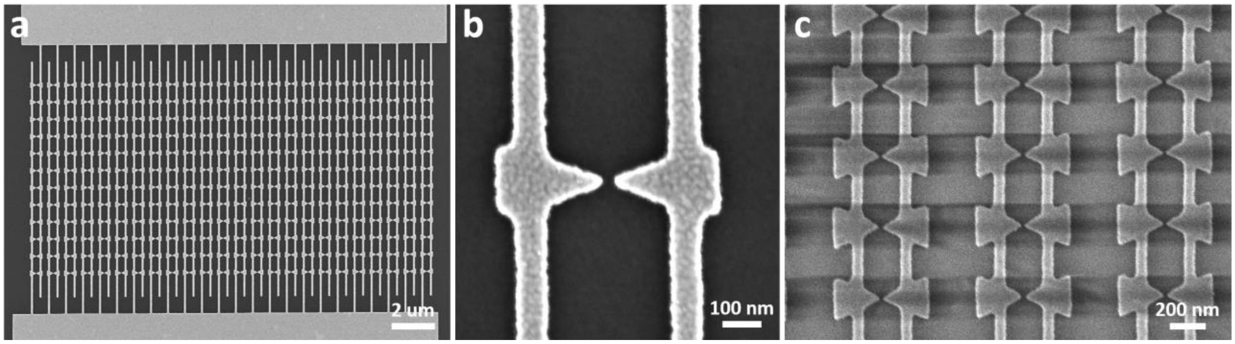

Figure 3.2. SEM images of the plasmonic nanoantenna arrays. (a) A plasmonic bow-tie nanoantenna array and two contact pads on silicon substrate. (b) A pair of plasmonic bow-tie nanoantenna with a 28 nm gap on silicon substrate. (c) A plasmonic bow-tie nanoantenna array on a glass (BK7) substrate. The image artifacts (distortion, blurring, and varying contrast) are caused by charging during imaging.

The fabricated bow-tie nanoantenna gap size varied from the nominal size due to process variations. If the two nano-triangles of a bow-tie were connected, they would electrically short the cathode and anode, making the whole array unresponsive for CEP detection. We used electromigration to remove these shorted devices by breaking their contact wires (Figure 3.3). In the electromigration process, a bias voltage was applied to the nanoantenna array connected in series with a 2.5 Ω resistor. The shorted devices had a low resistance and hence a high current, which broke the contact wires of these devices via electromigration. The normal devices had a large resistance and negligible current, and remained intact after electromigration. Figure 3.3a shows the voltage and current across a nanoantenna array during electromigration. The applied voltage (across the array and the resistor) was kept at 1 V for 50 s, and then increased to 1.25 V. Initially, the nanoantenna array was shorted, with a resistance of 15 Ω. Electromigration process started at 50 s, showing a decrease of the current, which indicates an increase resistance. At 250 s, the current dropped to zero, implying the array was transformed into an open circuit. At the start of electromigration, the average current in one contact wire is ~1 mA, with a current density of ~1 A/μm^2, consistent with previous reports [57,58]. Figure 3.3b shows the SEM image of a shorted nanoantenna array after electromigration. The contact wires were broken by electromigration. Figure 3.3c&d show two columns of bow-tie nanoantennas from an array. If all bow-ties along the column were disconnected (Figure 3.3c), the column was an open-circuit and the contact wires were not broken. However, if there were connected bow-ties along the column (Figure 3.3d), the column was shorted and the contact wires were broken by electromigration. Hence, the electromigration process is a surgical tool that selectively removes shorted devices from an array.

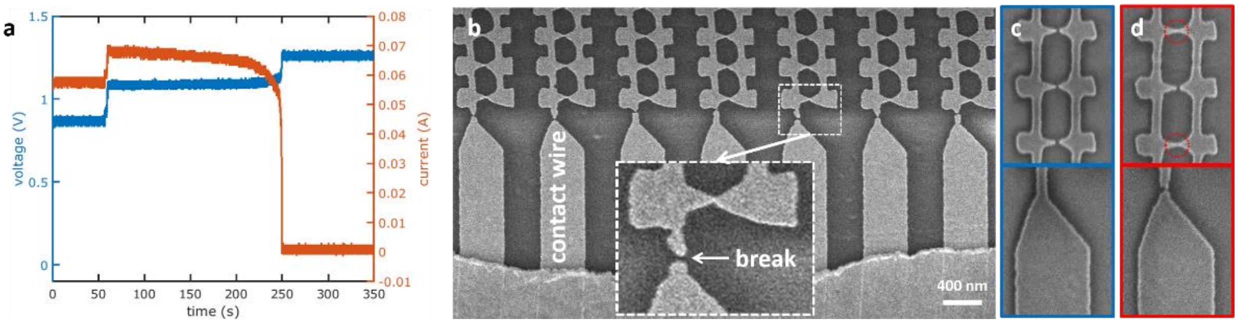

Figure 3.3. Electromigration of the plasmonic nanoantenna array. (a) Applied voltage and current across a plasmonic nanoantenna array during the electromigration process. Electromigration transformed a shorted array into an open-circuit array. (b) An SEM image of a connected plasmonic nanoantenna array after electromigration. The electrical contact wires were broken and disconnected during electromigration. Inset: zoomed-in image of the connected bow-tie antenna and the broken contact wire. (c) For an unbroken wire, the bow-tie nanoantennas along the wire are all disconnected. (d) For a broken wire, there is usually a short circuit caused by connected bow-tie nanoantennas (red dashed circles).

3.3 Electromagnetic simulation

We simulated the optical response of the plasmonic nanoantenna arrays with a finite element method electromagnetic solver (*COMSOL Multiphysics*). The modeled nanoantenna geometry was taken from SEM images of fabricated nanostructures. The 20-nm-thick Au nanoantenna was placed on the interface between vacuum and a glass (BK7) substrate, with a 2-nm-thick Ti adhesion layer in between. The optical properties of Au and Ti were taken from the work by Johnson and Christy [32] describing optical constants of the metals fabricated under similar conditions to ours (vacuum-evaporated polycrystalline thin films). The refractive index of glass was fixed at 1.5 as its dispersion was negligible in the wavelength range of interest. Periodic boundary conditions were applied to the simulation domain boundaries to model a periodic array of nanoantennas. The array pitch was 800 nm in the bow-tie long-axis direction and 400 nm in the bow-tie short-axis direction. The light was incident normally with a linear polarization along the bow-tie long-axis to excite the plasmonic mode. Perfect matched layers were added to the top and bottom of the simulation domain to absorb outgoing electromagnetic waves and model semi-infinite vacuum and substrate.

Figure 3.4 shows the simulated optical response of a nanoantenna array. Figure 3.4a&b show the extinction and field enhancement spectra. The extinction is defined as $-10\log_{10}(T/T_0)$, where T is the power transmissivity when the nanoantenna is present, and T_0 is the power transmissivity when the nanoantenna is absent (but the substrate is still present). Both power reflection and absorption were considered in the model. The field enhancement is defined as the ratio of the optical near-field at the bow-tie tip, averaged over the curved surface defined by the tip radius of curvature and gold thickness, to the optical field of the incident light. It can be seen that the extinction spectrum shows a double-peak feature with one peak at ~1100 nm wavelength and another peak at ~1300 nm wavelength, while the field enhancement spectrum shows a single peak at 1100 nm wavelength. The optical near-field around the nanoantenna is plotted at 1100 nm (Figure 3.4c) and 1300 nm (Figure 3.4d) wavelengths. For the peak around 1100 nm, the optical field is localized at the bow-tie tip, indicating this peak shows the plasmonic resonant mode of the bow-tie nanoantenna, and we named this mode as the “bow-tie mode”. For the peak around 1300 nm, an enhancement optical field is found around the bow-tie nanoantenna as well as the contact wires, indicating a plasmon mode propagating and resonating along the wires, and we named this mode as the “wire mode”. For photoelectron emission, the bow-tie mode is desired, as it produces a high field enhancement and a strong field localization at the tip. The field enhancement spectrum shows a broadband enhancement, which preserves the ultrafast characteristics of the optical pulse to induce CEP sensitive photoelectron emission.

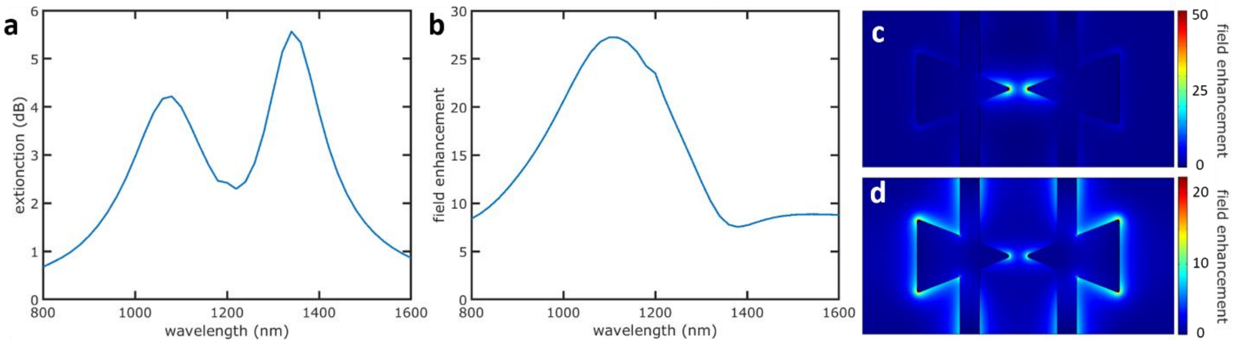

Figure 3.4. Electromagnetic simulation of electrically connected bow-tie nanoantenna arrays. Simulation of an array is achieved by using periodic boundary conditions. (a) Simulated extinction spectrum of the bow-tie array. (b) Simulated field enhancement (at the bow-tie tip) spectrum of the bow-tie array. (c,d) Simulated optical near field profile of the bow-tie nanoantenna at 1100 nm wavelength (c) and 1300 nm wavelength (d).

To further investigate the effect of the electrical connection contact wire on the nanoantenna optical response, we performed simulations with different contact wire positions (Figure 3.5). For comparison, we also include the spectra for the bow-tie nanoantenna without contact wires. Bow-tie without wires shows a single-peak extinction and field enhancement spectra. When the contact wires are added, the extinction peak is split into two peaks, corresponding to the aforementioned bow-tie and wire modes. It is observed that the spectral separation of the two peaks is small if the contact wire position is near the center of the nano-triangle (e.g. wire is 100 nm or 150 nm from the bow-tie center). The spectral separation of the two peaks increases, with the bow-tie mode being blueshifted and the wire mode being redshifted, when the contact wire position is close to the nano-triangle tip (e.g. wire is 50 nm from the bow-tie center) or nano-triangle base (e.g. wire is 200 nm from the bow-tie center). For the field enhancement spectra, the single peak is preserved if the wire position is near the nano-triangle center (e.g. wire is 100 nm from the bow-tie center), and double peaks show up when the wire moves towards the nano-triangle tip or base. These extinction and field enhancement spectra indicate that the bow-tie plasmonic mode is least disturbed when the contact wire is close to the nano-triangle center. For the bow-tie plasmonic mode, the nodes of the optical-near field distribution are close to the nano-triangle center. Placing the contact wires at these nodes leads to a minimal perturbation to the bow-tie plasmonic mode [59,60].

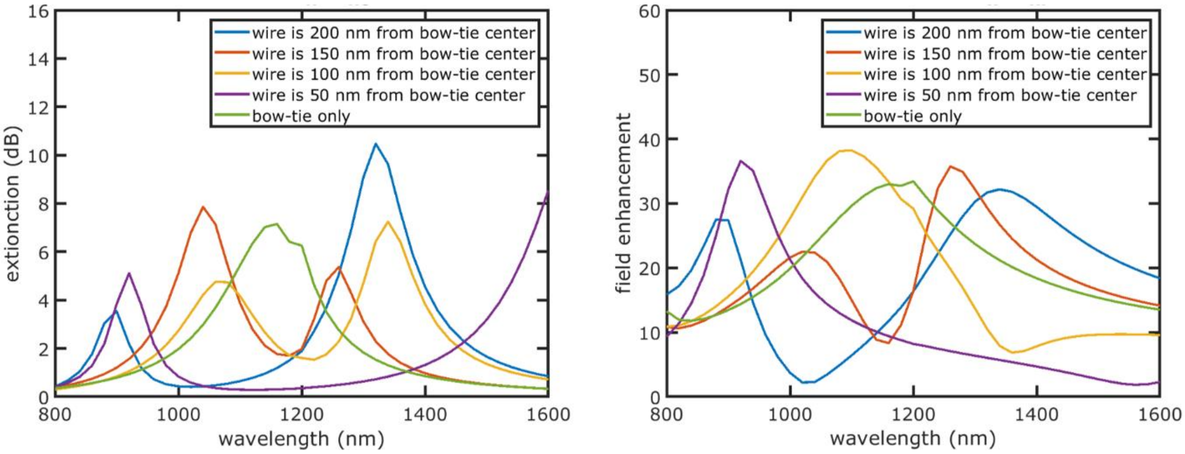

Figure 3.5. Simulated extinction and field enhancement spectra of the plasmonic bow-tie nanoantennas with different contact wire positions (the distance from the bow-tie center to the wire inner edge is 200 nm, 150 nm, 100 nm, and 50 nm, respectively). For comparison, we also include the spectra for the bow-tie nanoantenna without contact wires.

3.4 Optical characterization and photoemission measurement

Optical extinction and photoelectron emission of the plasmonic nanoantenna arrays were measured under the illumination of an optical pulse train[1]. The optical pulses had a center wavelength of 1177 nm, near the resonance wavelength of the plasmonic nanoantennas. The center wavelength and the plasmonic resonance wavelength do not need to be identical, as it was suggested that the overlapping of the plasmonic resonance with the pulse spectrum would lead to a broadened near-

---

[1] Optical and photoemission measurement was performed together with Dr. Phillip Keathley and Marco Turchetti at Massachusetts Institute of Technology.

field pulse after enhancement and a decreased CEP sensitivity [54,55]. The average pulse duration was ~10 fs (~2.5 optical cycles), the maximum pulse energy was ~190 pJ, and the repetition rate was 78 MHz. For photoemission measurement, the CEO frequency f_{CEO} of the pulse train was locked to 100 Hz. The photocurrent was first amplified by a transimpedance amplifier and then detected by a lock-in amplifier.

We measured the CEP sensitive photoelectron emission from the electrically connected plasmonic nanoantenna arrays. Figure 3.6a shows a typical photoemission current spectrum, with a CEP sensitive photocurrent of 4.7 pA and a signal-to-noise ratio of 16. From several tested devices, we measured up to 5 pA CEP sensitive current when illuminating ~12 bow-tie nanoantennas with a 2.25 μm × 4.1 μm beam spot size. The average photocurrent per nano-triangle emitter was about 0.2 pA. The averaged photocurrent was roughly the same as the reported result [54] using a single bow-tie nanoantenna and shorter optical pules, and was 4× the photocurrent in another report [55] using nanoparticle arrays under similar operation conditions to our devices.

We further confirmed the CEP sensitivity by inserting a barium fluoride (BaF_2) wedge in the optical beam path to shift the CEP (Figure 3.6b). Due to the mismatch between group velocity and phase velocity, the BaF_2 wedge can shift the CEP of an optical pulse traversing the wedge. The BaF_2 wedge was step-wise inserted by 10 mm every 20 s, and the expected CEP shift per step was 58°. We measured the phase between the photocurrent signal oscillating at f_{CEO} and the local oscillator signal used to lock f_{CEO}, and this phase shows a step-wise change of 55° per step.

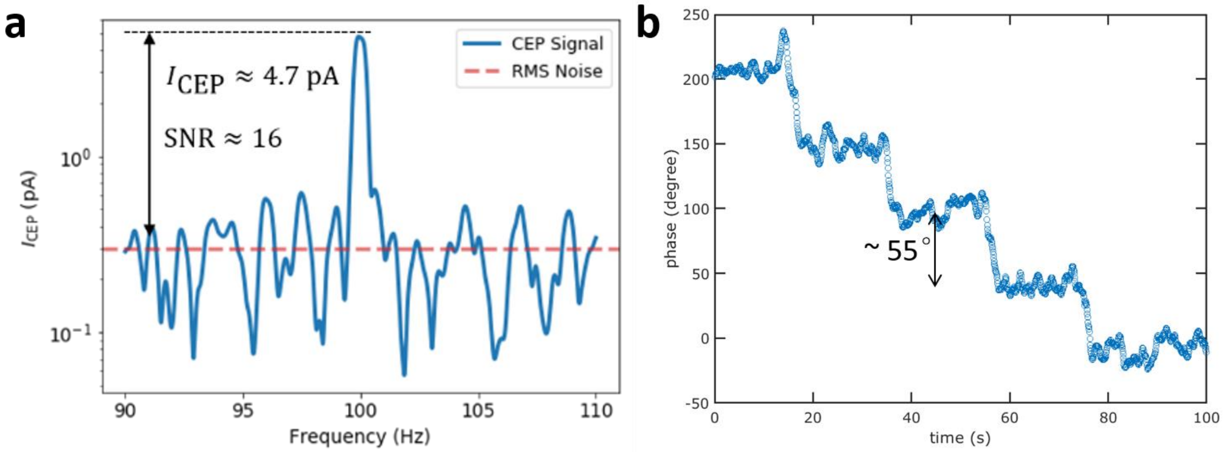

Figure 3.6. Measured photoemission from the nanoantenna array. (a) Spectrum of the photoemission current while the ϕ_{CE} is oscillating at 100 Hz. (b) Phase of the photoemission current when a BaF_2 wedge is step-wise inserted into the optical beam path every 20 s.

As our device is an electrically connected parallelized array, we also investigated the CEP sensitive photocurrent response from an entire array (Figure 3.7). The magnitude and phase of the photocurrent was measured by scanning the optical beam spot across a nanoantenna array. The photocurrent magnitude varies across the array, which is caused by the variation of the bow-tie nanoantenna geometry and hence the field enhancement responsible for photoemission. However, the photocurrent phase is relatively uniform across the array with 0.14π rad standard deviation, indicating the photoemission from the entire array is sensitive to the CEP and can be used for CEP detection. The uniform phase response indicates the CEP detection device is robust against optical pulse energy fluctuations and fabrication process variations.

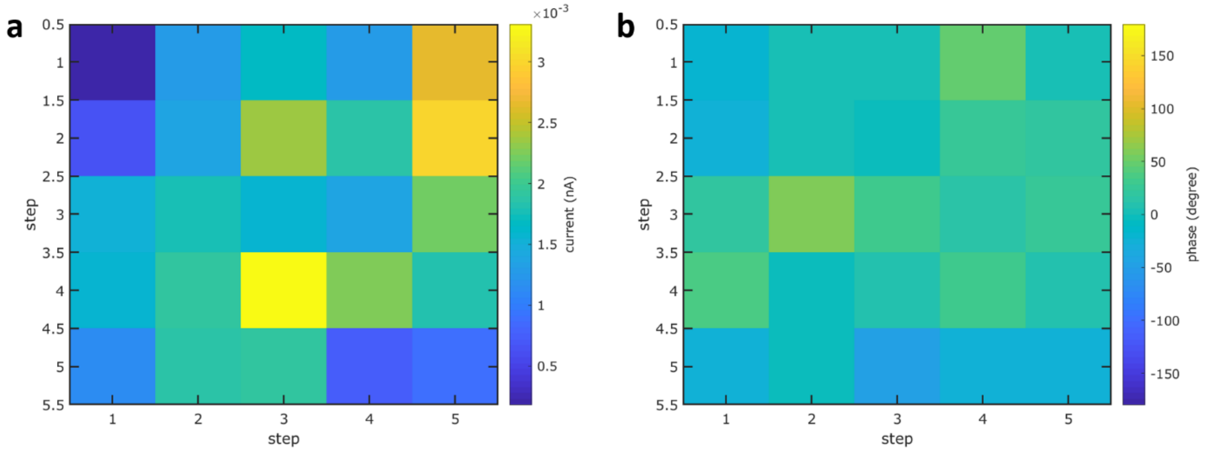

Figure 3.7. CEP-sensitive photoemission from an entire nanoantenna array. Magnitude (a) and phase (b) of the photoemission current are measured while scanning the optical beam across the array.

We observed a decrease of the CEP sensitive photocurrent in the first few seconds of exposing the nanoantenna arrays with the optical pulses. We ascribed this effect to laser-induced reshaping of the plasmonic nanoantennas. Figure 3.8 shows the SEM image of a nanoantenna array before (Figure 3.8a) and after (Figure 3.8b) photoemission measurement. The average gap size of the bow-tie nanoantennas increased from 39 nm to 62 nm. The increased bow-tie gap size led to a decreased field enhancement, and hence a decreased photoelectron emission current. This decrease saturated after a few seconds exposure time, as the increased gap size and decreased field enhancement eventually led to a condition below the threshold of laser-induced reshaping.

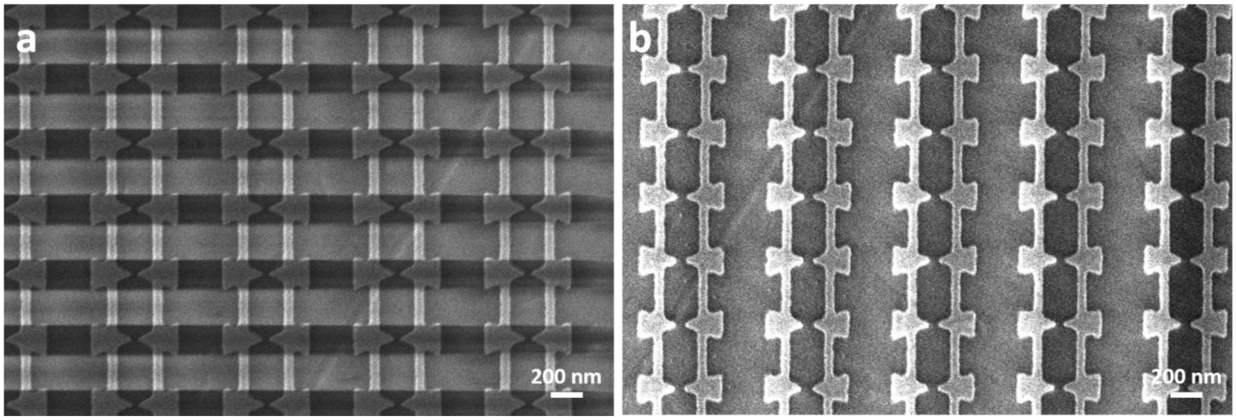

Figure 3.8. SEM images of a nanoantenna array before (a) and after (b) photoemission measurement. The contrast variation was caused by charging effect of the insulating substrate.

We performed optical extinction measurement on the nanoantenna arrays. Figure 3.9 shows the simulated and measured extinction spectra from an array before and after photoemission measurement. The simulation used geometries extracted from SEM images of the array. The double-peak feature of the spectra was obtained in both simulation and measurement, with the bow-tie mode around 1050 nm wavelength and the wire mode around 1250 nm wavelength. The wire mode was stronger in simulation than in measurement, since the simulation used periodic boundary conditions and assumed the wires were infinitely long, whereas the fabricated devices consisted of finite arrays and wires. The bow-tie mode was associated with individual nanoantennas and less affected by the finite array size, while the wire mode was associated with plasmons propagating and resonating along the wires and affected by the finite wire length.

Several other features of the extinction spectra were well reproduced in simulation and measurement. The exposure to optical pulses led to a larger spectral separation between the two peaks. The bow-tie mode was slightly blueshifted, with a decrease in its intensity, while the wire mode was slightly redshifted, with an increase in its intensity. The change of the extinction spectra before and after photoemission measurement is caused by a combined effect of laser-induced reshaping of the bow-ties and the change of the relative position between the wires and the nano-triangles (see earlier discussions) as a result of the reshaping.

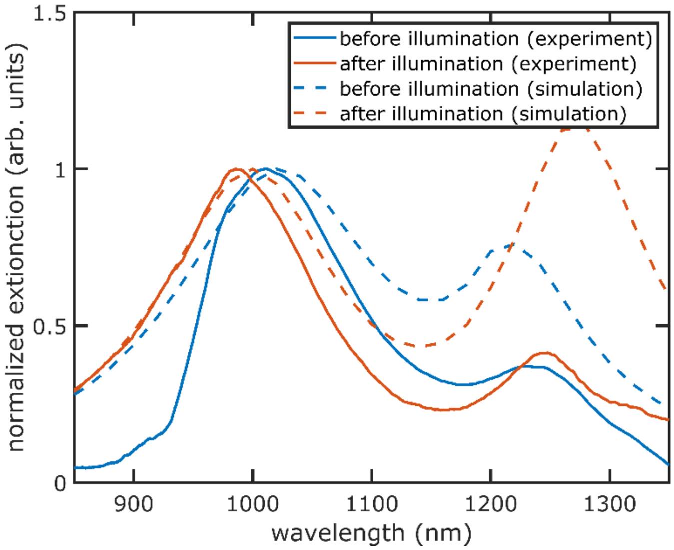

Figure 3.9. Simulated and measured extinction spectra of a nanoantenna array before and after laser illumination and photoemission measurement.

3.5 Summary

Based on the optical-field-driven photoemission, we demonstrate CEP detection using electrically connected plasmonic nanoantenna arrays. We fabricated electrically connected nanoantenna arrays with a nano-gap size down to sub-20 nm. Symmetric, balanced detection with the nanoantennas removed the CEP-insensitive photoemission current, enabling high amplifier gains in photocurrent detection and reducing the noise caused by optical pulse energy fluctuation. Distributed electrical connection to individual nanoantenna removed the need for a conductive layer and associated fabrication complexity, and could potentially permit multiplexed functions. Nanoscale separation between the emitter and collect, with an extracted RC constant of 0.3 fs for a nanoantenna, enabled high speed readout and high bandwidth operation. We used electromigration to selectively remove shorted devices caused by fabrication process variations. We performed electromagnetic simulations to design the nanoantenna with the desired plasmonic resonance mode to enhance the optical field and assist photoelectron emission. We also investigated the effect of the connection wire on the plasmonic mode. We detected CEP with the nanoantenna device, which produced a higher photocurrent and outperformed previously reported on-chip devices. Uniform phase response from the nanoantenna array was demonstrated. Furthermore, damage induced by exposure to ultrafast optical pulses was shown. In order to operate the CEP detectors at higher power without device degradation, alternative plasmonic materials, such as refractory plasmonic materials [61], are preferred. Our work demonstrates on-chip integration of multiple optical-field-driven optoelectronic devices with distributed electrical interconnection, and represents a step towards integrated ultrafast electronic and optoelectronic devices with petahertz operation frequencies.

Chapter 4

Electron-energy loss study of plasmonic modes in aluminum nanodisks

Surface plasmons are collective oscillations of electrons in a material coupled to electromagnetic fields, and are commonly used to confine light at the nanoscale and enhance light-matter interactions. Aluminum is a plasmonic metal capable of supporting high-energy surface plasmons in the ultraviolet (UV), thanks to its low optical loss and high bulk plasmon energy. Electron energy loss spectroscopy (EELS) has recently emerged as an alternative technique to optical characterizations for probing the surface plasmons of nanostructures with a high spatial resolution and the ability to excite dark plasmonic modes that do not couple efficiently to free space radiation. In this chapter, we investigate the electron energy loss spectroscopy of surface plasmon modes in aluminum nanodisks. We demonstrate the excitation of multipolar edge modes and breathing modes, depending on the electron beam positions. These modes are tunable in the UV region by varying the nanodisk size. We calculate the dispersion relations with both full wave electromagnetic simulations and simple intuitive models using the effective wavelength theory, and model the multipolar modes as ring-resonator modes at the periphery and the breathing modes as two-dimensional cavity modes. Furthermore, we theoretically investigate the surface plasmon modes for nanodisks of which the diameter is comparable to the thickness. We find some surface plasmon modes carry a polar nature and cannot be simply categorized as radial breathing modes or angular (azimuthal) multipolar edge modes. Part of the content in this chapter was derived from the work in [62].

This chapter is organized as follows. In Section 4.1, we introduce the EELS technique for the characterization of plasmonic nanostructures. In Section 4.2, we describe the fabrication of aluminum nanodisks on a thin supporting membrane for EELS measurement. In Section 4.3, we discuss the experimental EELS measurement of the nanodisks. In Section 4.4, we present the theoretical analysis of EELS and the plasmonic modes of aluminum nanodisks. Finally, Section 4.5 summarizes our results.

4.1 EELS for plasmonics

Surface plasmons are collective oscillations of electrons in a material coupled to electromagnetic fields, and are commonly used in light manipulation at deep-subwavelength scale [63]. The strong field enhancement and tight mode confinement of surface plasmon resonance enable its applications in spectroscopy [20,64,65], sensing [25,26,66–68], photodetection [69,70], photovoltaics [71,72], and metamaterials [22,23]. Conventional plasmonic materials are mostly noble metals such as gold and silver. Recently, aluminum has attracted a growing interest as a novel plasmonic metal [73–79]. Aluminum nanostructures support high energy surface plasmon resonances at visible to ultraviolet and deep-ultraviolet wavelengths, due to the low optical loss and high bulk plasmon energy (15 eV) of aluminum. Moreover, aluminum is cheap, naturally abundant, and CMOS-compatible. These properties make aluminum a promising candidate plasmonic material for large scale manufacturing and commercial applications.

Recently, electron energy loss spectroscopy (EELS) has emerged as an alternative technique to optical characterizations for probing the surface plasmon properties of nanostructures [80–93]. EELS is typically performed in a scanning transmission electron microscope (STEM), in which a focused electron beam induces surface plasmons in the nanostructure. The surface plasmon energy can be obtained by measuring the energy loss of the electrons, and the surface plasmon mode profile can be retrieved from the EELS map by scanning the electron beam around the nanostructure. Due to the tight focus of the electron beam, EELS has a high spatial resolution. Furthermore, EELS can probe the dark plasmonic modes which do not couple efficiently to free space radiation, in contrast to the far-field optical techniques that only access the bright modes.

Theoretical modeling is import to understand and analyze the experimental EELS data, as well as to assist the design of plasmonic nanostructures. Full wave electromagnetic calculations can accurately resolve the plasmonic properties of nanostructures, while simple intuitive models are also required to further the understanding of these properties and to better design the plasmonic nanostructures in various applications. Nanostructures prepared with lithographic techniques for EELS measurement typically possess a flat geometry with their lateral dimensions much larger than the thickness. In an intuitive picture, the surface plasmon modes of the flat nanostructure have been categorized into the multipolar edge modes, which are bound to the periphery of the nanostructure, and the breathing modes, which are confined within a two-dimensional cavity formed by the nanostructure [83]. The dispersion relation of the antisymmetric film plasmon mode can fit the dispersion of the breathing modes very well. However, the dispersion of the multipolar edge modes usually deviates from this dispersion relation. Sometimes additional nanostructures have to be experimentally fabricated and measured to reproduce the dispersion of the edge modes [91,92]. Moreover, advanced nanolithography produced nanostructures with a lateral dimension similar to the thickness, and for these nanostructures, it is not fully clear how these modes behave and couple to the excitation electron beam.

In this chapter, we investigate the electron energy loss spectroscopy of surface plasmon modes in aluminum nanodisks. We experimentally observed the expected multipolar edge modes and breathing modes, with their excitations depending on the electron beam position. The resonant energies of these modes were tunable in the UV spectral range by changing the nanodisk diameter. We theoretically reproduced the dispersion relation of the breathing modes and especially the multipolar edge modes, for which we calculated the effective wavelength from a two-dimensional mode solver. Furthermore, we theoretically investigated the surface plasmon modes for nanodisks of which the diameter is comparable to the thickness. In this situation, the assumption of flat nanostructures is no longer valid, and we found the surface plasmon modes cannot be simply categorized as radial breathing modes or angular (azimuthal) multipolar edge modes. Some modes carry a polar dependence, and specifically, the polar nature of the breathing modes creates a net dipole moment in the vertical direction, suggesting these modes are bright.

4.2 Sample fabrication

The aluminum nanodisks were fabricated on a thin silicon nitride membrane (Figure 4.1) with electron beam lithography and a lift-off process. We started from a silicon nitride membrane TEM grid (*SiMPore Inc.*) with a 5 nm nominal membrane thickness. A 60 s oxygen plasma ashing was used to clean the grid and promote resist adhesion. The grid was then stuck to a sacrificial silicon chip for spin-coating a PMMA thin film resist with approximately 70 nm thickness. Resist soft-baking was performed at 180 °C for 2 min. The nanodisk pattern was defined by electron beam lithography via an Elionix F-125 system using 125 keV electrons. After exposure, cold development was performed at 0 °C in 3:1 IPA:MIBK. Aluminum thin film with a 15 nm thickness was deposited via electron-beam evaporation. The evaporation was performed at room temperature with a chamber pressure below 2×10^{-6} Torr and a deposition rate of 5 Å/s. The lift-off was performed in ~60 °C NMP by soaking the sample for ~120 min without sonication.

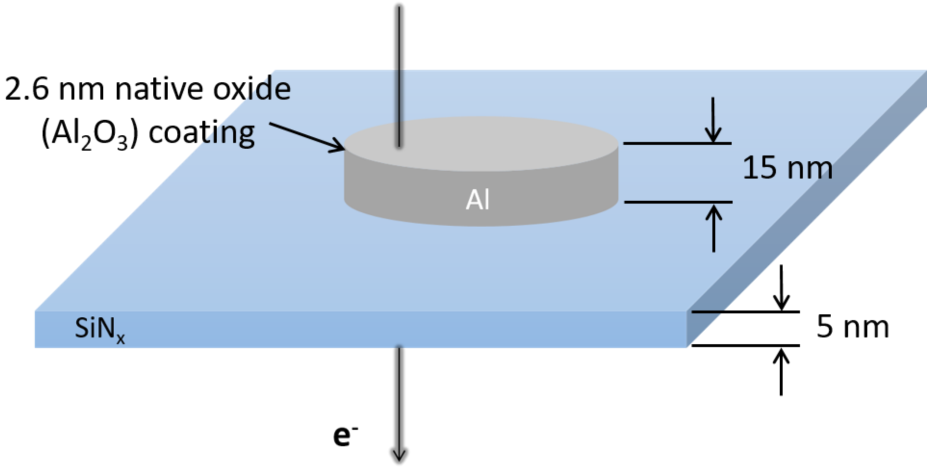

Figure 4.1. Schematic of the aluminum nanodisk structure. The nanodisk thickness is 15 nm, and is supported by a silicon nitride film with 5 nm thickness. The aluminum core is surrounded by a 2.6-nm-thick native oxide coating.

Aluminum nanodisks with diameters from 3 nm to more than 100 nm were fabricated. In ambient conditions, aluminum forms a native oxide (alumina) layer on its surface. The thickness of the native oxide is about 2.6 nm, measured from both the EELS mapping of aluminum nanodisks as well as the optical ellipsometry of aluminum films. Figure 4.2a shows a bright field TEM image of an aluminum nanodisk with a 6 nm diameter (including the native oxide on the surface). Figure 4.2b shows a high-angle-annular-dark-field (HAADF) image of an aluminum nanodisk with a 17 nm diameter.

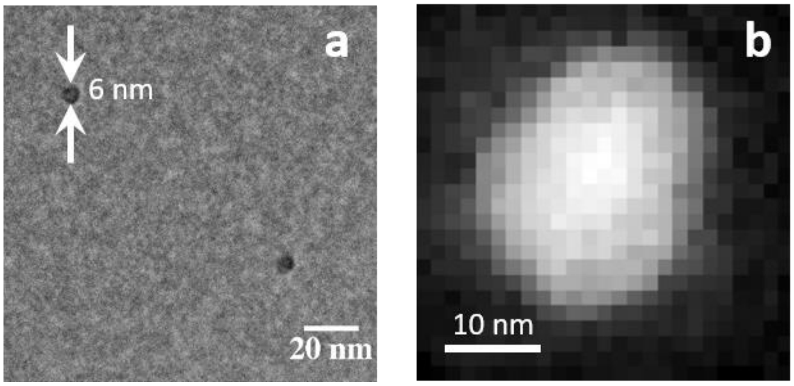

Figure 4.2. TEM images of aluminum nanodisks. (a) A bright field TEM image of an aluminum nanodisk with a 6 nm diameter. The image is acquired in a JEOL 2010 TEM operating at 200 kV acceleration voltage. (b) A high-angle-annular-dark-field (HAADF) image of an aluminum nanodisk with a 17 nm diameter. The image is acquired in a Hitachi 2700C STEM operating at 200 kV acceleration voltage.

4.3 Experimental EELS of aluminum nanodisks

The EELS measurement was performed in a Hitachi 2700C STEM[1]. The electron probe current is ~20 pA. The acceleration voltage was 200 kV and the electron beam energy spread was 0.4 eV. The EELS was acquired with a dispersion of 0.05 eV/channel and a step size of 1 nm. Figure 4.3a shows an example of the acquired EEL spectra. The zero loss peak represents the collected electrons with the initial beam energy (200 keV) and no energy loss. The peak at around 15 eV demonstrates the bulk plasmon of aluminum. A series of peaks show up in the 2-8 eV range, and they correspond to various surface plasmon modes of the aluminum nanodisks.

Figure 4.3b&c shows the resonant energies of plasmonic modes for nanodisks with various diameters, acquired by placing the electron beam at the nanodisk edge (Figure 4.3b) or the

---

[1] EELS measurement was performed together with Dr. Lihua Zhang at Brookhaven National Lab.

nanodisk center (Figure 4.3c). The theoretical EELS data is also illustrated, and we will discuss it later in details. To get the experimental surface plasmon energy, the background contributions from the zero loss peak and bulk plasmon peak were first subtracted, and then the spectra were fitted with several Gaussian peaks[1]. The plasmon energies were extracted as the center of the Gaussian peaks. Data points with different colors and symbols represent different plasmonic modes, with open squares showing the experimental data and solid symbols showing the simulation data. Mode assignment to the experimental data is performed by comparing to the nearest simulation data.

Several surface plasmon modes were observed in the aluminum nanodisks. To differentiate between electron-beam configurations, we named the modes as surface plasmon (SP) modes for electron-beam at the edge surface, and center plasmon (CP) modes for electron-beam at the nanodisk center. The SP modes were excited when the electron beam is at the nanodisk edge, while the CP modes were excited when the electron beam is at the nanodisk center, with the exception of SP1 modes which were excited in both configurations. The excitation of SP1 for electron beam at the center could be caused by symmetry-breaking due to the deviation of the fabricated nanodisks from a perfect cylinder, as well as the deviation of the electron beam from the center in EELS measurement. The SP1-3 modes are multipolar edge modes, including the dipole mode (SP1), quadrupole mode (SP2), and the hexapole mode (SP3). The CP1-2 modes are the first and second order breathing modes. The peaks around 7 eV (SP4, SP5, CP3) corresponds to the plasmon of an aluminum thin film [92]. We will discuss the surface plasmon mode profiles and dispersion relations with theoretical study later in this chapter. There is a slight blueshift (0.3 eV on average) of the experimental peaks from the simulated peaks, which could be due to variations of the

---

[1] Data fitting was performed by Sarah Goodman at Massachusetts Institute of Technology.

aluminum thickness and optical constants. By changing the aluminum nanodisk diameter, the plasmonic modes can be tuned from visible to vacuum ultraviolet spectral range.

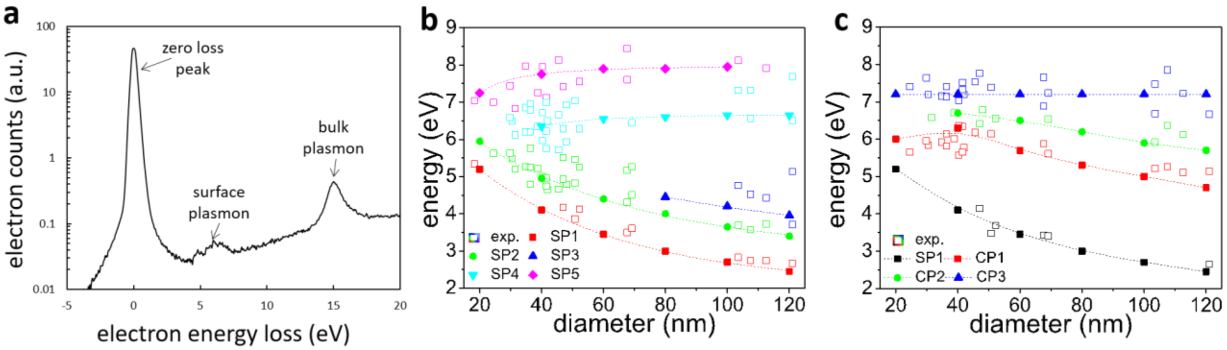

Figure 4.3. Surface plasmon for aluminum nanodisks probed with EELS. (a) A typical experimental EEL spectrum. The zero loss peak, the surface plasmon peaks, and the bulk plasmon peak are labeled. (b,c) Measured and simulated surface plasmon energies for aluminum nanodisks with different diameters (20 nm – 120 nm). The electron beam is placed at the nanodisk edge (b) or the nanodisk center (c). Data points with different colors and symbols represent different plasmonic modes, with open squares showing the experimental data and solid symbols showing the simulation data. Mode assignment to the experimental data is performed by comparing to the nearest simulation data.

4.4 Theoretical EELS of aluminum nanodisks

The structure under theoretical investigation was an isolated aluminum nanodisk supported by a silicon nitride thin film (Figure 4.1). This configuration was commonly used in EELS experiments studying surface plasmons of nanoparticles. The nanodisk thickness was 15 nm, and its diameter was varied to study the geometry-dependent plasmonic resonances. The sharp edges of the nanodisk were rounded with a 3 nm curvature to avoid singularities and to better represent experimentally fabricated nanostructures. We included a 2.6-nm-thick native oxide (alumina) coating surround the aluminum core [77]. The silicon nitride film thickness was 5 nm.

The electron beam was considered as a linear current induced by an electron moving in the vertical $\hat{\mathbf{z}}$ direction with a constant energy. This assumption is valid as the energy loss (~ eV) is much less than the electron energy (100 keV in our model). The theoretical treatment was previously reported [86,94] and we give a brief outline here. The spectral current density and electron energy loss probability can be expressed as

$$\boldsymbol{j}(z,\omega) = -\mathrm{e}\hat{\mathbf{z}}\delta[\boldsymbol{r}_t - \boldsymbol{R}_\mathbf{0}]e^{\mathrm{i}\omega z/v} \tag{4.1}$$

$$\Gamma_{\mathrm{EELS}}(\omega) = \frac{v\mathrm{e}}{2\pi\hbar\omega}\int dz\,\mathrm{Re}[e^{-\mathrm{i}\omega z/v}\hat{\mathbf{z}}\cdot\boldsymbol{E}_{\mathrm{in}}(z,\omega)] \tag{4.2}$$

Here, $\boldsymbol{j}(z,\omega)$ is the current density as a function of position and (angular) frequency, e is the electron charge, $\hbar$ is the reduced Planck constant, v is the scalar velocity of the electron, $\boldsymbol{r}_t = (x,y)$ is the transverse position, $\boldsymbol{R}_\mathbf{0} = (x_0,y_0)$ describes the transverse position of the electron beam, and $\boldsymbol{E}_{\mathrm{in}}(z,\omega)$ is the electric field induced by the linear current.

The induced field was calculated by a finite-element electromagnetic solver (*COMSOL Multiphysics*) using the linear current excitation. Excitation electron beam was modeled by a long cylinder carrying the linear current. The cylinder diameter was 1 nm, representing a finite beam spot size. For the numerical simulation results shown in this chapter, the electron beam current density was assumed to be constant in the transverse (x, y) plane of the cylinder. Instead of an infinitely narrow line, using a finite diameter cylinder avoids singularities in the calculation, improves the meshing quality, and allows for the implementation of arbitrary current distribution in the transverse plane. The optical properties for aluminum were taken from Rakić [95] with linear interpolation. The refractive index of alumina and silicon nitride were fixed at 1.88 and 2.4, respectively, as the dispersion of both materials were negligible within the spectral range of interest. Small variations in the dielectric refractive indices could lead to a small shift in the plasmonic mode energy, but would not affect the mode profile. The full calculation domain was encapsulated in a 50-nm-thick spherical perfect matched layer (PML) to absorb outgoing electromagnetic waves without undesired reflection at the domain boundary. Due to the many different length scales in the model (electron beam diameter of 1 nm, Al nanostructure on the order of 10 nm, calculation domain on the order of 100 nm), entities in the model were meshed adaptively with highly nonuniform tetrahedral discretization elements to ensure a high quality meshing. EELS was simulated in the energy range of 2 eV to 8 eV with a 0.05 eV energy step. Maxwell’s equations were solved in the frequency domain using the multifrontal massively parallel sparse (MUMPS) direct solver.

Figure 4.4 shows the simulated electron energy loss spectra and plasmonic mode profiles of an aluminum nanodisk with 120 nm diameter. Two configurations with different electron-beam positions were considered: one at the nanodisk edge and the other at the nanodisk center. Multiple EELS peaks corresponding to various plasmonic modes were observed in both configurations (Figure 4.4a). We labeled the three lowest modes (SP1 at 2.5 eV, SP2 at 3.4 eV, and SP3 at 4.0 eV) for electron-beam at the edge, and the two lowest modes (CP1 at 4.7 eV and CP2 at 5.7 eV) for electron-beam at the center. Figures 4.4b&c demonstrate the surface normal electric field profiles of the modes for the two electron-beam configurations. For the case with the electron-beam at the edge (Figure 4.4b), the mode profiles show the three modes are multipolar edge modes: dipole mode (SP1), quadrupole mode (SP2), and hexapole mode (SP3). For the case with the electron-beam at the center (Figure 4.4c), the mode profiles show the two modes are 1st (CP1) and 2nd (CP2) order breathing modes. The electron beam excitations of multipolar and breathing modes shown here are consistent with previous reports [82,83,96].

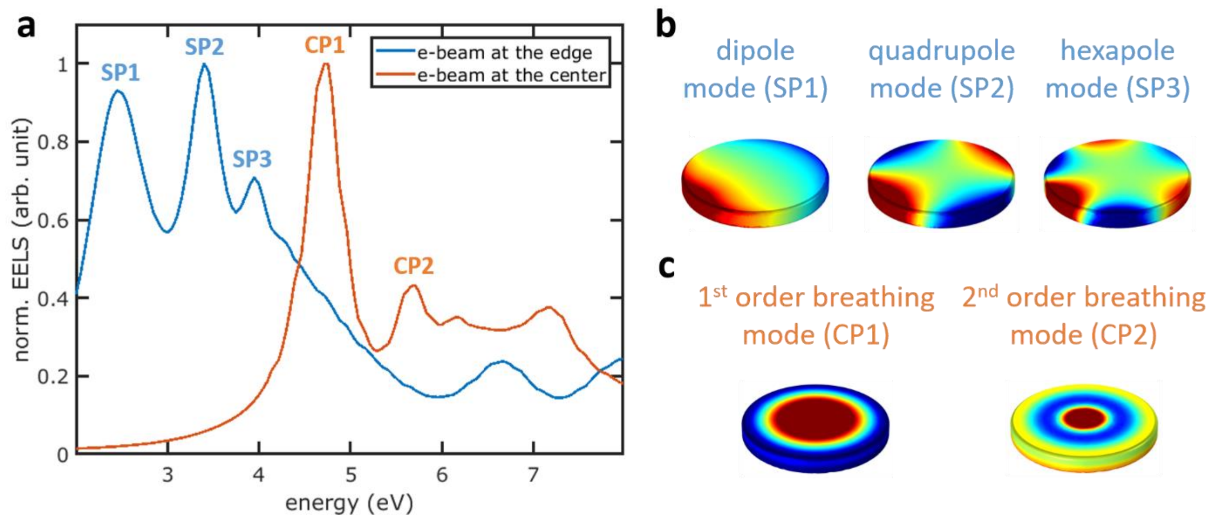

Figure 4.4. Simulated electron energy loss spectra and plasmonic mode profiles of the aluminum nanodisk. (a) Normalized electron energy loss spectra of an aluminum nanodisk with 120 nm diameter. The electron beam is either at the edge (blue) or at the center (orange) of the nanodisk. The labeled peaks correspond to three lowest modes (SP1, SP2, SP3) for electron-beam at the edge and two lowest modes (CP1, CP2) for electron-beam at the center. (b) Surface normal electric field profiles of the three lowest modes for electron-beam at the edge. According to the mode profiles, SP1 is the dipole mode, SP2 is the quadrupole mode, and SP3 is the hexapole mode. (c) Surface normal electric field profiles of the two lowest modes for electron-beam at the center. According to the mode profiles, CP1 is the 1st order breathing mode, and CP2 is the 2nd order breathing mode. In **b** and **c**, the color scale is saturated to better visualize the mode profiles.

We studied the plasmonic modes of aluminum nanodisks with diameters ranging from 120 nm down to 20 nm. Figure 4.3b&c shows the plasmonic mode resonant energies for these nanodisks. As expected, the multipolar and breathing modes were blue shifted with decreasing nanodisk diameter. For instance, the SP1 mode was shifted from 2.5 eV (corresponding to 496 nm free space wavelength) for a 120-nm-diameter nanodisk to 5.2 eV (corresponding to 238 nm free space wavelength) for a 20-nm-diameter nanodisk, and the CP2 mode was shifted from 5.7 eV (corresponding to 218 nm free space wavelength) for a 120-nm-diameter nanodisk to 6.7 eV (185 nm free space wavelength) for a 40-nm-diameter nanodisk. By changing the aluminum nanodisk diameter, the plasmonic modes can be tuned from visible to vacuum ultraviolet spectral range.

We note the plasmonic modes for a 20-nm-diameter nanodisk behave unexpectedly. For the case with the electron-beam at the nanodisk edge, the second plasmonic mode at 6 eV is in fact the 1st order breathing mode (CP1) rather than the quadrupole mode (SP2) by inspecting the mode profile. However, the energy of this mode does not follow the trend of other CP1 modes for the nanodisks with a diameter ranging from 120 nm to 40 nm, as it is red shifted compared to the CP1 mode of a 40-nm-diameter nanodisk. For nanodisks with small diameters, the assumption of "flat nanostructures" [83] is no longer valid, causing the unexpected mode energy. We will also discuss it later for a 12-nm-diameter nanodisk.

The dispersion relation of plasmonic modes can be obtained by scaling the modes to surface plasmon polariton (SPP) modes propagating at an extended thin film or at the edge of a thin film [82–84,90,92]. Specifically, the multipolar modes of plasmonic nanoparticles can be considered as surface plasmon edge modes propagating and resonating at the periphery of the nanoparticles, while the breathing modes can be considered as thin film SPP modes confined in a two-dimensional cavity defined by the nanoparticle geometry. We show the dispersion relation of aluminum nanodisk plasmonic modes in Figure 4.5. The breathing modes can be considered as the thin film SPP modes confined in the nanodisk cavity, with the surface plasmon wavenumber k satisfying the following relation

$$k_n D = 2n\pi - \phi \tag{4.3}$$

Here, n is the mode order, D is the nanodisk diameter, and ϕ is the nontrivial phase shift upon reflection at the nanodisk boundary [92,97,98]. Figure 4.5a shows the dispersion relation for the antisymmetric SPP modes of an extended thin film stack consisting of 15 nm aluminum and 5 nm silicon nitride, as well as the dispersion relation of the first and second breathing modes interpreted as nanodisk cavity modes. To fit the breathing modes and SPP mode dispersion relation, a phase shift $\phi = 0.6\pi$ was used.

The dispersion relation for the multipolar edge modes can be calculated considering the surface plasmon edge mode is circulating at the nanodisk periphery:

$$k_n \pi D = 2n\pi \tag{4.4}$$

Here, we dropped the phase shift term as we argue that no reflection boundary is encountered when the edge mode is circulating at the periphery. The dispersion relation of multipolar modes usually deviates slightly from the antisymmetric SPP mode [83,92]. This deviation is caused by the different effective wavelength (and hence wavenumber) of the surface plasmon edge mode compared with the antisymmetric SPP mode, as they are associated with different geometries. The SPP mode is associated with an extended thin film stack, while the edge mode is associated with the edge of a semi-infinite metallic film. To get a better fitting of the multipolar modes, we numerically calculated the exact dispersion relation of the surface plasmon edge mode via a two-dimensional (2D) mode solver in *COMSOL*. Figure 4.5b shows the dispersion relation for the surface plasmon edge mode, as well as the first, second, and third multipolar modes of the nanodisk. It can be seen that the dispersion relation of the surface plasmon edge mode serves as a better fit for the multipolar modes compared to the dispersion relation of antisymmetric SPP mode. Figure 4.5c&d shows the electric and magnetic field profiles of the fundamental surface plasmon edge mode supported by a semi-infinite aluminum thin film with 15 nm thickness on a 5-nm-thick silicon nitride film. The semi-infinite aluminum film on a silicon nitride film forms a plasmonic edge waveguide. The field penetration depth is on the order of 10 nm, which is comparable to the nanodisk diameter, suggesting the coupling of charges across the nanodisk causes the minor deviation of the multipolar modes dispersion relation from the edge mode dispersion relation. The accurate modeling of the multipolar edge modes as waveguide modes is consistent with previous reports [91,92].

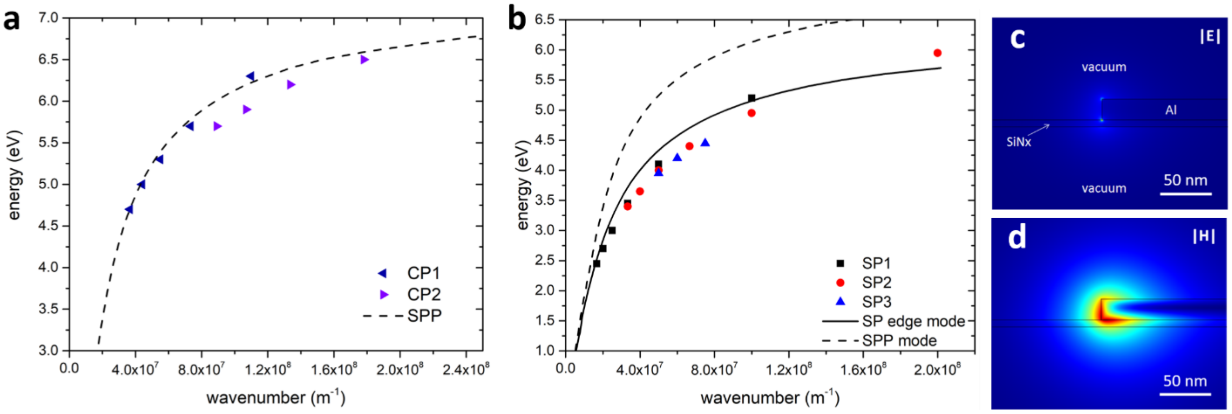

Figure 4.5. Simulated dispersion relation of plasmonic modes. (a) Dispersion relation of the breathing modes (CP1: navy blue left-pointing triangles, CP2: purple right-pointing triangles). The dashed black curve (SPP) shows the dispersion relation of the surface plasmon polariton (antisymmetric mode) of a thin film stack consisting of 15-nm-thick aluminum and 5-nm-thick silicon nitride. The fitting considers a 0.6π phase shift upon reflection at the nanodisk boundary. (b) Dispersion relation of the multipolar modes (SP1: black squares, SP2: red circles, SP3: blue triangles). The solid black curve shows the dispersion relation of the fundamental surface plasmon edge mode propagating along the edge of a semi-infinite 15-nm-thick aluminum film on a 5-nm-thick silicon nitride film. The dashed black curve shows the dispersion relation of the SPP mode as shown in (a). (c) & (d), electric and magnetic field profiles of the fundamental surface plasmon mode propagating along the edge.

We further investigated the surface plasmon modes of a nanodisk with a small diameter (Figure 4.6). The nanodisk diameter is 12 nm, comparable to its thickness (15 nm). Figure 4.6 shows the simulated electron energy loss spectra of the nanodisk with different electron-beam positions. Spectra with different colors correspond to different electron-beam positions illustrated in the inset showing the top-view of the nanodisk and the electron-beam positions. The coupling between the electron-beam and the surface plasmon modes depends on the beam position. Therefore, changing the beam position leads to various excitation intensities of the plasmon modes.

In Figure 5, we identified four modes of the nanodisk: first order breathing mode at 4.7 eV, dipole mode at 6 eV, second order breathing mode at 6.5 eV, and a higher order mode at 6.8 eV.

For the nanodisk with a diameter similar to its thickness, the assumption of flat nanostructures is no longer valid, and we found the surface plasmon modes cannot be simply categorized as radial breathing modes or angular (azimuthal) multipolar modes. A polar order is required to describe these modes. The first order breathing mode at 4.7 eV (mode I) can be viewed as a polar mode, with opposite charge polarity at the top and bottom of the nanodisk. This mode carries a net dipole moment in the vertical direction, suggesting it is no longer a dark mode and can be accessed via far field optical excitation. Due to the polar nature of this mode, it can always be excited by an electron beam in the vertical direction, regardless of the horizontal position of the electron beam. Similar to the nanodisks with a larger diameter, the dipole mode at 6 eV (mode II) can only be excited when the electron beam is away from the nanodisk center, as the mode has an antisymmetric charge distribution in the horizontal plane. Since the mode is bound to the nanodisk edge, the excitation of the dipole mode is strongest when the electron beam is close to the edge of the nanodisk. The polar dependence of the plasmon modes is further manifested by mode III at 6.5 eV and mode IV at 6.8 eV. The mode profile of mode III shows a radial dependence of breathing modes in the horizontal plane, together with a polar dependence in the vertical direction. This mode is accessible only when the electron beam is close to the nanodisk center. The mode profile of mode IV shows an angular dependence similar to the dipole mode in the horizontal plane, but also a polar dependence in the vertical direction. This mode is accessible when the electron beam is away from the nanodisk center.

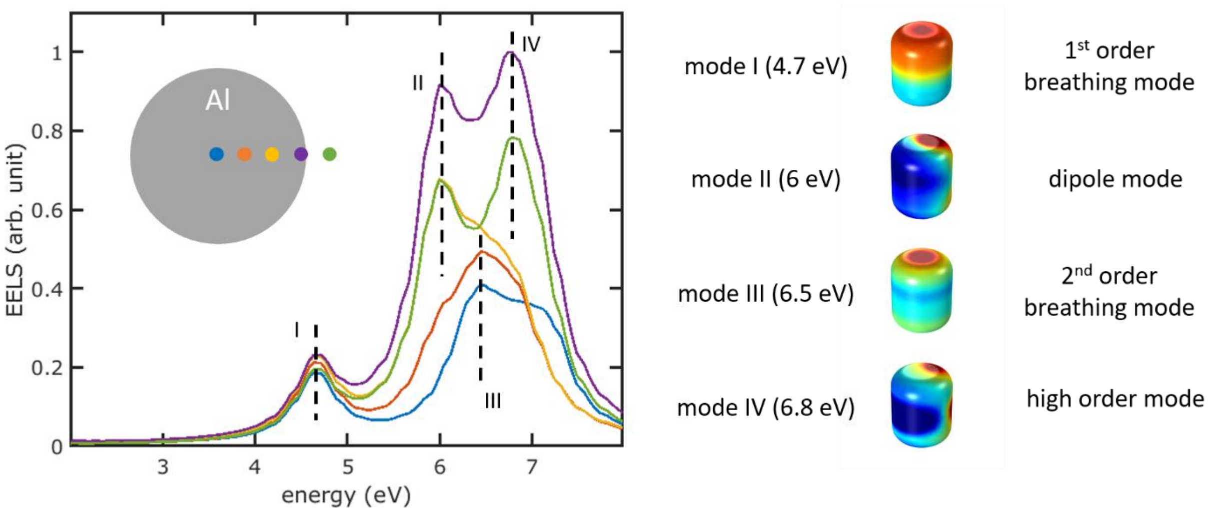

Figure 4.6. Simulated electron energy loss spectra and plasmonic mode profiles for an aluminum nanodisk with 12 nm diameter. Spectra with different colors correspond to different electron-beam positions, as illustrated by the inset showing the top-view of the nanodisk and the electron-beam positions. The black dashed lines indicate the mode energies for four plasmonic modes: 1st order breathing mode (mode I), dipole mode (mode II), 2nd order breathing mode (mode III), and a higher order mode (mode IV).

4.5 Summary

In summary, we have studied the electron energy loss caused by the excitation of surface plasmon modes of aluminum nanodisks. Surface plasmon energies for nanodisks with diameters ranging from 20 nm to 120 nm are measured with EELS and compared to numerical simulations. The plasmon modes can be characterized as the multipolar modes and the breathing modes. The breathing modes are modeled as cavity modes formed by confinement of the thin film antisymmetric surface plasmon polariton modes in the nanodisk, with a 0.6π phase shift upon reflection at the nanodisk boundary. The multipolar modes are modeled as ring-resonating modes bound to the nanodisk edge, with the dispersion relation accurately reproduced from a computationally less demanding 2D mode solver. For nanodisks with a diameter comparable to the thickness, the assumption of flat nanostructures is no longer valid. Besides the radial and angular dependence of the breathing and multipolar modes, the plasmon modes of a small nanodisk possess a polar nature. Our work demonstrate the plasmonic modes of aluminum nanodisks can be tuned from visible to vacuum ultraviolet spectral range, potentially benefiting UV applications. We showed both full wave electromagnetic simulations as well as simple intuitive models for theoretical investigation of the electron energy loss spectroscopy of the nanodisks. Being able to accurately reproduce the dispersion relation of plasmon modes calculated with three-dimensional full wave electromagnetic simulation, the intuitive model based on the 2D mode solver provides an alternative, less computationally intensive method to resolve the plasmon modes of nanostructures. This method could be especially useful for nanostructures of which simple analytical approach is not available due to the presence of substrates or complex geometries. Furthermore, for the breathing modes that are "dark" considering only the horizontal symmetries, the polar nature makes these modes bright, potentially accessible via far-field optical excitation and detection, which previously was only possible for large disks [96]. The theoretical treatment presented in this chapter is based on classical electromagnetics while neglecting the change of the state of the probing electron. To further investigate few-nanometer-sized metallic nanostructures and dielectric layers, classical electromagnetic treatment has to be augmented with quantum confinement [99], nonlocal effect [100–103], and electron tunneling [104–106]. For more accurate analysis, the change of the state of the probing electron also needs to be considered. Experimental study of small-diameter nanodisks, however, are prohibited by the weak surface plasmon EELS signals and a large fitting error, potentially due to a reduced structure thickness and a stronger oxidation effect caused by a large surface-to-volume ratio. To overcome these difficulties, alternative plasmonic materials and monochromated EELS measurement are preferred.

Chapter 5

Polarization-tunable light emission from free-electron-driven metasurfaces

Swift electrons in free space carry evanescent near field in a broad spectral range. When interacting with a certain electromagnetic environment, this near field can be converted to far field radiation, which is often utilized to construct free-electron light sources. As an example, free-electron lasers (FELs) use the interaction between free electrons and magnetic undulators to generate intense coherent radiation with a tunable frequency ranging from microwaves to X-rays, and are commonly used in materials science, chemical technology, biomedical research, and solid-state physics. However, FELs require large facilities and their availability is limited at few accelerator facilities around the world. For applications that do not require the high intensity and coherence provided by FELs, a lab-scale or table-top free-electron light source is more desirable. Recently, there has been a growing interest in generating optical-frequency electromagnetic radiation from free electrons with modest to low energies interacting with nanoscale structures, facilitating the development of compact and tunable light and surface plasmon sources driven by electricity. However, the polarization of free-electron-induced radiation strongly depends on the electron beam direction and is usually hard to control. In this chapter, we demonstrate polarization-tunable light emission from free-electron-driven metasurfaces. The metasurfaces consist of unit cells of C-shaped aperture nanoantennas. By changing the orientation of the nanoantennas, the polarization of the free-electron light emission can be controlled. Our work takes a step towards compact and tunable free-electron-driven light sources with potential applications in nanophotonics research, on-chip integrated light sources, charged particle detectors and beam diagnostics, biomedical imaging and diagnostics.

This chapter is organized as follows. In Section 5.1, we introduce the metasurface technique for tuning the polarization of free-electron light emission. In Section 5.2, we describe the fabrication of metasurfaces. In Section 5.3, we experimentally demonstrate polarization-tunable light emission from the metasurfaces driven by free electrons. Finally, Section 5.4 summarizes our results.

5.1 Metasurface free-electron light sources with a tunable polarization

Free electrons carry evanescent near field that induces electromagnetic excitations when interacting with a certain dielectric environment, such as interfaces, slow-light media, nanoscale resonators, and periodic structures [86]. Such effects are often utilized to construct free-electron radiation sources. These sources have great tunability, as one can tune the radiation wavelength by changing the electron energy or the dielectric environment. Early experiments on free-electron radiation sources focused on generating electromagnetic waves in the microwave and THz regimes [107–114], as well as the optical frequency using high-energy electrons [115–118]. In particular, free electrons moving in close proximity to a periodic structure generate far field electromagnetic radiation, referred to as Smith-Purcell radiation [115]. In the Smith-Purcell effect, spontaneous emission is observed when free electrons propagate parallel to the surface at close proximity, inducing a periodic motion of charge or dipole oscillation that emit coherently. Taking such configurations allows one to minimize heating effects and opens the possibility of recycling the free electron energy with a depressed collector [119]. Furthermore, free electron bunching effects can lead to highly efficient superradiant Smith-Purcell emission [120], a well-known mechanism accounting for gain in free-electron lasers [121]. Recently, there has been a growing interest in generating optical-frequency electromagnetic radiation from free electrons with modest to low energies interacting with nanoscale structures [86,122–131]. Light emission from nanostructures driven by free electrons facilitates the development of compact and tunable light and surface plasmon sources driven by electricity. These light sources could find applications in nanophotonics research [80], on-chip integrated light sources [124], charged particle detectors and beam diagnostics [132], and biomedical imaging and diagnostics [133].

Polarization is a fundamental property and degree of freedom of electromagnetic waves, and hence it is desirable to have the ability to control the polarization of light emission. However, the polarization of free-electron-induced radiation strongly depends on the electron beam direction and is usually hard to control. In Smith-Purcell-like processes the polarization is always parallel to the electron velocity. This limitation restricts the potential of such sources. This chapter attempts to bypass this limitation.

The electron beam excitation can typically be estimated by one or several electric dipoles oscillating in the electron beam direction, hence leading to predefined radiation patterns and polarization properties. There have been some reports on manipulating the polarization of free-electron light emission based on artificial structures [127,134–137]. However, very few experiments have paid attention to the polarization control of Smith-Purcell radiation, mainly due to the difficulties in manipulating the polarization given the fixed geometrical configuration in the experiments, as illustrated in Figure 5.1a. Smith-Purcell radiation is generated when free electrons interact with a periodic structure, such as a grating, along their moving direction, so that the grating lines are perpendicular to the beam direction (in oblique incidence, there is an “effective grating” with its lines perpendicular to the beam direction). The spatially modulating image charges inside the grating – induced by the free electrons – give a preferential polarization to the generated radiation. As a result, the induced far-field radiation has a transverse magnetic (TM) polarization, with its electric field perpendicular to the grating lines and magnetic field parallel to the grating lines.

Metasurfaces are artificial media consisting of subwavelength structures patterned on a surface [138–140]. Metasurfaces usually possess electromagnetic properties unattainable in natural materials and thin films, and have been used to control electromagnetic wave properties including amplitude, phase, wave vector, polarization, spectral shape, spatial distribution, and orbital angular momentum [141]. There have been several reports on free-electron light emission from complex artificial structures [124,125,127,130,131,142–145]. Specifically, in the context of Smith-Purcell radiation, the requirement of periodic structures is conveniently met by the periodic nature of metasurfaces. By changing the line structure unit cell of gratings used in conventional Smith-Purcell radiation to a complex unit cell structure, the radiation properties can be tailored according to the metasurface designs. However, no previous experiment has shown a control of the polarization of the Smith-Purcell radiation, which is widely considered as inherently fixed (parallel to the electron velocity). A recent theory proposal [146] suggested how this can be done with a novel metasurface design.

In this chapter, we demonstrate a tunable polarization metasurface free-electron light source based on Smith-Purcell radiation. The light source has not only a tunable wavelength achieved by varying the electron energy and the grating pitch, but also a tunable polarization direction that has never been demonstrated in Smith-Purcell radiation experiments.

The polarization of free electron light emission can be tuned by designed metasurfaces. Polarization control of Smith-Purcell radiation with Babinet metasurfaces has been theoretically proposed in the THz regime [146]. This concept is illustrated in Figure 5.1. Figure 5.1b shows the interaction between free electrons and a periodic metasurface, of which each unit cell is a C-shaped aperture (abbreviated as C-aperture in the following) in a metallic film. The C-aperture structure possesses an effective out-of-plane electric dipole in the x-direction, and an effective magnetic dipole across the C-opening in the y-direction. The electric and magnetic dipole resonances can be understood intuitively by applying the Babinet principle to its complementary structure, a C-ring structure, which possesses an electric dipole across the gap of the C-ring and an out-of-plane magnetic dipole. When the metasurface is driven by an electron beam, the x-component of the electron near field directly induces the out-of-plane electric dipole. The in-plane magnetic dipole is excited via antenna resonance that couples the electric and magnetic dipoles. As a result, the subsequent radiation from the dipole resonances has a transverse magnetic (TM) polarization, with the magnetic field in the y-direction (parallel to the metasurface and perpendicular to the electron beam direction) and the electric field in the x-z plane. This polarization of emitted light is the same as that of conventional Smith-Purcell radiation shown in Figure 5.1a. However, the situation can be changed via the metasurface design, as demonstrated in Figure 5.1c, by rotating the C-aperture structure. If the C-opening is facing the y-direction, the out-of-plane electric dipole remains in the x-direction, whereas the in-plane magnetic dipole is rotated to the z-direction. The emitted light then has a transverse electric (TE) polarization, with the electric field in the y-direction (parallel to the metasurface and perpendicular to the electron beam direction) and the magnetic field in the x-z plane. The polarization control mediated by metasurface design is able to produce radiation with its electric field polarized perpendicular to the electron beam, which is previously unattainable in regular Smith-Purcell radiation. Here we experimentally demonstrated tunable polarization light emission from free-electron-driven metasurfaces, and extended the operating frequency to the optical regime. We effectively developed a tunable nanoscale free-electron light source integrated with an adjustable polarizer.

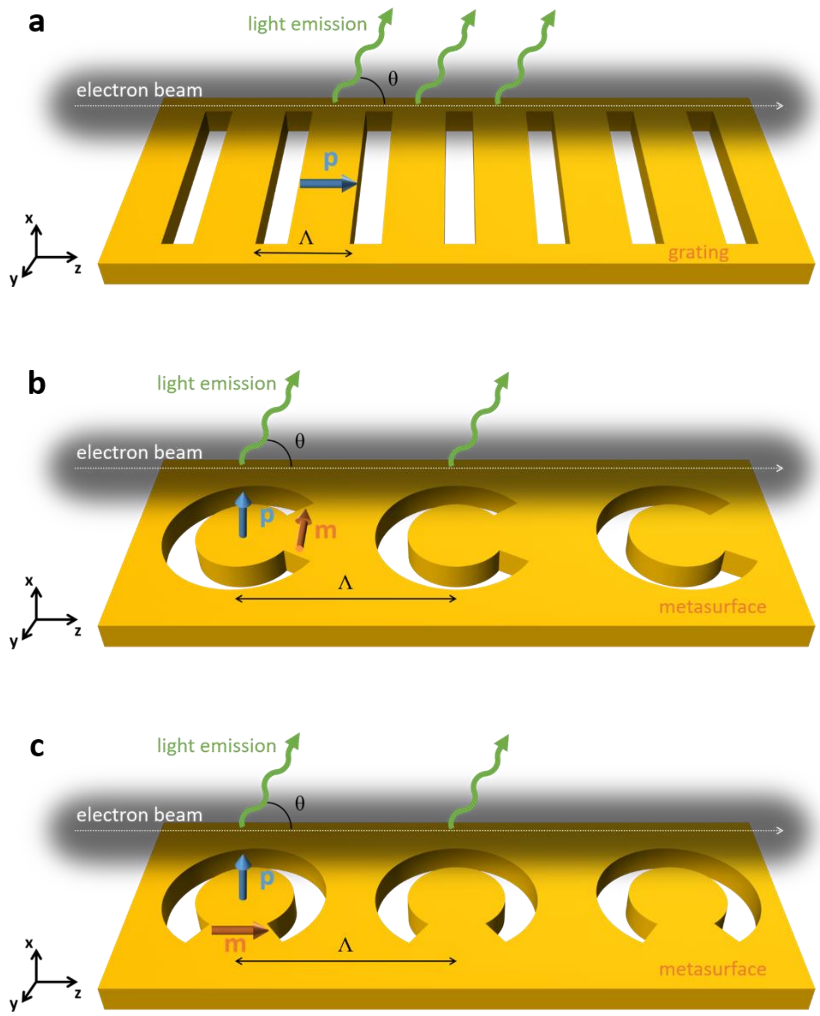

Figure 5.1. Free electron light sources based on periodically structured surfaces. (a) Schematic of light emission from the interaction of free electrons and a grating. When an electron beam (white dashed line) passes parallel to a metallic grating, the grating can diffract the near-field (black glow) of the electron beam into far-field radiation, named as the Smith-Purcell radiation. The underlying mechanism is electron-induced dipoles in each grating line (blue arrow) that radiate constructively in a certain direction (green wavy arrows with an angle θ from the direction of the electron beam). Since the induced dipole is oriented in the electron beam direction (z-direction), the radiated light has a transverse magnetic (TM) polarization, with the electric field in the x-z plane (perpendicular to the grating lines) and the magnetic field in the y-direction (parallel to the grating lines). (b,c) Schematic of light emission from the interaction of free electrons and a metasurface consisting of C-aperture antennas with the C-opening oriented in the z(y)-direction. The unit cell of this metasurface is a C-aperture antenna, which has an effective electric dipole in the x-direction (out-of-plane direction), and an effective magnetic dipole in the y(z)-direction (across the C-opening). The electron beam directly induces the out-of-plane electric dipole, which then excites the magnetic dipole via antenna resonance coupling. As the magnetic dipole is oriented in the y(z)-direction, the radiated light again has a TM (TE) polarization, of which the electric field is in the x-z plane (y direction) and the magnetic field is in the y-direction (x-z plane).

5.2 Sample fabrication

We fabricated metasurfaces consisting of C-shaped nanostructures, and measured light emission from the metasurfaces driven by an electron beam. The metasurface fabrication process is illustrated in Figure 5.2a. The pattern of the metasurface was defined via electron beam lithography (EBL) in a thin layer (~ 40 nm) of hydrogen silsesquioxane (HSQ), a negative tone electron-beam resist, spin-coated onto a silicon substrate. Metasurface patterns were defined using electron beam lithography with a 125 keV electron beam (Elionix F-125). After exposure, the samples were developed in salty developer (1% NaOH and 4% NaCl in de-ionized water) and rinsed with water and IPA. Residual solvents were removed by oxygen plasma ashing. EBL and development produced C-shaped nanostructures made of cross-linked HSQ. Then a 30 nm gold layer was evaporated to form the metasurface. Figure 5.2b shows a low magnification SEM image of a fabricated metasurface. The metasurface is a periodic array of C-shaped nanostructures with 150 nm pitch in both vertical and horizontal directions. The patterned metasurface typically covers a 50 um × 100 um area on the substrate. We fabricated metasurfaces with different orientations of the C-shaped nanostructures, with two examples illustrated in the SEM images shown in Figure 5.2c and Figure 5.2d.

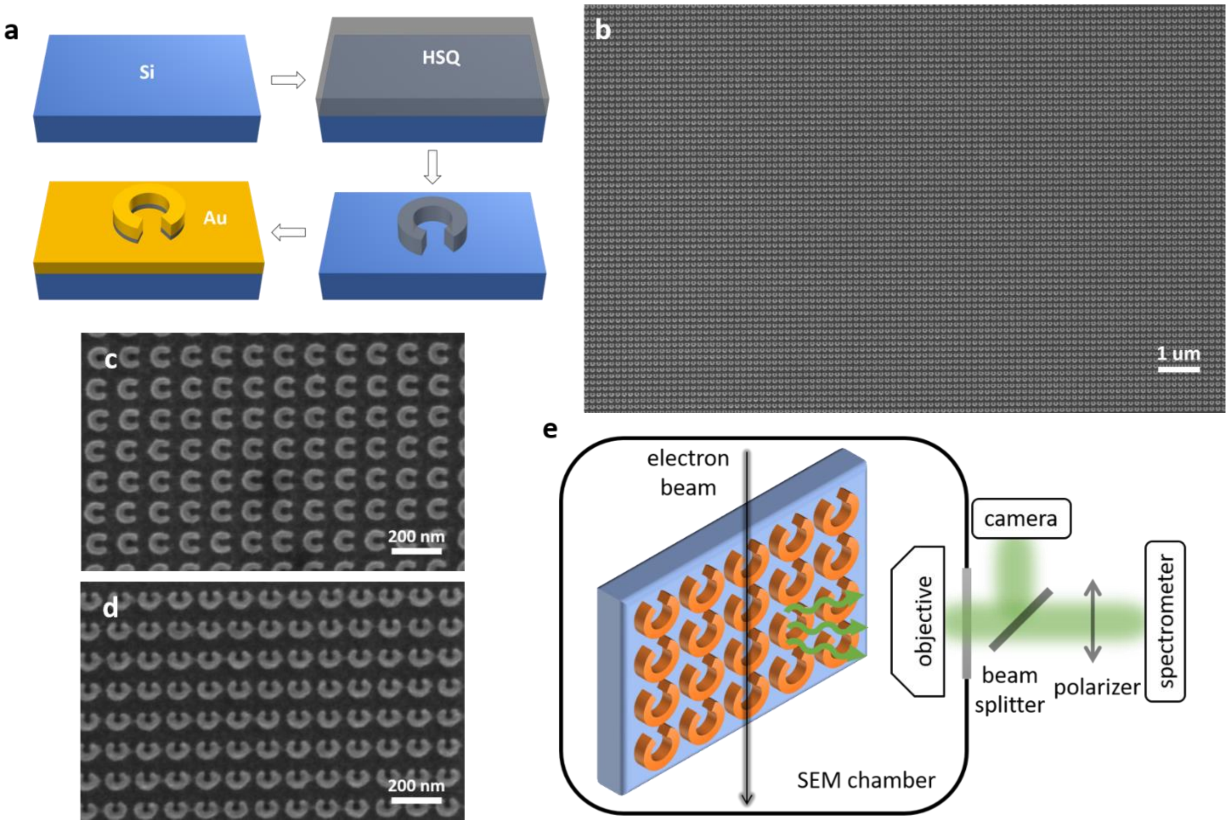

Figure 5.2. Metasurface structures and experimental setup. (a) Fabrication process flow of the metasurfaces. Starting from a silicon substrate, a thin layer (~ 40 nm) of HSQ, a negative tone electron-beam resist, is spin-coated onto the substrate. The patterns of the C-shaped nanostructures are defined via electron beam lithography. After development, a 30 nm gold layer is evaporated to form the metasurface. (b) An SEM image of a metasurface. The metasurface is a periodic array of C-shaped nanostructures. The array has 150 nm pitch in both horizontal and vertical directions. (c,d) Zoom-in SEM images of two metasurfaces with the C-shaped nanostructures oriented in orthogonal directions: the opening of the C-shaped nanostructure is facing the horizontal direction (c) or the vertical direction (d). (e) Experimental setup to measure the light emission from the metasurfaces. The metasurface is placed in an SEM chamber and is almost parallel to the electron beam of the SEM. Interaction between the electron beam and the periodic metasurface generates light emission (the Smith-Purcell radiation), which is collected by an objective lens and coupled out of the chamber through a transparent viewport. Via a beam splitter, part of the light is sent to a camera for imaging and alignment, and the other part is filtered by a polarizer and sent to a spectrometer.

5.3 Free-electron light emission from the metasurfaces

We measured the light emission from metasurfaces driven by an electron beam[1]. Figure 5.2e shows the experimental setup. A modified SEM provides the electron beam and the optical out-coupling [131]. The metasurface sample was mounted vertically on the SEM stage so that the electron beam was almost parallel to the metasurface. An objective lens collected light emitted in the normal direction to the metasurface and coupled light out of the SEM chamber via a transparent viewport. A beam splitter divided the emitted light and enabled both spatial imaging and spectral measurement.

The fabricated metasurfaces consist of C-aperture antennas similar to the theoretically proposed designs [146]. The C-shapes in the SEM images (Figure 5.2b-d) correspond to the metallic structures on top of the C-shaped HSQ nanostructures. In addition, the metallic film is covering the whole metasurface, as illustrated in the fabrication process (Figure 5.2a). The background metallic film appears dark in the SEM images due to low secondary electron emission. The optical property of cross-linked HSQ is very similar to that of silicon dioxide. Therefore, the fabricated nanostructures are essentially C-aperture antennas in the optical frequency, with dielectrics (HSQ) filled in the aperture gap.

Smith-Purcell radiation stems from the collective excitation of a periodic structure, and the radiation wavelength depends on the electron energy and the structure pitch. Figure 5.3 shows the measured Smith-Purcell radiation from the metasurfaces driven by free electrons. Background cathodoluminescence, measured by positioning the electron beam at an unstructured area on the sample, was subtracted from the raw emission spectra data. Figure 5.3a shows the light emission spectra of a metasurface driven by 18 keV electrons and 20 keV electrons. The opening of the C-

---

[1] Free-electron light emission measurement was performed together with Charles Roques-Carmes, Dr. Ido Kaminer, and Dr. Steven Kooi at Massachusetts Institute of Technology.

shaped nanostructure of this metasurface is facing the vertical direction. The emitted light is collected without a polarizer. For Smith-Purcell radiation, the emission wavelength decreases with increasing electron beam energy. The emitted light has a peak wavelength around 603 nm and 582 nm for electrons with a kinetic energy of 18 keV and 20 keV, respectively, in good agreement with the Smith-Purcell formula [115]. The emission wavelength is not pinned by the individual antenna resonance, but dependent on the collective behavior of the periodic metasurface that generates Smith-Purcell radiation.

For the metasurfaces driven by free electrons, the polarization of emitted light follows the orientation of the C-shaped nanostructures. Polarization resolved light emission was measured by inserting a polarizer before the spectrometer. Figure 5.3b-d presents the light emission spectra from metasurfaces with different orientations of the C-shaped nanostructures. The C-opening is facing the vertical direction (Figure 5.3b), 45° to the vertical direction (Figure 5.3c), and the horizontal direction (Figure 5.3d). The electron beam energy is 18 keV (Figure 5.3b-c) or 20 keV (Figure 5.3d). Light emission spectra in two orthogonal polarizations are shown: one is along the C-opening direction, and the other is perpendicular to it. As shown in Figure 5.3b-d, the emitted light is strongly polarized in the direction of the C-opening. Figure 5.3e shows the normalized light emission peak intensity with a polarization angle from 0° to 180° (measured from the electron beam direction) for metasurfaces with different orientations of the C-shaped nanostructures. Light emission data for different metasurfaces is vertically shifted for better visualization. It can be seen the light emission polarization follows the orientation of the C-shaped nanostructures. By designing the metasurface with C-shaped nanostructures in certain orientation, light emission polarized in that direction can be achieved. Specifically, as presented in Figure 5.3d, when the C-opening is facing horizontally, the emitted light is polarized in the horizontal direction, even with the electron beam in the vertical direction. This is in stark contrast to conventional Smith-Purcell radiation, where the radiation is strongly polarized in the direction of the electron beam [115].

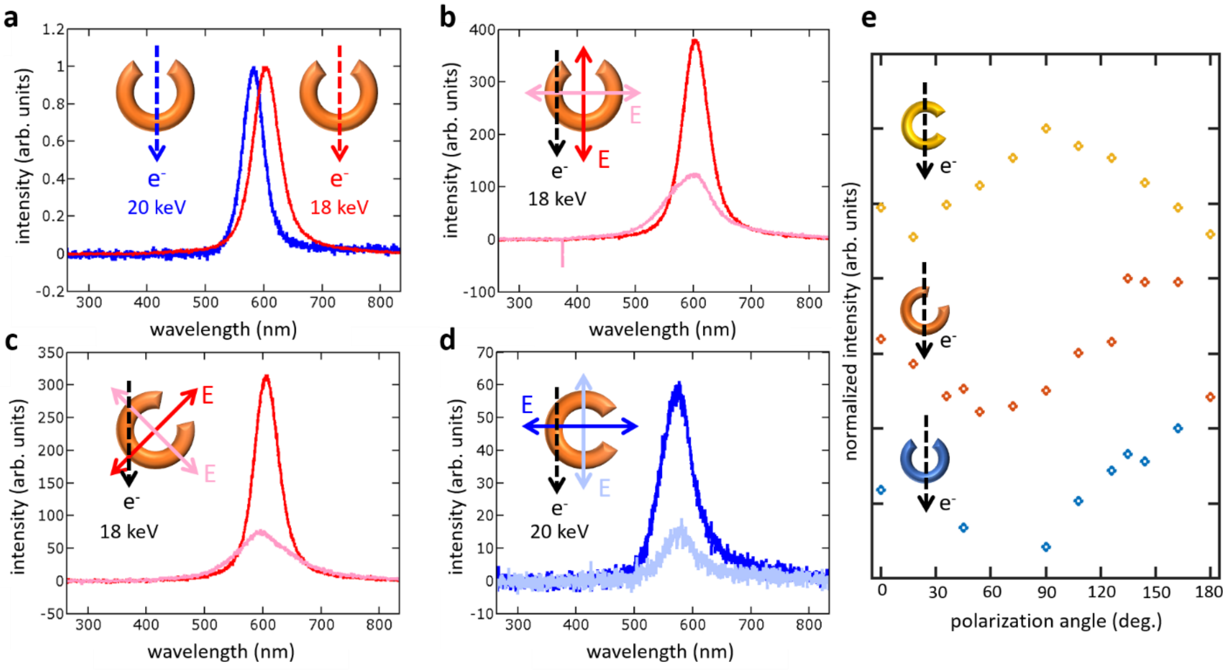

Figure 5.3. Measured Smith-Purcell radiation with tunable polarization from the metasurfaces driven by free electrons. (a) Free-electron-driven light emission spectra of the metasurface consisting of C-shaped nanostructures with the opening facing the vertical direction. The metasurface is driven by free electrons with 18 keV (red) and 20 keV (blue) energy. The emission is blueshifted with increasing electron energy, as predicted by the theory of Smith-Purcell radiation. (b,c,d) Free-electron-driven light emission spectra in orthogonal polarizations from metasurfaces consisting of C-shaped nanostructures with the opening facing the vertical direction (b), 45° to the vertical direction (c), and the horizontal direction (d). The free electron energy is 18 keV (red and light red) or 20 keV (blue and light blue). Each figure shows the spectra in two polarizations: one is in the C-opening orientation (red and blue), and the other is orthogonal to it (light red and light blue). (e) Normalized light emission peak intensity for different metasurfaces and different polarization angles (measured from the electron beam direction). Light emission data is recorded for three metasurfaces, with the C-opening facing the vertical direction (blue), 45° to the vertical direction (orange), and the horizontal direction (yellow). The data points for different metasurfaces are shifted vertically for better visualization. Insets: the C-shaped nanostructure orientation, the electron beam direction, and the polarizations of the spectra.

5.4 Summary

To summarize, we demonstrated polarization-tunable light emission from free-electron-driven metasurfaces. Visible light emission was obtained in the form of Smith-Purcell radiation when driving the periodic metasurfaces with an electron beam. The unit cell of the metasurfaces consisted of a C-shaped aperture nanoantenna, with its orientation controlling the polarization direction of the emitted light. Designed metasurfaces provided a solution to manipulate the polarization of free-electron radiation, which was widely considered to be fixed by the electron beam direction. We effectively developed a tunable nanoscale free-electron light source integrated with an adjustable polarizer. The combination of the spectral tunability of free-electron radiation with the metasurface-mediated polarization control could be particularly useful in the spectral range where conventional light sources and polarizers are inefficient or nonsexist. Our work takes a step towards compact and tunable free-electron-driven light sources with potential applications in nanophotonics research, on-chip integrated light sources, charged particle detectors and beam diagnostics, biomedical imaging and diagnostics. Future work might involve a better understanding of the optical response of the nanoantenna, metasurface designs that enable a full control of the polarization states including circular and elliptical polarizations, as well as material choices and structural engineering that push the operating frequency to shorter wavelengths.

Chapter 6

Nanostructured-membrane electron phase plates

Nanostructured material phase plates can impose designed phase modulations onto electron beams. These phase modulations can enable electron wavefront shaping and benefit electron microscopy, spectroscopy, lithography, and interferometry. Despite great flexibility in the phase plate design, this technique lacks tunability, as one phase plate can usually provide only one phase modulation, predetermined by its structure. In this chapter, we demonstrate that, by changing the electron energy, adjustable functions such as tunable diffraction efficiency can be achieved by a phase plate. We fabricate large-area mesh-shaped electron phase plates in a thin membrane with electron beam lithography and reactive-ion-etching. The phase plates are characterized by electron diffraction in a TEM with various electron energies, as well as diffractive imaging in an SEM.

This chapter is organized as follows. In Section 6.1, we introduce the electron phase plates, and briefly describe our nanostructured-membrane phase plates. In Section 6.2, we discuss the fabrication of the membrane phase plates. In Section 6.3, we show the characterization of the phase plates with electron diffraction in a transmission electron microscope (TEM). In Section 6.4, we show the phase plate achieves diffractive imaging in a scanning electron microscope (SEM). Finally, Section 6.5 summarizes our results.

6.1 Electron phase plates

Electron phase control, wavefront engineering and beam shaping are of vital importance in applications including electron microscopy, spectroscopy, and lithography. Conventionally, electron phase control is achieved via electric and magnetic fields, implemented by electron optics devices such as lenses and multipoles. Recently, phase plates have attracted a growing interest as a method to engineer the wavefront of electron beams. These phase plates are typically nanostructured electron-transparent membranes that impose certain phase modulations onto an incident electron beam. The phase plates have created a rich set of phase profiles in electron beams, including electron vortex beams [147–149], Airy beams [150], helicon beams [151], and arbitrarily sculptured wavefronts [152]. Although phase plates have great flexibility as various phase profiles can be created by changing the nanostructure patterns, one phase plate can usually provide only one phase modulation, predetermined by its structure, which cannot be changed once the phase plate is fabricated. A notable exception is a programmable phase plate of which pixelated phase modulation is achieved by micro-fabricated electrostatic-elements [153]. The static nature of the phase plates rendered their application inconvenient, as a new phase plate has to be fabricated and swapped into the electron beam path whenever a new functionality is required. For instance, in the electron beam shaping based on diffraction holograms, a specific diffracted beam is useful, and the surface profile of the phase plate needs to be carefully controlled to achieve the desired diffraction efficiency distribution for the diffracted beams [154]; but a new phase plate is required each time a different diffraction efficiency distribution is needed. Moreover, the diffraction efficiency can be different from the optimal design due to phase plate fabrication process variations, and it is desired to have an additional knob to fine tune the diffraction efficiency from a phase plate. Here, we demonstrate different phase modulation amplitudes can be created on one phase plate with a fixed structure by adjusting the electron energy. Indeed, this technique does not provide arbitrary phase profiles from one phase plate. But it does provide an alternative route towards the creation of electron phase plates with adjustable functions, such as the tunable diffraction efficiency shown in this chapter. We also employ electron beam lithography [151], rather than the more typically used focused ion beam milling [147,149,150,152,155], in the fabrication of these electron phase plates. Lithographic patterning enables high-throughput fabrication of a large-area nanostructured membranes with a small feature size and high density. Besides electron phase plates, these membrane nanostructures could also find a wide range of applications including diffractive elements for atoms [156], molecules [157], and X-rays [158], nanophotonic devices based on photonic crystals [159], separation processes based on nanoporous membranes [160], and nanopore single molecule sensing [161].

In this chapter, we discuss a mesh grating phase plate schematically illustrated in Figure 6.1. The mesh grating consists of a two-dimensional array of nano-holes patterned in a thin membrane. This mesh phase plate imposes a two-dimensional periodic phase shift to an incident electron beam. The electron beam passing through the mesh phase plate will be diffracted into multiple beams, with the direct beam (blue) and first-order diffracted beams (red) highlighted in Figure 6.1. The greyscale image at the bottom of Figure 6.1 is an electron diffraction pattern from a nanofabricated mesh phase plate experimentally measured in a transmission electron microscope.

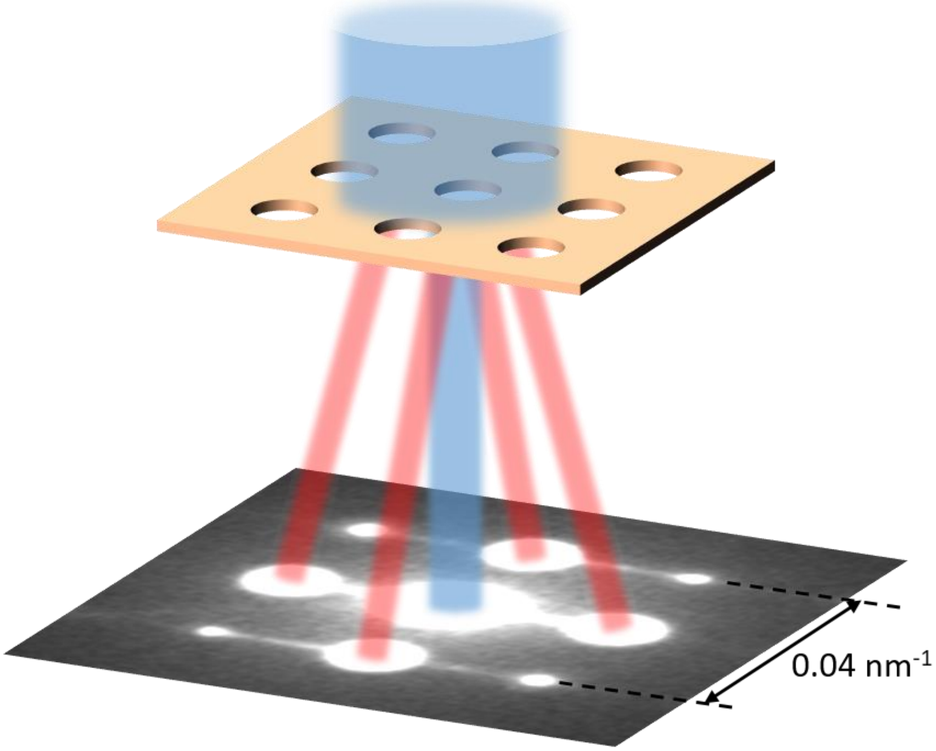

Figure 6.1. Electron diffraction from a mesh grating phase plate. The direct beam (blue) and four first-order diffracted beams (red) are shown in the schematic. The beam cross section image at the bottom is an electron diffraction pattern measured experimentally in a JEOL 2010F TEM with 200 keV electrons. The electron optics for focusing, diffraction, and imaging are not shown here.

6.2 Sample fabrication

We employed electron beam lithography and a reactive-ion-etching process to fabricate the mesh phase plates (Figure 6.2). We started from a silicon nitride membrane TEM grid (*SiMPore Inc.*), which had a 10 ± 0.5 nm nominal membrane thickness and was supported by a silicon frame with 250-µm-by-250-µm windows. A 25 s oxygen plasma ashing was used to clean the grid and promote resist adhesion. The grid was then stuck to a sacrificial silicon chip with carbon tapes for spin-coating. A PMMA thin film, a positive-tone electron-beam resist, was spin-coated with approximately 70 nm thickness. Resist soft-baking was performed at 180 °C for 2 min. The nanostructure pattern was defined by electron beam lithography via an Elionix F-125 system using 125 keV electrons. The exposure dose was 4800 ~ 6400 μC/cm^2 (300 ~ 400 e$^-$/nm^2). After exposure, cold development was performed at 0 °C in 3:1 IPA:MIBK. CF_4 reactive-ion-etching transferred the pattern into the membrane by etching through-holes. After etching, PMMA resist was stripped via a 90 s oxygen plasma ashing. After resist stripping, a metallic film was evaporated onto the sample. Metallization was performed by electron-beam evaporation of gold or aluminum with 10 nm nominal thickness. The purpose of the metallization is twofold: (i) the metal film reduces charging effects in the electron beam imaging and diffraction experiments; and (ii) this additional film gives us the ability to control the electron phase shift by varying the film composition and thickness.

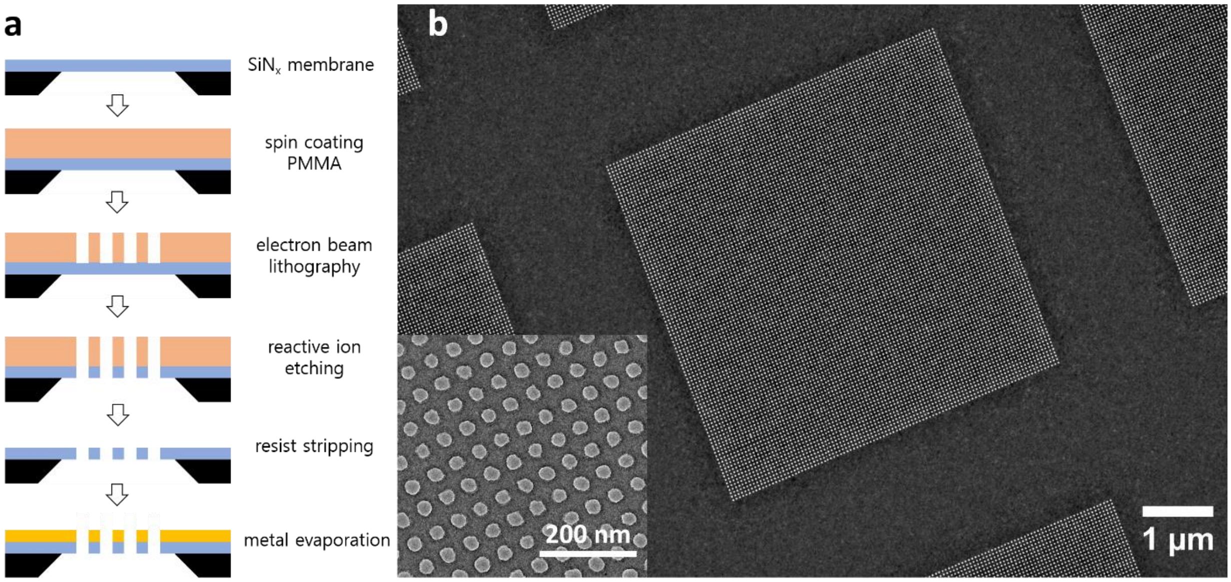

Figure 6.2. Fabrication of mesh phase plates. (a) Fabrication process flow. (b) A TEM image of the mesh phase plate. The image was acquired in a FEI Tecnai G2 TEM with 80 keV electrons. Inset: a TEM image of the nanostructured membrane at a higher magnification.

Figure 6.2b shows a TEM image of a typical nanofabricated mesh phase plate. The nanoscale through-holes in the membrane form a square-lattice with 50 nm pitch. There are 2-μm-wide supporting bars in the horizontal and vertical directions to maintain the mechanical strength of the membrane. Figure 6.3 illustrates the function of the supporting bars. Without the supporting bars, the defects (connected nano-holes) in the mesh can lead to a tearing of the nanostructured membrane. The supporting bars divide the nano-hole mesh into 5-μm-by-5-μm square regions. With the supporting bars, the defects are confined within the square regions, and the membrane is not broken. The patterned mesh covers a total area of 100-μm-by-100-μm on the membrane. We also fabricated nanostructured membranes with line grating patterns. However, for membrane gratings, the grating lines with a high aspect-ratio tended to stick together, making it difficult to fabricate large area phase plates (Figure 6.4). The mesh phase plates were free from this issue (Figure 6.5).

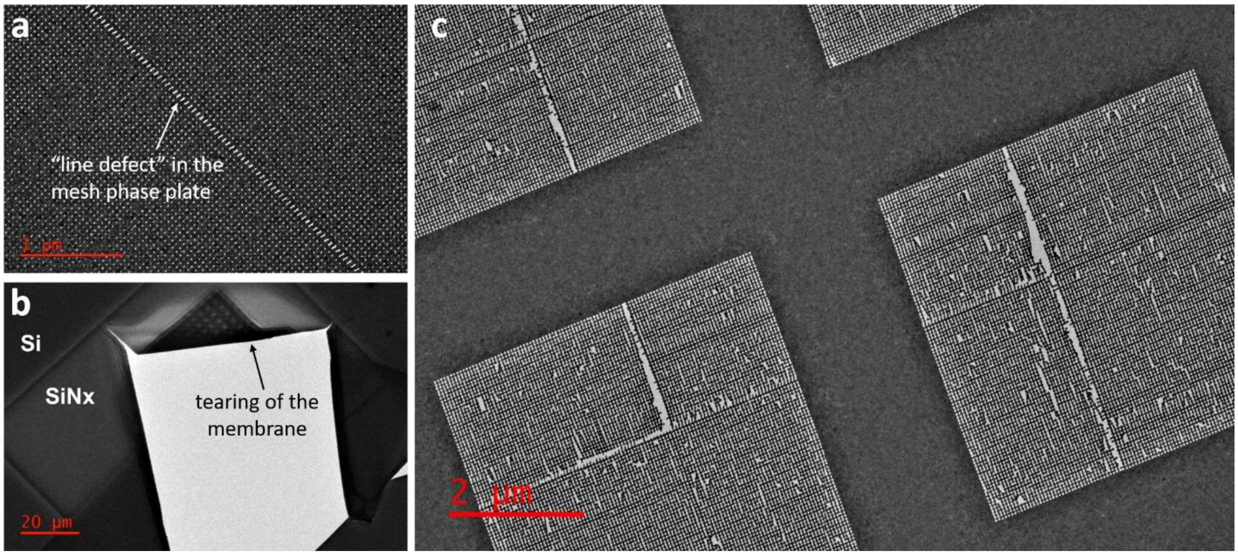

Figure 6.3. TEM images showing supporting bars maintain the mechanical strength of the nanostructured membrane. (a) Defects in the nanostructured membrane can occur along a line. (b) Without supporting bars, these defects eventually lead to a tearing of the nanostructured membrane. (c) With supporting bars, the defects are confined within the patterned area, and the membrane is not broken even with the presence of defects.

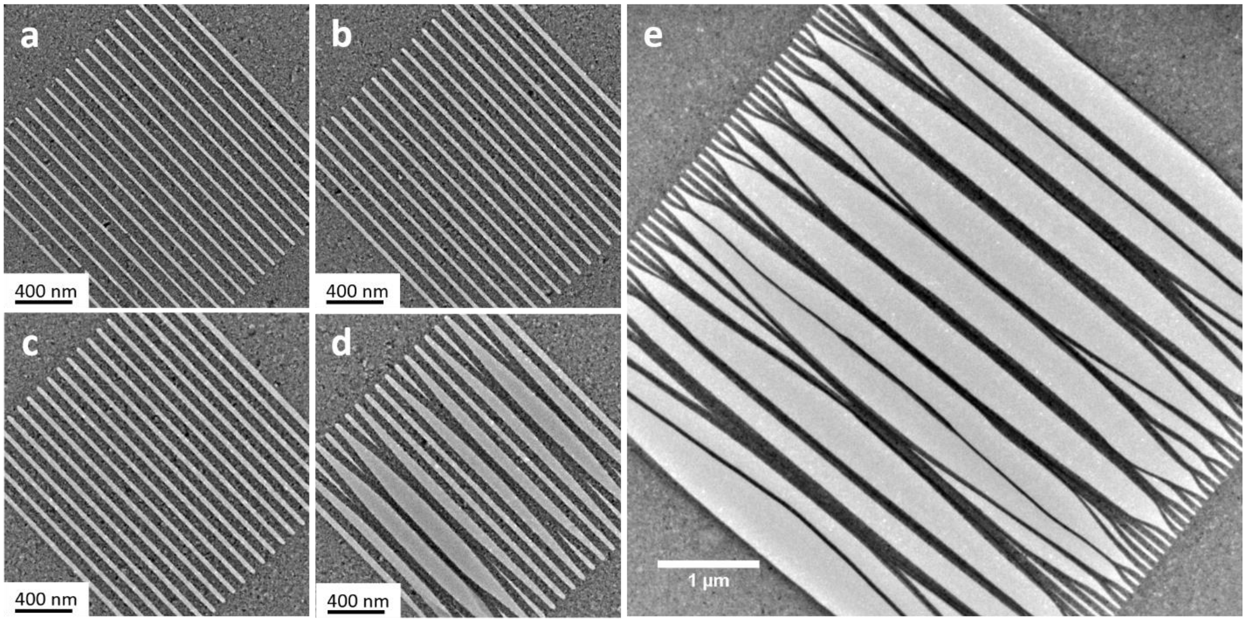

Figure 6.4. TEM images of line grating nanostructures in a membrane. (a-d) Gratings with 2-µm-long lines and various widths and hence aspect-ratios. For the grating with narrow and high aspect ratio lines (d), the adjacent grating lines tend to stick together. (e) A larger area grating with 6-µm-long lines. The grating lines have a high aspect-ratio and adjacent lines tend to stick together.

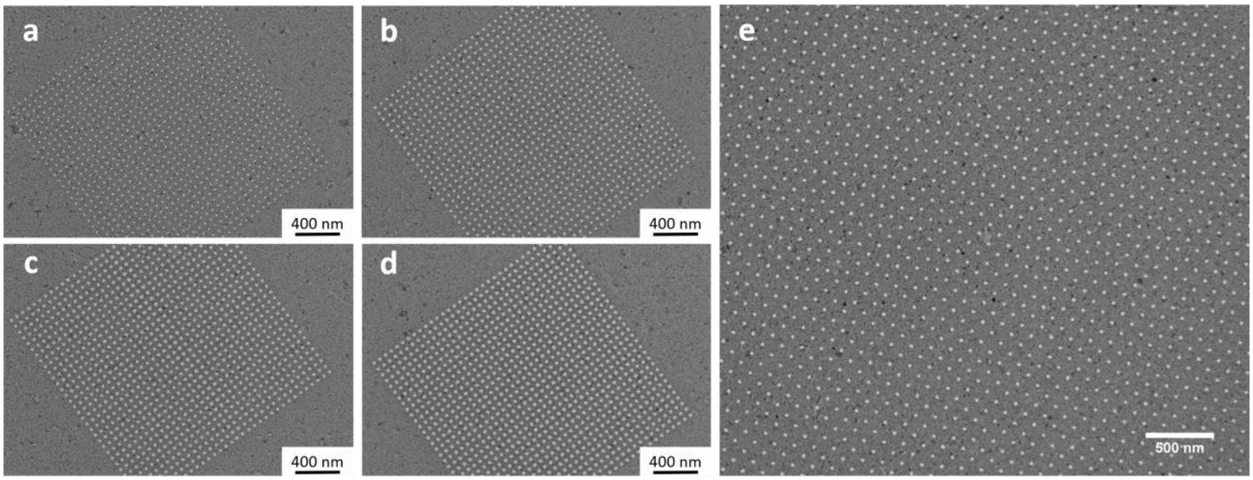

Figure 6.5. TEM images of mesh nanostructures in a membrane. (a-d) 2-µm-by-2-µm meshes with various sized nano-holes. (e) A larger area 6-µm-by-6-µm mesh. In contrast to line gratings, the meshes are free from defects.

We demonstrated lithographic pattern definition with electron beam lithography (EBL), followed by a pattern transfer step, is an alternative approach to typically used direct milling method with focused ion beam (FIB) in the fabrication of electron phase plates. Additive manufacturing of electron phase plates with EBL and a metal lift-off process was demonstrated in an earlier work [151] (the fabricated structure was considered as an amplitude mask in the work). We add capabilities to the EBL fabrication of electron phase plates by demonstrating subtractive manufacturing with a dry-etching step. Parallel pattern transfer with EBL enables a high throughput and is beneficiary to the production of large-area phase plates favored in shaping electron beam probes with a tight focus. Furthermore, by using an intermediate resist layer and a follow-up pattern transfer step, various materials can be patterned, including those that are hard to mill, and both additive and subtractive pattering techniques can be employed, enabling the production of phase plates with diverse materials and structures. We want to point out the same FIB tools used in direct milling can perform ion-beam lithography similar to EBL, demonstrating the wide applicability of the lithographic methods in various pattern generation tools.

6.3 Electron diffraction

The nanostructured electron phase plate was characterized with electron diffraction measurement using 200 keV electrons (JEOL 2010F TEM). Figure 6.6 shows the electron diffraction pattern as well as the high-dispersion electron diffraction pattern from the nanostructured mesh phase plate. A typical polycrystalline electron diffraction pattern was observed, with a central direct beam and several concentric rings. This diffraction pattern arose from the evaporated polycrystalline gold film. Given the pitch of the mesh nanostructure (50 nm) and the wavelength of 200 keV electrons (2.5 pm), the diffracted beams from the mesh phase plate should have a small angle (~50 μrad) and be located very close to the direct beam (~0.02 nm^{-1}). In order to observe the diffraction from the mesh phase plate, a high-dispersion electron diffraction pattern was taken (inset of Figure 6.6) in the low-magnification mode, in which the TEM objective lens was turned off. The electron beam illuminated a full window in the silicon nitride TEM grid containing the patterned mesh nanostructure. The electron diffraction pattern was recorded with a camera length of 80 m. In the high-dispersion electron diffraction pattern, a square lattice of diffraction spots was observed in the reciprocal space, corresponding to the mesh nanostructure in the real space. The diffraction spots were labelled according to crystallography conventions. The distance between the diffraction spots (0.02 nm^{-1}) was also commensurate with the pitch (50 nm) of the mesh phase plate. The periodic mesh nanostructure can be considered as an “artificial crystal” that produces an electron diffraction pattern with a well-defined lattice structure.

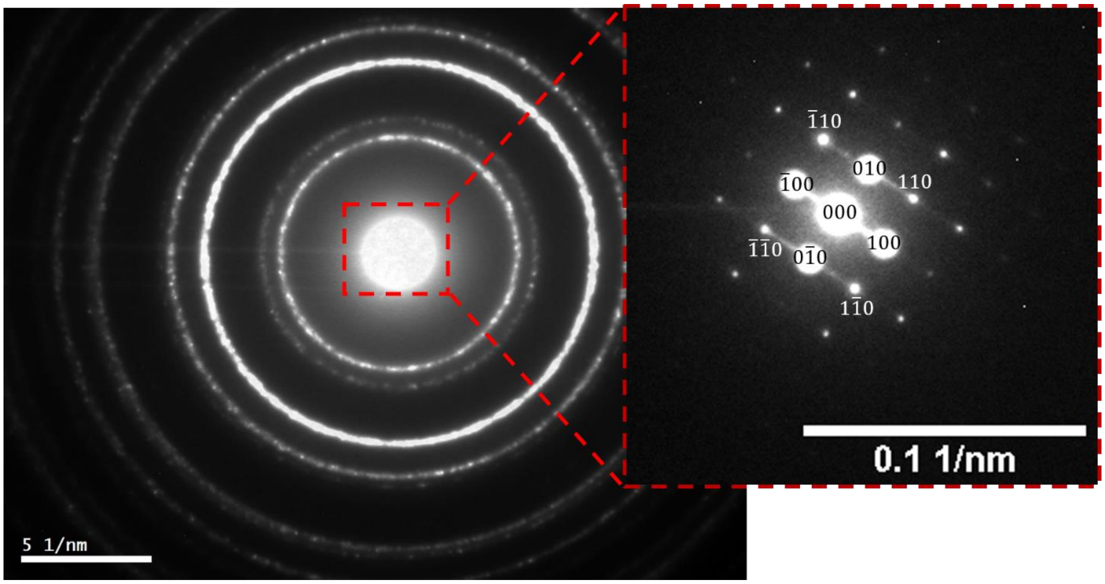

Figure 6.6. Electron diffraction patterns of the mesh phase plate. The electron-beam energy was 200 keV. The diffraction pattern consists of a bright spot in the center representing the direct beam and a series of concentric rings coming from electron diffraction by the polycrystalline gold film. Inset: high-dispersion electron diffraction pattern of the nanostructured membrane. Note the focus and stigmation were re-adjusted to obtain the high-dispersion electron diffraction pattern. The square lattice in the reciprocal space corresponds to the mesh structure in the real space. The diffraction spots were labeled according to crystallography conventions.

Changing the phase profile of a phase plate can modify its diffraction pattern. We changed the phase profile of the mesh phase plate by adjusting the electron-beam energy, thus modulating the intensities of different diffraction orders. The electron diffraction experiment was conducted in a FEI Tecnai G2 TEM with its beam energy adjustable from 20 keV to 120 keV. Figure 6.7 shows the TEM image of the mesh phase plate and its selected-area electron diffraction patterns at various electron-beam energies. In order to resolve the diffraction pattern from the mesh phase plate, the incident electron beam was spread out to ensure a small convergence angle and hence small spots in the diffraction pattern. A selected-area aperture selected a region on the mesh phase plate without supporting bars so that the diffraction came from only the mesh structure. The electron diffraction patterns were recorded with a camera length of 4.2 m. In the diffraction patterns, the zeroth ({000}), first ({100}), and second ({110}) diffraction orders are most visible. Higher diffraction orders are much weaker, consistent with theoretical calculation. The diffraction efficiency, namely the relative intensity of different diffraction orders, was modulated by the beam energy. The diffraction efficiency modulation was most obvious in the diffraction pattern from 60 keV electrons, where the direct beam was suppressed compared to first-order and second-order diffracted beams (Figure 6.7c). The modulation of diffraction intensities by changing the beam energy (and hence the phase shift) is analogous to oscillations of diffraction intensities with sample thickness (and hence the phase shift) in crystal diffraction. We interpret this diffraction intensity modulation as an effective Pendellosung effect [162] in an artificial nanostructure.

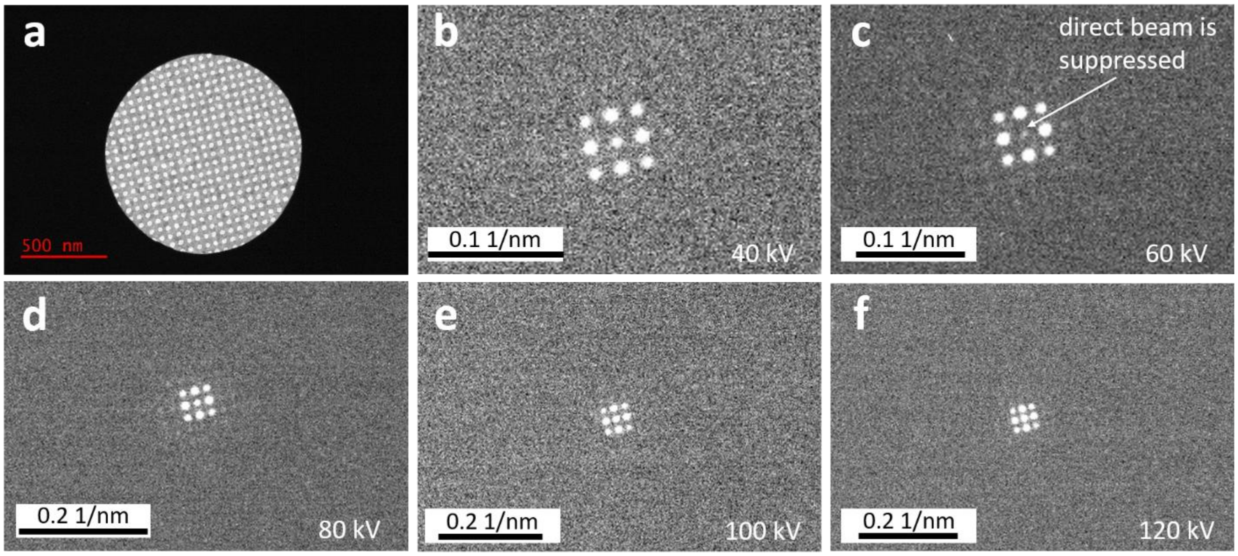

Figure 6.7. Selected-area electron diffraction patterns from the nanostructured membrane using electron beams with various energies. (a) A TEM image of the nanostructured membrane and the selected-area aperture. (b-f) Selected-area electron diffraction patterns with a 40 keV (b), 60 keV (c), 80 keV (d), 100 keV (e), and 120 keV (f) electron beam.

For a quantitative comparison of the mesh phase plate electron diffraction patterns at different electron energies, we measured the intensity ratio between the direct beam (I_0) and the first-order diffracted beam (I_1) (averaged from the four first-order diffracted beams: (100), $(\bar{1}00)$, (010), $(0\bar{1}0)$) (Figure 6.8). The beam intensity was measured from the diffraction pattern by first subtracting the background and then integrating the intensity around the corresponding diffraction spot. To minimize the artifacts of the TEM image recording system, we took the same diffraction pattern with several different exposure times. For one phase plate at one electron energy, the beam-intensity ratio should be constant. We only used diffraction patterns with an intermediate exposure time and they produced similar beam-intensity ratios. Diffraction patterns with a low exposure time was susceptible to noise, while diffraction patterns with a high exposure time suffered from camera saturation. At the intermediate exposure time, 6-16 electron diffraction patterns (varies for different electron energies) were used to produce the average value and the standard deviation of one experiment data point showing the beam intensity ratio in Figure 6.8. In Figure 6.8, it was confirmed that, by changing the electron energy, and hence the phase profile of the mesh phase plate, the intensities of diffracted beams could be modulated.

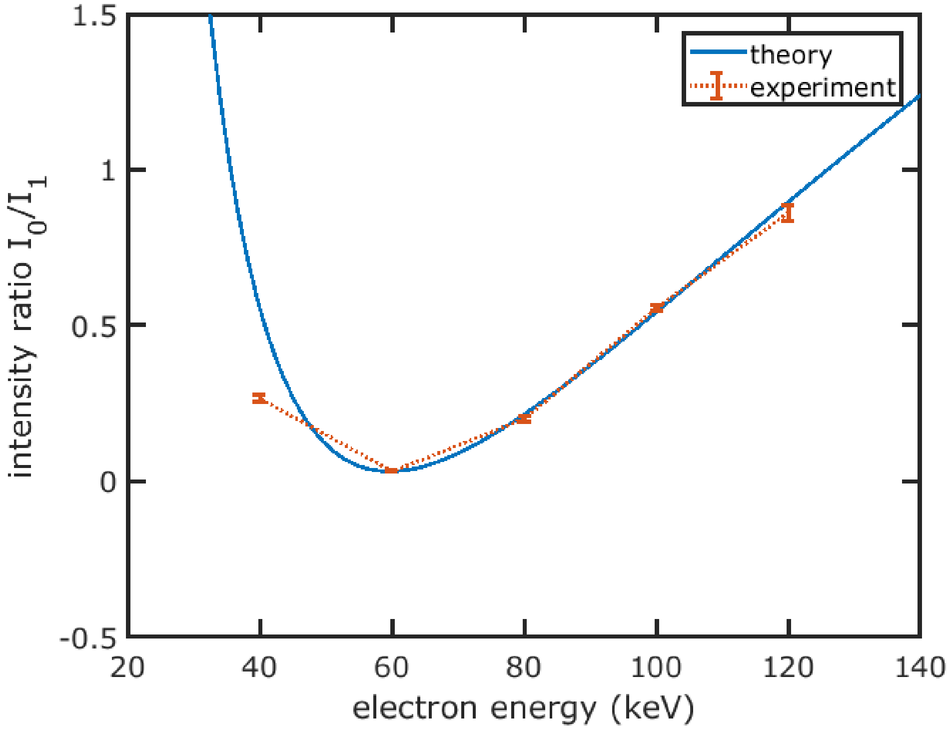

Figure 6.8. Experimental and theoretical beam-intensity ratio between the direct beam (I_0) and the first-order diffracted beam (I_1) as a function of electron-beam energy. Each of the experimental data point was obtained by measuring the beam-intensity ratio from electron diffraction patterns taken at 8-15 (varies for different electron energies) different exposure times, with the error bars showing the standard deviations.

The measured beam-intensity ratio was verified by theoretical modeling of electron diffraction from the mesh phase plate. The mesh phase plate was modeled as a uniform film with a periodic hole array in it. The mesh was considered as a mixed amplitude and phase plate. When a free electron passes through a thin film, the phase shift (relative to propagation in free space) can be described as [163]

$$\Delta\phi_0 = C_0 V_{\mathrm{MIP}} t_0 = \frac{2\pi \mathrm{e}(E + \mathrm{E}_0)}{\lambda E(E + 2\mathrm{E}_0)} V_{\mathrm{MIP}} t_0 \tag{6.1}$$

where C_0 is a constant depending on electron energy, V_{MIP} is the material mean inner potential (MIP), t_0 is the material thickness, e is the electron charge, λ is the electron wavelength, E is the electron kinetic energy, and E_0 is the electron rest energy. Thus, the phase plate is binary, with 0 phase shift in the holes and $\Delta\phi_0$ phase shift in the membrane structure. Note the $\Delta\phi_0$ phase shift is electron-energy dependent as well as material dependent. For the amplitude modulation, a constant transmission factor α was applied to the electron wave passing through the material phase plate. The electron diffraction pattern was calculated as the Fourier transform of the mesh phase plate. The analytical Fourier coefficients are

$$c_{m,n} = \alpha e^{\mathrm{i}\Delta\phi_0} \frac{\sin(m\pi)}{m\pi} \frac{\sin(n\pi)}{n\pi} + (1 - \alpha e^{\mathrm{i}\Delta\phi_0}) \frac{\pi d^2}{2p^2} \frac{\mathrm{J}_1(\pi d\sqrt{m^2 + n^2}/p)}{\pi d\sqrt{m^2 + n^2}/p} \tag{6.2}$$

where integer pair (m, n) denotes the diffraction order, d is the hole diameter, p is the array pitch, and J_1 is the Bessel function of the first kind with order 1. The diffraction intensity is hence $I_{m,n} = |c_{m,n}|^2$. The Fourier transform was also calculated numerically, producing the same results as the analytical analysis. The hole diameter $\mathrm{d} = 28$ nm was measured from a typical TEM image of the phase plate by averaging over ~200 nano-holes. The calculated beam-intensity ratio between the first-order diffracted beam and the direct beam is shown in Figure 6.8. The best fit between theoretical and experimental diffraction beam-intensity ratios was obtained by setting the MIP-thickness product to $276\ \mathrm{V \cdot nm}$ and the amplitude transmission factor to 0.41. The fitted MIP-thickness product appears smaller than the estimated value assuming 10 nm thickness for both Au and Si_3N_4, and 21 V MIP for Au [163] and 14 V MIP for Si_3N_4 [155]. We attribute this discrepancy to the following potential causes: (i) beam-energy-dependent inelastic scattering and high-angle diffraction from the phase plate are not considered in the theoretical model; (ii) the actual material thicknesses are different from the nominal thicknesses; (iii) the material density and composition can vary depending on the fabrication conditions and material thickness (e.g. the Au film was only ~10 nm thick and could be different from the bulk Au, resulting in a lower MIP); and (iv) the pattern of the fabricated phase plate can be different from the ideal circular hole arrays.

The intensity ratio between the second-order diffracted beam (I_2) (averaged from the four second-order diffracted beams: (110), $(\bar{1}10)$, $(1\bar{1}0)$, $(\bar{1}\bar{1}0)$) and the first-order diffracted beam (I_1) was also experimentally measured and theoretically calculated (Figure 6.9). In theory, the intensity ratio I_2/I_1 is a constant. This constant intensity ratio between diffracted beams is a direct result of the binary phase modulation imposed by the phase plate, and this constant only depends on the phase plate pattern and the diffraction orders, free from any fitting parameters (see Equation (6.2)). In experiments, the intensity ratio I_2/I_1 slightly increases with a decreasing electron energy. This increase could be caused by the fact that electrons with a lower energy are subject to a stronger scattering by the phase plate material, leading to a higher relative intensity of the second-order diffracted beams as they have a larger scattering angle.

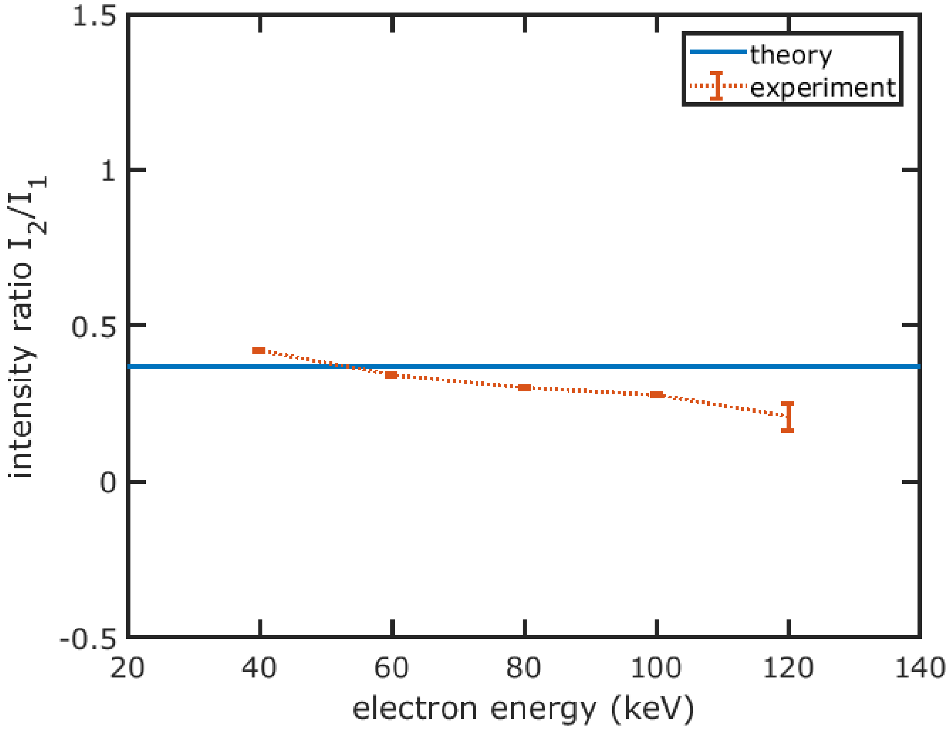

Figure 6.9. Experimental and theoretical beam-intensity ratio between the second-order diffracted beam (I_2) and the first-order diffracted beam (I_1) as a function of electron-beam energy. Each of the experimental data point was obtained by measuring the beam-intensity ratio from electron diffraction patterns taken at 8-15 (varies for different electron energies) different exposure times, with the error bars showing the standard deviations. In theory, the intensity ratio I_2/I_1 is a constant, since the phase plate impose a binary phase modulation. In experiments, the intensity ratio I_2/I_1 slightly increases with a decreasing electron energy. This increase could be caused by the fact that electrons with a lower energy are subject to a stronger scattering by the phase plate material, leading to a higher relative intensity of the second-order diffracted beams as they have a larger scattering angle.

The phase profile of the phase plate could also be changed by using different material compositions. We fabricated mesh phase plates with an aluminum film instead of a gold film on top of the silicon nitride membrane. The selected-area electron diffraction patterns for various electron energies are shown in Figure 6.10. The intensity distribution among diffraction orders of an aluminum-coated mesh phase plate is different from that of a gold-coated mesh phase plate. For instance, the direct beam was never suppressed for all the electron energies tested.

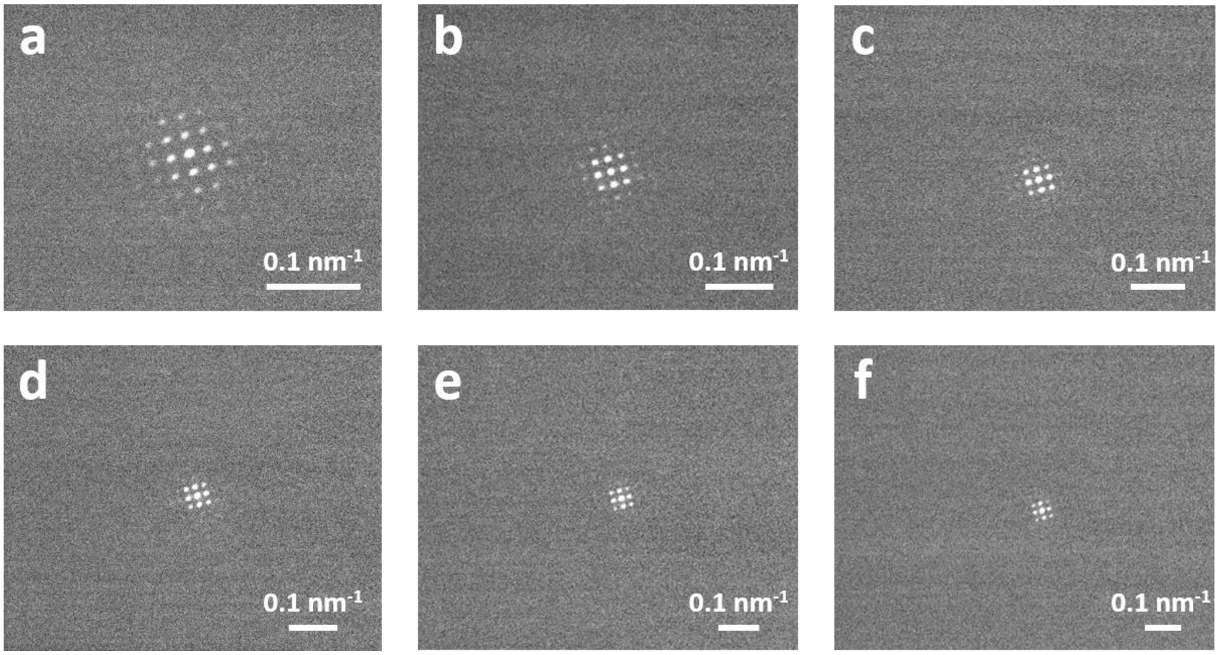

Figure 6.10. Selected-area electron diffraction patterns from an Al-coated nanostructured membrane. The electron-beam energy is 20 keV (a), 40 keV (b), 60 keV (c), 80 keV (d), 100 keV (e), and 120 keV (f).

For the aluminum-coated mesh phase plates, the measured and calculated beam-intensity ratios (I_0/I_1 and I_2/I_1) are shown in Figure 6.11. The best fit between theoretical and experimental diffraction beam-intensity ratios was obtained by setting the MIP-thickness product to $200\ \mathrm{V \cdot nm}$ and the amplitude transmission factor to 0.68. Both a lower MIP-thickness product and a higher amplitude transmission factor are expected by changing the Au film to the Al film. The aluminum-coated mesh phase plates also presented a constant intensity ratio I_2/I_1 that was well reproduced in the theory. Compared with gold-coated phase plates, the closer fitting of I_2/I_1 between theory and experiments could be a result of weaker energy-dependence of the electron scattering.

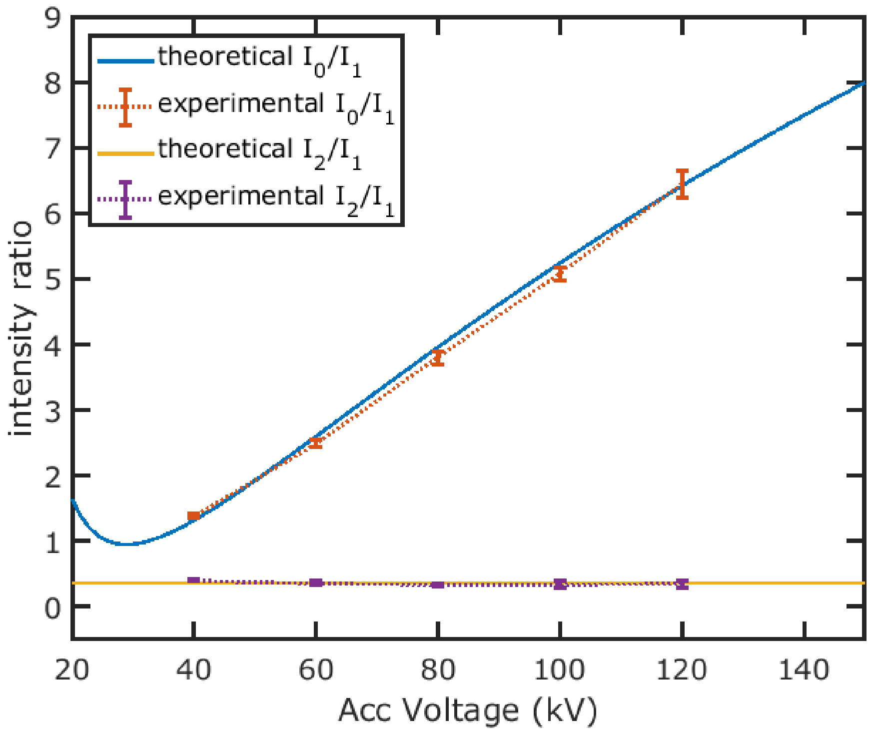

Figure 6.11. Experimental and theoretical beam-intensity ratios (I_0/I_1 and I_2/I_1) for the Al-coated nanostructured membrane. Each of the experimental data point was obtained by measuring the beam-intensity ratio from electron diffraction patterns taken at 14-20 (varies for different electron energies) different exposure times, with the error bars showing the standard deviations. The best fit between theoretical and experimental diffraction beam-intensity ratios was obtained by setting the MIP-thickness product to $200\ \mathrm{V} \cdot \mathrm{nm}$ and the amplitude transmission factor to 0.68 (due to the almost linear behavior of the experimental data, similar goodness of fit was also obtained by using a slightly smaller MIP-thickness product and a slightly larger amplitude transmission factor, or using a slightly larger MIP-thickness product and a slightly smaller amplitude transmission factor). Both a lower MIP-thickness product and a higher amplitude transmission factor are expected by changing the Au film to the Al film.

6.4 Diffractive imaging

We further performed diffraction experiments using the large-area nanostructured phase plates to produce diffractive images in a scanning electron microscope (SEM) [164]. Diffractive imaging was performed in a modified Zeiss LEO 1525 SEM. The electron energy was 20 keV. Figure 6.12a shows the experimental setup. The mesh phase plate is inserted in the beam path of the SEM and functions as a diffraction grating. The beam spot size on the phase plate was estimated by using the edges of the window in the silicon frame as knife edges (Figure 6.12b), and measuring the image grayscale along a line-scan across the knife edge. The estimated beam spot size was 57 μm on the phase plate. While the SEM electron beam is scanning across the sample, multiple diffracted beams are also scanning across the sample and generating multiple superimposed images with small offsets. Figure 6.12b is a low magnification SEM image showing the sample to be imaged as well as the membrane TEM grid with the mesh phase plate (opaque region is the silicon frame and transparent region is the membrane). The sample contained Sn nanoparticles with various sizes, with the SEM image (without the diffraction grating) shown in Figure 6.12c. A PELCO STEM imaging holder (*Ted Pella Inc.*) was used to hold both the nanostructured membrane phase plate and the Sn nanoparticle sample with ~18 mm separation. The electron beam was focused at the Sn nanoparticles and diffractive imaging was acquired from the secondary electron signal at the Everhart-Thornley detector of the SEM. Figure 6.12d illustrates a diffractive image of the sample, showing multiple superimposed and displaced images of the nanoparticles. A fast Fourier transform (FFT) of the diffractive image is also shown, with its spatial frequency components resembling the electron diffraction pattern of the mesh phase plate.

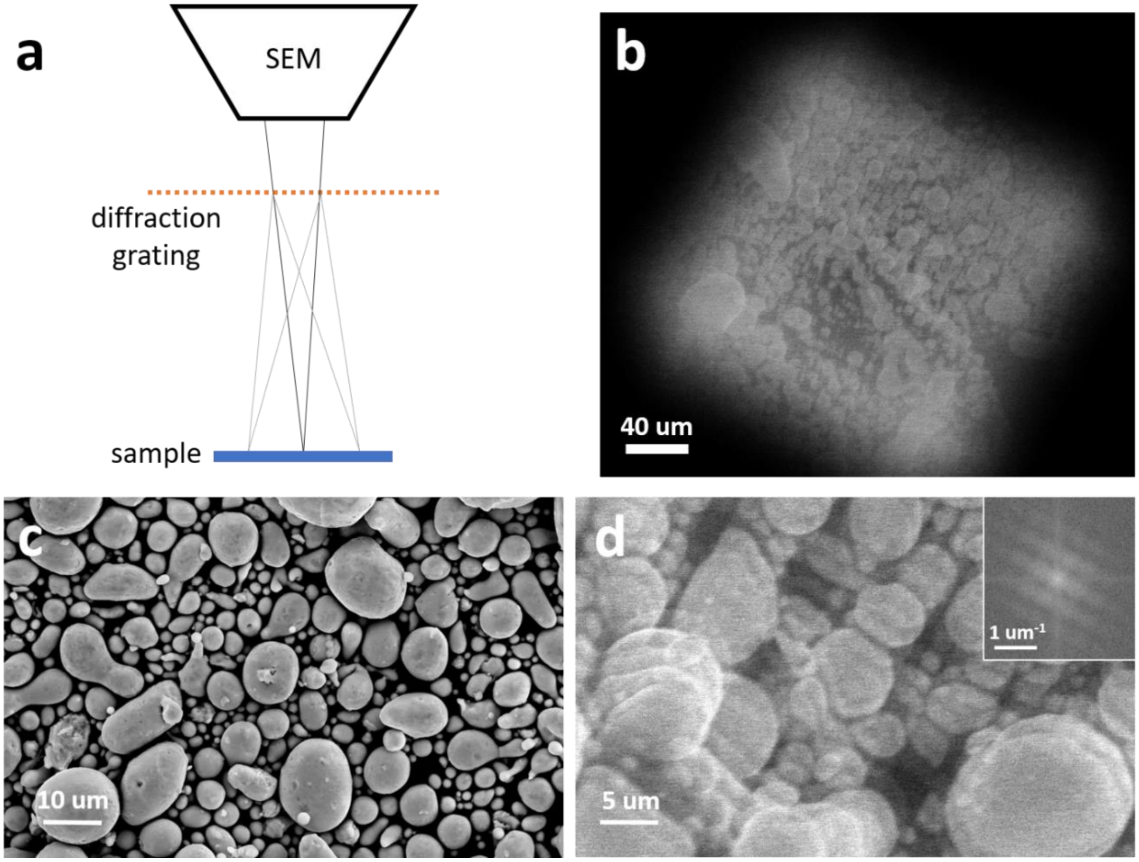

Figure 6.12. SEM diffractive imaging with the nanostructured membrane. (a) Experimental setup of diffractive imaging. The nanostructured membrane diffraction grating is inserted into the beam path between the SEM column and the sample. The estimated beam spot size was 57 μm on the phase plate. The SEM electron beam is diffracted by the membrane into multiple beams focused at the sample. As these beams scan across the sample, multiple superimposed and displaced images are generated. (b) An SEM image of diffractive imaging of Sn nanoparticles, showing the nanostructured membrane (transparent square region) and its Si supporting frame (opaque region). (c) A regular SEM image (without the diffraction grating) of Sn nanoparticles used as the sample for diffractive imaging. (d) A diffractive SEM image of the Sn nanoparticles. Inset: a fast Fourier transform (FFT) of the image.

6.5 Summary

To summarize, we demonstrated adjustable phase modulation and diffraction efficiency from an electron phase plate by changing the electron energy. The phase plate was fabricated with electron beam lithography and reactive-ion-etching, and covered a large area on an electron-transparent membrane. We characterized the phase plate with electron diffraction in TEMs as well as diffractive imaging in an SEM. This work provides an alternative route towards the creation of electron phase plates with adjustable functions, such as tunable diffraction efficiency. The concept shown here can be applied to, for example, improving diffraction efficiency for beam shaping using diffractive hologram phase plates, of which the diffracted beams, rather than the direct beam, are desired.

Chapter 7

Efficient two-port electron beam splitters via quantum interaction-free measurement

A beam splitter is a device that splits one beam of wave, such as electromagnetic wave and matter wave, into two beams. Beam splitters are crucial parts of both classical and quantum experiments. Many of these experiments require a coherent and efficient two-port beam splitter. In light optics, efficient two-port beam-splitting can be achieved by devices such as a half-silvered mirror, a waveguide coupler, or a fiber switch. However, for electron optics, coherent and efficient two-port splitting cannot be readily achieved. In this chapter, we propose a design of an efficient two-port electron beam splitter using the concept of quantum interaction-free measurement (IFM). Our design combines an electron resonator and a weak phase grating. We use a scattering matrix method to analyze the performance of the beam splitter. High-order diffraction from the grating leads to intensity loss in the two-port beam splitter. We employ an aperture to block high-order diffraction while minimizing loss and improving efficiency by invoking the concept of quantum IFM. This design can be generalized to beam splitters for not only electrons, but also photons, neutrons, atoms, and other quantum mechanical systems. Part of the content in this chapter was derived from the work in [165].

This chapter is organized as follows. In Section 7.1 and Section 7.2, we introduce the electron beam splitters and the quantum interaction-free measurement, respectively. In Section 7.3, we introduce the scattering matrix method for theoretical calculation, and analyze the working principle of the beam splitter under the simplest scenario—the two-beam condition—by considering only two beams in the case of crystal diffraction. In Section 7.4, we analyze the beam splitter by taking into account high-order diffracted beams in the case of a nanofabricated grating, and propose to reduce the intensity loss due to high-order beams with a beam-blocking aperture. In Section 7.5, we show the aperture performs quantum IFM on the electron, evaluate the total intensity loss of the beam splitter, and discuss the effect of electron inelastic scattering. Finally, Section 7.6 summarizes our results.

7.1 Electron beam splitters

Electron beam splitters divide an input electron beam into multiple output beams, and are commonly used in applications including electron interferometry [166], holography [167], imaging [168], and spectroscopy [147]. Many of these applications require a coherent two-port electron beam splitter with minimal loss of the beam intensity. Existing electron beam splitters can split incident electron beams, but can hardly split the beam into only two beams without beam intensity loss.

Several types of electron beam splitters have been developed, including biprisms [169], thin crystals [170], optical standing waves [171], and nanofabricated gratings [149,154,172,173]. Electron biprisms are commonly used electron beam splitters for electron interferometry and holography. Biprisms split the input electron beam into two output beams by the electrostatic force of a charged wire. However, a biprism placed in the beam inevitably blocks part of the beam and causes diffraction around the wire edges, which leads to beam intensity loss. Furthermore, biprisms are wavefront-division beam splitters, which divide the wavefront of the input beam. Wavefront-division beam splitters require a high-spatial-coherence electron beam [174]. Also, this type of beam splitters cannot split a beam with a pattern (such as certain spatial profiles achieved by amplitude or phase modulation) in it, and hence cannot be applied to some emerging electron beam technologies that use quantum mechanical effects [168,175]. Thin crystals have been used as amplitude-division electron beam splitters. This type of beam splitters has a less stringent requirement on the coherence of input beam, leading to a higher beam intensity by using extended sources and a larger interference field [174]. However, electron diffraction from crystals results in multiple diffracted beams. In order to achieve a two-port beam splitter, high-order diffracted beams need to be blocked, leading to intensity loss. Optical standing waves can diffract electron beams based on the Kapitza-Dirac (KD) effect [171]. The advantage of beam splitter based on the KD effect is that electrons do not go through or near materials, and as a result, decoherence caused by inelastic scattering can be minimized. However, the KD effect requires high quality laser beams and good alignment, and high-order diffracted beams still exist. Recently, nanofabricated gratings have been proposed as electron beam splitters [149,154,172,173]. These beam splitters are amplitude-division beam splitters. Additionally, nanofabrication enables the production of arbitrary patterns to impose spatial modulations onto the input beam, inspiring novel applications such as vortex beam generation [147,149,154]. For electron energies typically used in electron microscopy, thin membrane nanofabricated gratings are electron-transparent with small intensity loss caused by inelastic scattering. However, similar to other diffraction-based electron beam splitters, high-order diffracted beams still causes beam intensity loss. For instance, it has been reported a silicon nitride membrane grating shows ~34% maximal diffraction efficiency for the first order beam [154].

Several attempts have been made to improve the efficiency of existing electron beam splitters. For biprisms, selection of a small-diameter wire reduces the intensity loss [173]. For thin crystals and optical standing waves, the Bragg regime can be achieved by tilting the beam splitters with respect to the input beam, so that only two beams (the direct beam and one diffracted beam) are strongly excited (the "two-beam" condition). However, even in the Bragg regime, there are finite intensities in high-order diffracted beams. For instance, it has been reported that, in the Bragg regime (for (+1)-order diffracted beam) of optical standing wave electron diffraction, the (-1)-order and (+2)-order diffracted beams are clear visible in both theory and experiment, and the intensity in the (-1)-order diffracted beam is about half of the intensity of the (+1)-order [176]. For nanofabricated gratings, the diffraction efficiency can be increased by moving from amplitude gratings to phase gratings by using thinner membranes and lower-atomic-number materials, as well as controlling the surface profiles of the gratings [154]. All of these efforts help improve the efficiency of various types of electron beam splitters, but the intensity loss has never been eliminated.

7.2 Quantum interaction-free measurement

Quantum mechanical interaction-free measurement (IFM) was first proposed by Elitzur and Vaidman as a method of detecting an object without interacting with it [177]. In quantum IFM, a single probe particle (e.g. a single photon) is sent to a Mach-Zehnder interferometer (MZI). The object (if there is any) is placed in one of the two arms of the MZI. The object fully blocks the probe particle if the particle hits the object. The presence of this object changes the output state of the MZI, and in principle it is possible to detect the object without particle-object interaction, namely, the particle is not blocked by the object. The quantum IFM has been further developed by adding the quantum Zeno effect [178]. By cascading multiple stages of MZIs and using asymmetric beam splitters, efficient quantum IFM can be realized. The IFM efficiency can approach unity by repeatedly interrogating the object with a small fraction of the probe particle wavefunction, while the probability of particle-object interaction simultaneously tends to zero. While early reports on quantum IFM use photons as the probe particles, recent works have proposed quantum IFM with electrons to reduce sample damage in electron imaging [168,175].

In this chapter, we propose a highly efficient two-port electron beam splitter using the quantum IFM concept. The beam splitter is based on electron diffraction, while the high-order diffracted beams are suppressed with minimal intensity loss. In theory, the beam splitter efficiency can be made arbitrarily close to unity.

7.3 Case study: a thin crystal grating

In this section, we will introduce the proposed beam splitter design, and analyze it in the case of using a thin crystal as a component of the beam splitter. Our beam splitter design consists of a weak phase grating placed in a resonator (Figure 7.1(a)). The beam splitter has one input port and two output ports. The beam splitter works with a pulse electron beam, and the input and output ports have gates to control the entrance and exit of the electron. The input electron enters the resonator through the input port, after which the input port gate is closed and the electron starts to bounce back and forth in the resonator (the output port gates remain closed). We assume the weak phase grating imposes a pure phase modulation onto the electron beam without amplitude modulation. The electron passes through the grating multiple times when it is resonating, and is diffracted by the grating.

In this section, we consider the two-beam condition and assume there is only one diffracted beam. Before interacting with the grating, the electron is in the direct beam with unity probability. After each pass through the grating, a small fraction of the electron wavefunction is diffracted into the diffracted beam. This fraction is small as a weak phase grating is used. With the electron passing through the grating multiple times, the probability of the electron occupying the diffracted beam builds up. After a certain number of passes, the output port gates open and the direct and diffracted beams exit via the output ports. The beam splitting ratio (the relative intensity between the two output beams) can be tuned by changing the number of passes through the grating.

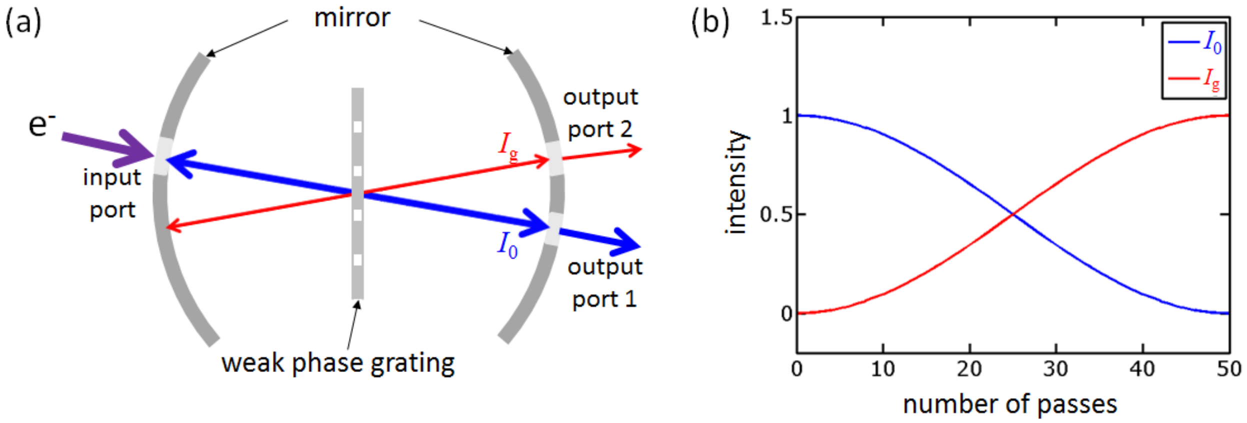

Figure 7.1. Electron beam splitter design in the two-beam condition. (a) Schematic of the beam splitter design. The beam splitter has one input port and two output ports. The input electron enters a resonator with a weak phase grating in it. The electron is diffracted by the weak phase grating. After a certain number of round-trips in the resonator and passes through the grating, the electron leaves the resonator. The output ports 1 and 2 corresponds to the direct (blue) and diffracted (red) beams, respectively. The schematic leaves out details of the electron source, lenses, deflectors, and detectors. (b) Calculated beam intensities of the direct and diffracted beams as a function of number of passes through the weak phase grating made by a thin crystal. The crystal thickness is 1% of the extinction distance. The beam splitting ratio, i.e. the relative intensity between the two output beams, can be tuned by changing the number of passes through the crystal.

We analyze the beam splitter with a scattering matrix method. We first consider a thin crystal as the weak phase grating, and it is tilted in the two-beam condition so that only one diffracted beam is strongly excited (Figure 7.1(a)). We treat the direct and diffracted beams in free space as two plane waves: $e^{2\pi i \boldsymbol{k_0}\cdot\boldsymbol{r}}$ (the direct beam) and $e^{2\pi i \boldsymbol{k_g}\cdot\boldsymbol{r}}$ (the diffracted beam), where $\boldsymbol{k_0}$ and $\boldsymbol{k_g}$ are the corresponding momenta with the following relation

$$\boldsymbol{k_g} = \boldsymbol{k_0} + \boldsymbol{g} \tag{7.1}$$

Here $\boldsymbol{g}$ is the change of momentum introduced by the periodic crystal potential. Before entering the crystal, the electron wavefunction is a superposition of the two plane waves

$$\Psi_{\text{in}} = a_1 e^{2\pi i \boldsymbol{k_0}\cdot\boldsymbol{r}} + a_2 e^{2\pi i \boldsymbol{k_g}\cdot\boldsymbol{r}} \tag{7.2}$$

When the electron is in the crystal, the wavefunction is a superposition of two Bloch waves (in the two-beam condition) [179,180]

$$\Psi_{\text{crystal}} = c_1 B_1 + c_2 B_2 \tag{7.3}$$

$$B_1 = e^{2\pi i \boldsymbol{k_1}\cdot\boldsymbol{r}}\left(1 + e^{2\pi i \boldsymbol{g}\cdot\boldsymbol{r}}\right) \tag{7.4}$$

$$B_2 = e^{2\pi i \boldsymbol{k_2}\cdot\boldsymbol{r}}\left(1 - e^{2\pi i \boldsymbol{g}\cdot\boldsymbol{r}}\right) \tag{7.5}$$

After exiting the crystal, the electron wavefunction is again the superposition of two plane waves

$$\Psi_{\text{out}} = b_1 e^{2\pi i \boldsymbol{k_0}\cdot\boldsymbol{r}} + b_2 e^{2\pi i \boldsymbol{k_g}\cdot\boldsymbol{r}} \tag{7.6}$$

Therefore, the crystal can be mathematically modeled as a scattering matrix $\boldsymbol{S}$ that relates the plane wave amplitudes of the input and output beams

$$\begin{bmatrix} b_1 \\ b_2 \end{bmatrix} = \boldsymbol{S} \begin{bmatrix} a_1 \\ a_2 \end{bmatrix} \tag{7.7}$$

The scattering matrix can be determined by matching the boundary conditions at the entrance and exit of the crystal

$$\boldsymbol{S} = \begin{bmatrix} \cos(\pi t/\xi_g) & \mathrm{i}\cdot\sin(\pi t/\xi_g) \\ \mathrm{i}\cdot\sin(\pi t/\xi_g) & \cos(\pi t/\xi_g) \end{bmatrix} \tag{7.8}$$

Here, ξ_g is the crystal extinction distance for electron diffraction. It can be shown the scattering matrix is unitary, hence the total intensity of the electron beam is conserved as expected. The final input-output relation after multiple passes through the crystal is

$$\boldsymbol{\Psi}_{\mathrm{OUTPUT}} = \boldsymbol{S}^N \boldsymbol{\Psi}_{\mathrm{INPUT}} \tag{7.9}$$

Here, $\boldsymbol{\Psi}$ is the vector representation of the electron wavefunction where the first (second) element is the amplitude coefficient of plane wave $e^{2\pi i \boldsymbol{k_0} \cdot \boldsymbol{r}}$ ($e^{2\pi i \boldsymbol{k_g} \cdot \boldsymbol{r}}$).

The electron starts in the direct beam so that

$$\boldsymbol{\Psi}_{\mathrm{INPUT}} = \begin{bmatrix} 1 \\ 0 \end{bmatrix} \tag{7.10}$$

The final intensities of the direct and diffracted beams can be calculated

$$I_0 = |\boldsymbol{\Psi}_{\mathrm{OUTPUT}}(1)|^2 \tag{7.11}$$

$$I_g = |\boldsymbol{\Psi}_{\mathrm{OUTPUT}}(2)|^2 \tag{7.12}$$

Here, the index 1 and 2 is referring to the first and second element of the wavefunction vector, respectively. We calculated the beam intensities for a crystal, of which the thickness is 1% of the extinction distance, as the electron passes through the crystal multiple times (Figure 7.1(b)). After each pass, a small fraction of the beam intensity will be split into the diffracted beam, which eventually leads to the intensity transfer from the direct beam to the diffracted beam after a certain number of passes ($N = 50$ in Figure 7.1(b)). We call this number of passes for a complete intensity transfer “the switch point”. The switch point is determined by the phase modulation of the weak phase grating. A weaker phase modulation will lead to a larger switch point.

A desired beam splitting ratio between the two output beams can be achieved by opening the output port gates after the electron passes through the weak phase grating a certain number of times. This ratio is tunable from zero to unity, depending on the number of passes. It can be seen that this electron beam splitter design bears a resemblance to microwave and photonic directional couplers [181].

7.4 Case study: a nanofabricated grating

Electron beam splitters based on electron diffraction will inevitably produce multiple diffracted beams (Figure 7.2(a)). In the previous section, we limit our analysis in the two-beam condition without considering higher-order beams. In this section, we will study the case of using a nano-grating as the weak phase grating in our beam splitter design, and take high-order diffraction into consideration.

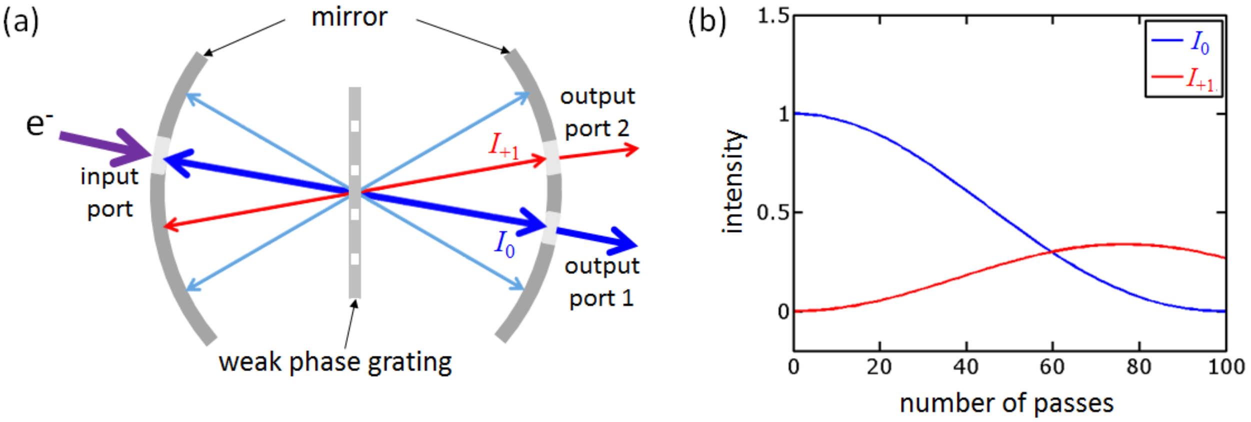

Figure 7.2. Electron beam splitters with multiple diffracted beams. (a) Schematic of the beam splitter similar to Figure 7.1(a), with the addition of high-order diffracted beams (light blue). These high-order diffracted beams do not contribute to the output beams. (b) Calculated beam intensities of the direct and 1st-order-diffracted beams as a function of number of passes through the weak phase grating made by a nano-grating. The nano-grating is a one-dimensional sinusoidal phase grating with 0.02π phase amplitude.

We use the scattering matrix method developed in the previous section to analyze the beam splitter. As high-order diffracted beams are considered, a matrix with dimension $M > 2$ is used.

In theory, there are infinitely many diffracted beams, while in practice, the very-high-order diffracted beams are weak and negligible. In our calculation, we choose $M = 100$ to get a reasonably accurate result.

We consider a one-dimensional sinusoidal phase grating is used as the weak phase grating. The grating modulation of the transmission for one period is

$$g_0(x) = exp\left[i\frac{A}{2}sin\left(2\pi\frac{x}{P}\right)\right], |x| \leq \frac{P}{2} \tag{7.13}$$

Here, A is the phase amplitude of the grating, and P is the grating pitch. The transmission modulation function of the full grating is

$$g(x) = g_0(x) * \sum_n \delta(x - nP) \tag{7.14}$$

This modulation function can be cast into a Fourier series

$$g(x) = \sum_{n=-\infty}^{\infty} J_n\left(\frac{A}{2}\right) exp\left(i\frac{2\pi n}{P}x\right) \tag{7.15}$$

The Fourier coefficients are Bessel functions of the 1st kind. As a result, the scattering matrix $\boldsymbol{S}$ of the weak sinusoidal phase grating is a $(2M + 1) \times (2M + 1)$ matrix (note there are positive orders, negative orders, and 0th order) with matrix elements

$$S_{ij} = J_{(j-i)}\left(\frac{A}{2}\right) \tag{7.16}$$

If $\boldsymbol{\Psi}_{\mathrm{INPUT}}$ and $\boldsymbol{\Psi}_{\mathrm{OUTPUT}}$ are $(2M + 1)$-dimensional vectors representing the input and output electron wavefunctions including high-order diffracted beams, we get the input-output relation after N passes

$$\boldsymbol{\Psi}_{\mathrm{OUTPUT}} = \boldsymbol{S}^N \boldsymbol{\Psi}_{\mathrm{INPUT}} \tag{7.17}$$

The intensity of one diffraction order is hence the squared magnitude of the corresponding element in the wavefunction vectors. We calculated the beam intensities for a beam splitter using a sinusoidal phase grating with a phase amplitude $A = 0.02\pi$ (Figure 7.2(b)). This phase amplitude can be obtained from a 1-nm-thick amorphous carbon film for 200 keV electrons. The two output beams are the direct (0-th-order) beam and the (+1)-st-order diffracted beam. An intensity transfer between the two beams are observed as the number of passes increases from zero to the switch point. However, in contrast to the two-beam condition in Figure 7.1(b), the sum of the intensities of the two output beams is always below unity. When the intensity of the direct beam drops to zero, the intensity of the (+1)-st-order diffracted beam does not increase to one; namely, a complete intensity transfer between the two output beams cannot be achieved. This intensity loss is due to the higher-order diffracted beams. As the electron is diffracted by the phase grating, there is always some finite intensity in the high-order diffracted beams. When used as a two-port beam splitter, this intensity loss means imperfect efficiency.

We use the quantum IFM concept to reduce the intensity loss associated with high-order diffracted beams and improve the beam splitter efficiency. The schematic is shown in Figure 7.3(a). A beam-limiting aperture is added to the design. The aperture allows the direct (0-th order) and (+1)-st-order diffracted beams to pass through, while blocking all other diffracted beams. Each time the electron passes through the weak phase grating, a fraction of the intensity will be diffracted into the higher-order beams. The aperture blocks these higher-order beams in every round trip and prevents intensity build-up in these beams.

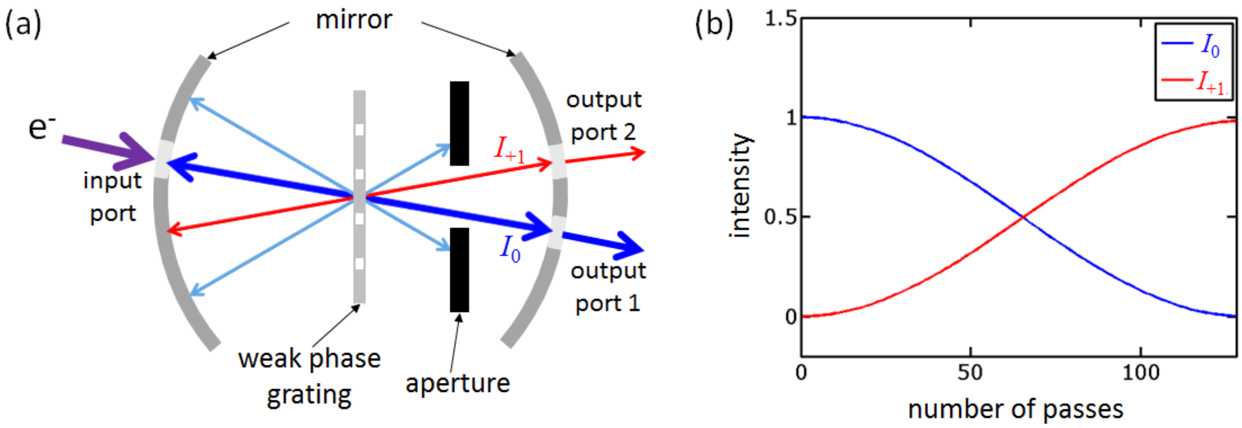

Figure 7.3. Beam splitter design using quantum IFM to suppress the high-order diffracted beams. (a) Schematic of the beam splitter similar to Figure 7.2(a), with the addition of a beam-limiting aperture (black) placed in the resonator. The aperture allows the direct (0-th order) and (+1)-st-order diffracted beams to pass through, while blocking other diffracted beams. (b) Calculated beam intensities of direct (0-th order) and (+1)-st-order diffracted beams as a function of number of passes through the weak phase grating. The grating is a one-dimensional sinusoidal phase grating with 0.02π phase amplitude.

In the scattering matrix method, the operation of the aperture can be represented by the matrix

$$\boldsymbol{S}_{\text{aper}} = \text{diag}(\cdots, 0, 1, 1, 0, \cdots) \tag{7.18}$$

This is a diagonal matrix with only two nonzero elements corresponding to the direct and (+1)-st-order diffracted beams that are not blocked by the aperture. The input-output relation for the electron passing through the weak phase grating and the aperture N times is

$$\boldsymbol{\Psi}_{\text{OUTPUT}} = (\boldsymbol{S}\boldsymbol{S}_{\text{aper}})^N \boldsymbol{\Psi}_{\text{INPUT}} \tag{7.19}$$

We calculated the beam intensities for a beam splitter using a sinusoidal phase grating with a phase amplitude $A = 0.02\pi$ (Figure 7.3(b)). In contrast to the beam splitter without the aperture, a complete intensity transfer can be achieved at the switch point, and the sum of the intensities of the two output beams is near unity (the sum approaches but never equals to unity; we will discuss this in a later section). The beam splitter performs similarly to the one in the two-beam condition (Figure 7.1), even though higher-order diffracted beams are considered. The aperture prevents intensity build-up in those higher-order diffracted beams, thus reducing intensity loss. With minimal intensity loss, a highly efficient, two-port electron beam splitter can be achieved.

7.5 Evaluation of intensity loss

It seems paradoxical that intensity loss due to high-order diffracted beams can be eliminated by blocking these beams. When these beams are blocked, their intensities would be lost and one would naively expect the total intensity loss to remain the same, if not increase. However, the combination of quantum IFM and quantum Zeno effect provides a counterintuitive way to eliminate the intensity loss caused by higher-order diffraction. In quantum IFM, an opaque object can be detected by a probe-particle without particle-object interaction, and the IFM efficiency can be improved via quantum Zeno effect by repeatedly interrogating the object with a small fraction of the particle wavefunction split from an asymmetric beam splitter. Our design of an efficient, two-port electron beam splitter is indeed performing a quantum IFM enhanced with quantum Zeno effect: the electron is the probe particle; the weak phase grating acts as the asymmetric beam splitter, the undesired higher-order diffraction is analogous to the small fraction of the wavefunction; the beam-limiting aperture is the opaque object; and the resonator effects the repeated interrogation via quantum Zeno effect. As quantum IFM minimizes particle-object interaction, our beam splitter design minimizes electron-aperture interaction and removes undesired diffraction modes with minimal intensity loss.

We want to mention that the intensity loss of the proposed beam splitter can be made arbitrarily close to zero, but not equal to zero. We calculated the beam intensity loss at the switch point for the beam splitter design with different switch points (Figure 7.4). It can be seen that there is always a finite intensity loss, and the intensity loss approaches zero with an increasing switch point. For a switch point higher than 230, the intensity loss can be made below 1%. The switch point increases with a decreasing phase modulation of the weak phase grating, and in theory, there is no upper limit for the switch point. Hence, the beam splitter can be designed with an arbitrarily low intensity loss. In practice, however, the switch point is limited by the implementation of the weak phase grating. For instance, if the weak phase grating is a nanofabricated grating, the minimum phase modulation is limited by the minimum achievable material thickness. For 200 keV electrons, a nano-grating made from graphene imposes the minimum phase modulation (among carbon-based materials) of ~0.007π. This phase modulation leads to a switch point of 871. Alternatively, if the weak phase grating is made from optical standing waves, a weak phase modulation can be made by using a low light intensity, and hence there is no limit to the switch point.

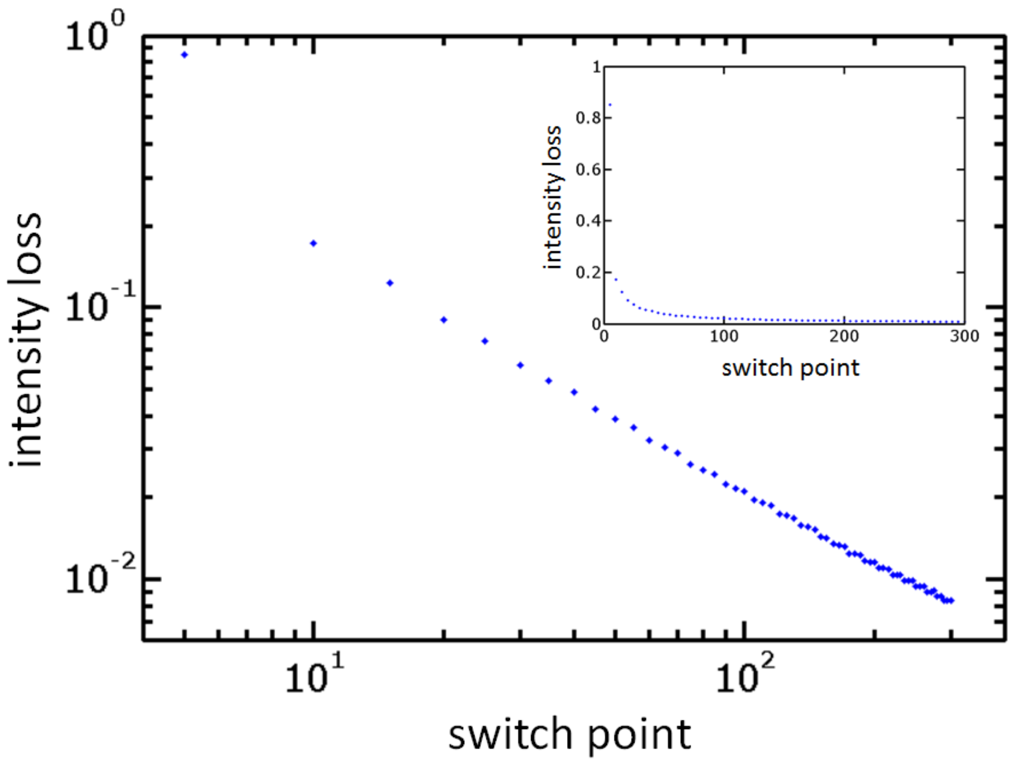

Figure 7.4. Intensity loss at the switch point for beam splitter designs with different switch points. The intensity loss approaches zero with an increasing switch point. Inset: the same plot in linear scale.

Besides undesired diffraction modes, intensity loss can also be caused by inelastic scattering if a material-based weak phase grating is used. Inelastic scattering is a non-unitary evolution of the system described by a non-Hermitian Hamiltonian. It has been shown non-Hermitian processes cannot be suppressed by a combination of quantum IFM and quantum Zeno effect [182,183]. To treat inelastic scattering, we consider a nano-grating is used, and the grating imposes both phase modulation and amplitude modulation onto the electron beam. The amplitude modulation is essentially attenuation caused by inelastic scattering, and can be modeled by the transmission probability

$$\mathrm{T} = e^{-t/\lambda} \tag{7.20}$$

Here, t is the material thickness, and λ is the inelastic mean free path (MFP) of the material. We incorporated this transmission probability into the scattering matrix method, and calculated the beam intensities for a beam splitter using a weak sinusoidal phase grating with 0.02π phase amplitude. For 200 keV electrons, we chose 1-nm-thick amorphous carbon film as the grating material. The inelastic MFP of amorphous carbon for 200 keV electrons is 160 nm [184]. Figure 7.5(a) shows the calculated beam intensities for the 0-th order and (+1)-st order beams. Inelastic scattering leads to a non-ideal efficiency. At the switch point, the efficiency is ~55%.

The effect of inelastic scattering depends on the nano-grating materials. For comparison with the amorphous carbon film, we also consider a nano-grating made from 1-nm-thick gold foil. For 200 keV electrons, the phase amplitude is 0.058π, and the inelastic MFP is 84 nm. Figure 7.5(b) shows the calculated beam intensities for the 0-th order and (+1)-st order beams. At the switch point, the efficiency is ~63%. For nano-gratings, the phase amplitude is related to the material mean inner potential (MIP). To achieve a certain beam splitting ratio, the material needs to impose a certain phase shift $\Delta\phi_0$ to the electron beam, which requires a certain material thickness t_0 according to

$$\Delta\phi_0 = \mathrm{C}_0 V_{\mathrm{MIP}} t_0 \tag{7.21}$$

Here, V_{MIP} is the material MIP, and C_0 is a constant. The beam splitter efficiency can be calculated as the intensity transmission probability

$$\mathrm{T}_0 = e^{-t_0/\lambda} = e^{-\frac{\Delta\phi_0}{\mathrm{C}_0 V_{\mathrm{MIP}}\lambda}} \tag{7.22}$$

It can be seen that materials with a large MIP-MFP product ($V_{\mathrm{MIP}}\lambda$) are preferred for a high efficiency beam splitter. Figure 7.5(c) shows the reported MIP and MFP values for several materials [184–189]. The three red dashed lines indicate three contours of constant MIP-MFP value.

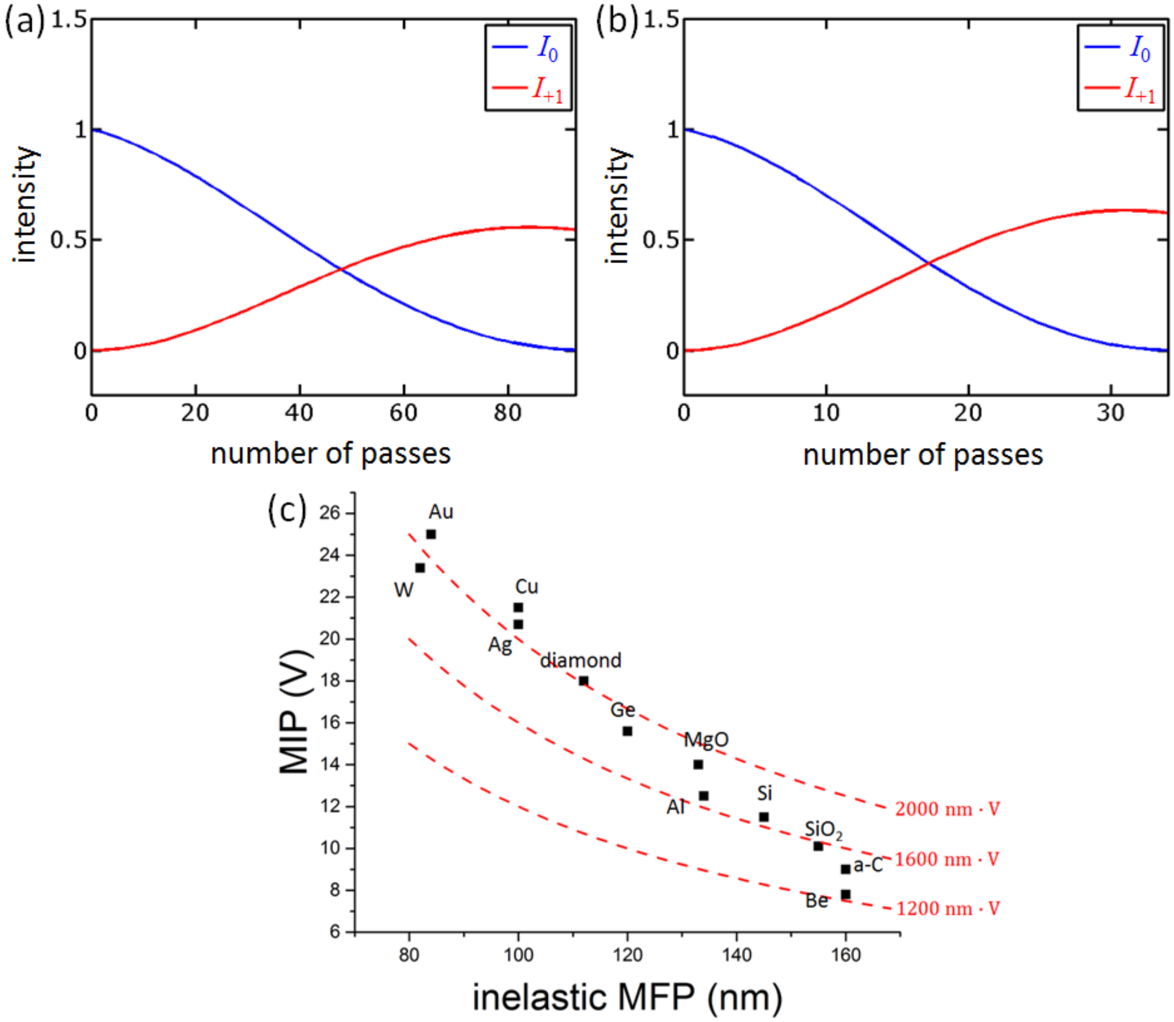

Figure 7.5. The effect of inelastic scattering. (a) Calculated beam intensities of the direct and diffracted beams as a function of number of passes through a weak sinusoidal phase grating made from a 1-nm-thick amorphous carbon film. The phase amplitude of the grating is 0.02π for 200 keV electrons. At the switch point, the efficiency is ~55%. (b) Calculated beam intensities of the direct and diffracted beams as a function of number of passes through a weak sinusoidal phase grating made from a 1-nm-thick gold foil. The phase amplitude of the grating is 0.058π for 200 keV electrons. At the switch point, the efficiency is ~63%. (c) MIP and MFP data for several materials [184–189]. Red dashed lines are contours with constant MIP-MFP products.

7.6 Summary

In this chapter, we propose the design of a highly efficient, two-port electron beam splitter based on quantum IFM and quantum Zeno effect. The beam splitter consists of a resonator and a weak phase grating. The input electron enters the resonator and is diffracted multiple times by the grating. The electron exits via the two output ports after some number of round trips to achieved the targeted beam splitting ratio. The beam splitter operates like a directional coupler for electron beams. The higher-order diffracted beams are suppressed by a beam-limiting aperture in the resonator, and quantum IFM ensures the intensity loss caused by blocking the high-order diffraction is minimized.

In practice, most of the components (electron sources, mirrors, phase gratings, apertures, and detectors) required to build such a beam splitter have been developed. In the meantime, a timed gate that allows the electron to enter and exit the resonator is under active development [168]. Hence, the experimental implementation of the proposed beam splitter is feasible.

The efficient, two-port electron beam splitter can benefit various electron beam technologies, especially the emerging techniques that bear a resemblance to quantum optics experiments [168,175]. Additionally, the beam splitter can be used to improve the efficiency of electron beam shaping and wavefront engineering based on diffractive holograms [147–150,155]. Finally, we want to mention this design can be applied to beam splitters for not only electrons, but also photons, neutrons, atoms, and other quantum mechanical systems.

Chapter 8

Conclusion and Outlook

We have developed several nanoscale structures and devices for vacuum optoelectronic engineering, including ultrafast photoelectron emission from nanostructures, free-electron-driven plasmon and photon emission from nanostructures, and manipulation of free electrons with nanostructures.

In Chapter 2, we demonstrated Au nanorod arrays as high-yield, ultrafast optical field emitters. The optical near-field and charge yield were enhanced by surface plasmon resonance. We designed, fabricated, and spectroscopically characterized the nanorod arrays to match the plasmonic resonance with the driving laser wavelength. We also investigated the effect of the dielectric environment, including the substrate and the metal adhesion layer, on the plasmonic resonance and photoemission yield. The high-yield ultrafast optical field emitter arrays could find applications in the development of efficient and bright free-electron lasers (FELs), as well as time-resolved electron microscopy and spectroscopy experiments.

The ultrafast nature of optical-field-driven photoemission provides a route to resolving the optical field that is oscillating at petahertz (PHz) frequency. In Chapter 3, we demonstrated the detection of carrier-envelope phase (CEP) using electrically connected plasmonic nanoantenna arrays. We designed and fabricated connected bow-tie nanoantenna arrays. We used electromigration to selectively remove short-circuit caused by fabrication process variations. We detected the CEP of ultrafast optical pulses by measuring the photocurrent from the nanoantenna array. Our work demonstrated on-chip integration of multiple optical-field-driven optoelectronic devices with distributed electrical interconnection, and represented a step towards integrated ultrafast PHz electronic and optoelectronic devices.

Electron beams can induce surface plasmon emission in plasmonic nanostructures, and this phenomenon has been used for nanoscale characterization of plasmonic modes in a scanning transmission electron microscope (STEM) using electron-energy-loss spectroscopy (EELS). In Chapter 4, we demonstrated the study of aluminum nanodisk plasmonic modes using STEM-EELS. We fabricated lithographically defined aluminum nanodisks on a supporting silicon nitride membrane. We showed the excitation of multipolar edge modes and breathing modes, and theoretically reproduced their dispersion relations. These modes were tunable in the ultraviolet (UV) region by changing the nanodisk size. We also discovered that, when the nanodisk size was small and comparable to its thickness, the assumption of flat nanostructures was no longer valid, and the surface plasmon modes possessed a polar dependence. Our work developed nanostructures supporting surface plasmons in a wide spectral range from 2 eV to 8 eV and enabling potential UV applications. Our theoretical analysis also deepened the understanding of the nanodisk plasmonic modes.

Similar to plasmon emission, electron beams can also induce photon emission when interacting with nanostructures. In Chapter 5, we demonstrated light emission in the form of Smith-Purcell radiation from free-electron-driven nanophotonic metasurfaces. The polarization of the emitted light were tuned by the metasurface design, in stark contrast to the conventional grating-based Smith-Purcell radiation, of which the polarization was predetermined by the electron-beam direction. Our work took a step towards compact and tunable free-electron-driven light sources with potential applications in nanophotonics research, on-chip integrated light sources, charged particle detectors and beam diagnostics, biomedical imaging and diagnostics.

Nanostructured material phase plates can impose designed phase modulations onto electron beams. In Chapter 6, we demonstrated large-area mesh-shaped electron phase plates in a thin silicon nitride membrane. We fabricated the phase plates with electron beam lithography and reactive-ion-etching. The phase plates were characterized by electron diffraction in a transmission electron microscope (TEM) with various electron energies, as well as diffractive imaging in a scanning electron microscope (SEM). Our work provided an alternative route towards the creation of electron phase plates with adjustable functions, such as tunable diffraction efficiency, by changing the electron energy.

Diffractive electron phase plates can be used as electron beam splitters; however, these beam splitters are inefficient two-port splitters due to the presence of high-order diffracted beams. In Chapter 7, we theoretically proposed a design for efficient, two-port electron beam splitters. This design combined an electron phase grating and an electron resonator. High-order diffraction from the grating was removed by a beam-limiting aperture, while the beam intensity loss was kept close to zero by invoking quantum interaction-free measurement and quantum Zeno effect. Our beam splitter design could benefit various electron beam technologies, especially the emerging techniques that bear a resemblance to quantum optics experiments and require a two-port electron beam splitter.

In line with the topics discussed in this thesis, there comes some other interesting scientific questions and further technological development. These potential future works are based on the extension of one topic, or the combination of several topics, in this thesis.

The ultrafast photoelectron-emission devices could benefit from new materials and device architectures. We observed device degradation in photoemission measurement, which was induced by laser-reshaping of the plasmonic gold nanostructures. By switching to alternative refractory plasmonic materials such as tungsten, tantalum, and transition metal nitrides, the damage threshold of the optical field emitters could be increased [61]. Additionally, the nano-gap dimension of our plasmonic bow-tie nanoantennas was sensitive to fabrication process variations, and the smallest achievable gap size was limited by lithographic resolution. By switching from in-plane nano-gaps defined by lithography to vertical nano-gaps defined by material thickness, we could achieve extremely thin and uniform nano-gaps by using self-assembled monolayers, atomic-layer-deposited dielectrics, and two-dimensional materials [190]. Furthermore, our on-chip connected nanoantenna arrays performed CEP detection with the current interconnect configuration. By designing other interconnect configurations, we could achieve multiplexed functions and demonstrate more complex integrated circuits of PHz optoelectronic devices.

The free-electron-driven plasmon and photon emission devices could benefit from engineering the nanostructures as well as the electron beams. Besides polarization control, properly designed metasurfaces could enable the control of other properties of free-electron radiation, such as phase, wave vector, spatial distribution, and orbital angular momentum. Additionally, by integrating nanoscale gratings and metasurfaces with on-chip electron emitters, an all-on-chip free-electron light source could be demonstrated. This electrically-driven on-chip light source could be fully tunable in terms of both spectral content and intensity, while other properties of the emitted light could be controlled by designed metasurfaces. Moreover, Smith-Purcell radiation has been demonstrated in the superradiant regime, where collective effects in the electron beam can structure the beam into electron bunches that radiate in-phase to produce high-power, coherent electromagnetic radiation [120,191,192]. By optimizing the nanostructure design and using a high beam current or a pre-bunched beam, FEL-like superradiant Smith-Purcell radiation in the optical frequency could potentially be demonstrated. Furthermore, it would be interesting to investigate free-electron radiation from tailored electron wavefunctions, which could be achieved with electron phase plates. This investigation could shed light upon the mechanism of the interaction between free electrons and nanophotonic structures, and provide additional degrees of freedom to tune the free-electron light emission. Tailored electron wavefunction could also enable the study of the temporal and quantum statistical properties of the emitted light.

Bibliography

[1] J. W. Gewartowski and H. A. Watson, *Principles of Electron Tubes: Including Grid-Controlled Tubes, Microwave Tubes, and Gas Tubes* (Van Nostrand, 1965).

[2] D. R. HARTREE, Nature **158**, 500 (1946).

[3] H. Iams and B. Salzberg, Proc. IRE **23**, 55 (1935).

[4] F. Braun, Ann. Der Phys. Und Chemie **296**, 552 (1897).

[5] A. S. Gilmour, *Klystrons, Traveling Wave Tubes, Magnetrons, Crossed-Field Amplifiers, and Gyrotrons* (Artech House, 2011).

[6] C. Körner, Int. Mater. Rev. **61**, 361 (2016).

[7] H. E. Cline and T. R. Anthony, J. Appl. Phys. **48**, 3895 (1977).

[8] C. Vieu, F. Carcenac, A. Pépin, Y. Chen, M. Mejias, A. Lebib, L. Manin-Ferlazzo, L. Couraud, and H. Launois, Appl. Surf. Sci. **164**, 111 (2000).

[9] E. Ruska, Rev. Mod. Phys. **59**, 627 (1987).

[10] K. Wille, *The Physics of Particle Accelerators: An Introduction* (Clarendon Press, 2000).

[11] R. G. Hobbs, Y. Yang, A. Fallahi, P. D. Keathley, E. De Leo, F. X. Kärtner, W. S. Graves, and K. K. Berggren, ACS Nano **8**, 11474 (2014).

[12] J. C. Williamson, J. Cao, H. Ihee, H. Frey, and A. H. Zewail, Nature **386**, 159 (1997).

[13] W. E. King, G. H. Campbell, A. Frank, B. Reed, J. F. Schmerge, B. J. Siwick, B. C. Stuart, and P. M. Weber, J. Appl. Phys. **97**, 111101 (2005).

[14] A. H. Zewail, Annu. Rev. Phys. Chem. **57**, 65 (2006).

[15] P. Baum and A. H. Zewail, Proc. Natl. Acad. Sci. **103**, 16105 (2006).

[16] W. Ackermann, G. Asova, V. Ayvazyan, A. Azima, N. Baboi, J. Bähr, V. Balandin, B. Beutner, A. Brandt, A. Bolzmann, R. Brinkmann, O. I. Brovko, M. Castellano, P. Castro, L. Catani, E. Chiadroni, S. Choroba, A. Cianchi, J. T. Costello, D. Cubaynes, J. Dardis, W. Decking, H. Delsim-Hashemi, A. Delserieys, G. Di Pirro, M. Dohlus, S. Düsterer, A. Eckhardt, H. T. Edwards, B. Faatz, J. Feldhaus, K. Flöttmann, J. Frisch, L. Fröhlich, T. Garvey, U. Gensch, C. Gerth, M. Görler, N. Golubeva, H.-J. Grabosch, M. Grecki, O. Grimm, K. Hacker, U. Hahn, J. H. Han, K. Honkavaara, T. Hott, M. Hüning, Y. Ivanisenko, E. Jaeschke, W. Jalmuzna, T. Jezynski, R. Kammering, V. Katalev, K. Kavanagh, E. T. Kennedy, S. Khodyachykh, K. Klose, V. Kocharyan, M. Körfer, M. Kollewe, W. Koprek, S. Korepanov, D. Kostin, M. Krassilnikov, G. Kube, M. Kuhlmann, C. L. S. Lewis, L. Lilje, T. Limberg, D. Lipka, F. Löhl, H. Luna, M. Luong, M. Martins, M. Meyer, P. Michelato, V. Miltchev, W. D. Möller, L. Monaco, W. F. O. Müller, O. Napieralski, O. Napoly, P. Nicolosi, D. Nölle, T. Nuñez, A. Oppelt, C. Pagani, R. Paparella, N. Pchalek, J. Pedregosa-Gutierrez, B. Petersen, B. Petrosyan, G. Petrosyan, L.

Petrosyan, J. Pflüger, E. Plönjes, L. Poletto, K. Pozniak, E. Prat, D. Proch, P. Pucyk, P. Radcliffe, H. Redlin, K. Rehlich, M. Richter, M. Roehrs, J. Roensch, R. Romaniuk, M. Ross, J. Rossbach, V. Rybnikov, M. Sachwitz, E. L. Saldin, W. Sandner, H. Schlarb, B. Schmidt, M. Schmitz, P. Schmüser, J. R. Schneider, E. A. Schneidmiller, S. Schnepp, S. Schreiber, M. Seidel, D. Sertore, A. V. Shabunov, C. Simon, S. Simrock, E. Sombrowski, A. A. Sorokin, P. Spanknebel, R. Spesyvtsev, L. Staykov, B. Steffen, F. Stephan, F. Stulle, H. Thom, K. Tiedtke, M. Tischer, S. Toleikis, R. Treusch, D. Trines, I. Tsakov, E. Vogel, T. Weiland, H. Weise, M. Wellhöfer, M. Wendt, I. Will, A. Winter, K. Wittenburg, W. Wurth, P. Yeates, M. V. Yurkov, I. Zagorodnov, and K. Zapfe, Nat. Photonics **1**, 336 (2007).

[17] P. Emma, R. Akre, J. Arthur, R. Bionta, C. Bostedt, J. Bozek, A. Brachmann, P. Bucksbaum, R. Coffee, F.-J. Decker, Y. Ding, D. Dowell, S. Edstrom, A. Fisher, J. Frisch, S. Gilevich, J. Hastings, G. Hays, P. Hering, Z. Huang, R. Iverson, H. Loos, M. Messerschmidt, A. Miahnahri, S. Moeller, H.-D. Nuhn, G. Pile, D. Ratner, J. Rzepiela, D. Schultz, T. Smith, P. Stefan, H. Tompkins, J. Turner, J. Welch, W. White, J. Wu, G. Yocky, and J. Galayda, Nat. Photonics **4**, 641 (2010).

[18] W. S. Graves, F. X. Kärtner, D. E. Moncton, and P. Piot, Phys. Rev. Lett. **108**, 263904 (2012).

[19] S. Nie and S. R. Emory, Science (80-.). **275**, 1102 (1997).

[20] K. A. Willets and R. P. Van Duyne, Annu. Rev. Phys. Chem. **58**, 267 (2007).

[21] K. Imura, T. Nagahara, and H. Okamoto, J. Chem. Phys. **122**, 154701 (2005).

[22] J. B. Pendry, Phys. Rev. Lett. **85**, 3966 (2000).

[23] H. J. Lezec, J. A. Dionne, and H. A. Atwater, Science (80-.). **316**, 430 (2007).

[24] Y. Zhao, M. A. Belkin, and A. Alù, Nat. Commun. **3**, 870 (2012).

[25] J. N. Anker, W. P. Hall, O. Lyandres, N. C. Shah, J. Zhao, and R. P. Van Duyne, Nat. Mater. **7**, 442 (2008).

[26] D. Rodrigo, O. Limaj, D. Janner, D. Etezadi, F. J. García De Abajo, V. Pruneri, H. Altug, F. J. Garcia de Abajo, V. Pruneri, and H. Altug, Science (80-.). **349**, 165 (2015).

[27] G. Volpe, M. Noack, S. S. Aćimović, C. Reinhardt, and R. Quidant, Nano Lett. **12**, 4864 (2012).

[28] P. Dombi, A. Hörl, P. Rácz, I. Márton, A. Trügler, J. R. Krenn, and U. Hohenester, Nano Lett. **13**, 674 (2013).

[29] P. M. Nagel, J. S. Robinson, B. D. Harteneck, T. Pfeifer, M. J. Abel, J. S. Prell, D. M. Neumark, R. A. Kaindl, and S. R. Leone, Chem. Phys. **414**, 106 (2013).

[30] R. K. Li, H. To, G. Andonian, J. Feng, A. Polyakov, C. M. Scoby, K. Thompson, W. Wan, H. a. Padmore, and P. Musumeci, Phys. Rev. Lett. **110**, 074801 (2013).

[31] A. Polyakov, C. Senft, K. F. Thompson, J. Feng, S. Cabrini, P. J. Schuck, H. A. Padmore, S. J. Peppernick, and W. P. Hess, Phys. Rev. Lett. **110**, 076802 (2013).

[32] P. B. Johnson and R. W. Christy, Phys. Rev. B **6**, 4370 (1972).

[33] K.-S. Lee and M. A. El-Sayed, J. Phys. Chem. B **109**, 20331 (2005).

[34] R. Bormann, M. Gulde, A. Weismann, S. V. Yalunin, and C. Ropers, Phys. Rev. Lett. **105**, 147601 (2010).

[35] S. V. Yalunin, M. Gulde, and C. Ropers, Phys. Rev. B **84**, 195426 (2011).

[36] M. F. Ciappina, J. A. Pérez-Hernández, A. S. Landsman, W. A. Okell, S. Zherebtsov, B. Förg, J. Schötz, L. Seiffert, T. Fennel, T. Shaaran, T. Zimmermann, A. Chacón, R. Guichard, A. Zaïr, J. W. G. Tisch, J. P. Marangos, T. Witting, A. Braun, S. A. Maier, L. Roso, M. Krüger, P. Hommelhoff, M. F. Kling, F. Krausz, and M. Lewenstein, Reports Prog. Phys. **80**, 054401 (2017).

[37] T. Srinivasan-Rao, J. Fischer, and T. Tsang, J. Appl. Phys. **69**, 3291 (1991).

[38] F. Krausz and M. I. Stockman, Nat. Photonics **8**, 205 (2014).

[39] B. Bergues, M. Kübel, N. G. Johnson, B. Fischer, N. Camus, K. J. Betsch, O. Herrwerth, A. Senftleben, A. M. Sayler, T. Rathje, T. Pfeifer, I. Ben-Itzhak, R. R. Jones, G. G. Paulus, F. Krausz, R. Moshammer, J. Ullrich, and M. F. Kling, Nat. Commun. **3**, 813 (2012).

[40] M. F. Kling, C. Siedschlag, A. J. Verhoef, J. I. Khan, M. Schultze, T. Uphues, Y. Ni, M. Uiberacker, M. Drescher, F. Krausz, and M. J. J. Vrakking, Science (80-.). **312**, 246 (2006).

[41] A. De Bohan, P. Antoine, D. B. Milošević, and B. Piraux, Phys. Rev. Lett. **81**, 1837 (1998).

[42] M. Ivanov, P. B. Corkum, T. Zuo, and A. Bandrauk, Phys. Rev. Lett. **74**, 2933 (1995).

[43] I. P. Christov, M. M. Murnane, and H. C. Kapteyn, Phys. Rev. Lett. **78**, 1251 (1997).

[44] J. Ye, L.-S. Ma, T. Day, and J. L. Hall, Opt. Lett. **22**, 746 (1997).

[45] D. J. Jones, S. A. Diddams, J. K. Ranka, A. Stentz, R. S. Windeler, J. L. Hall, and S. T. Cundiff, in *Science (80-.).* (IEEE, 2000), pp. 635–639.

[46] T. Udem, J. Reichert, R. Holzwarth, and T. W. Hänsch, Phys. Rev. Lett. **82**, 3568 (1999).

[47] C. Reimer, M. Kues, P. Roztocki, B. Wetzel, F. Grazioso, B. E. Little, S. T. Chu, T. Johnston, Y. Bromberg, L. Caspani, D. J. Moss, and R. Morandotti, Science (80-.). **351**, 1176 (2016).

[48] H. R. R. Telle, G. Steinmeyer, A. E. E. Dunlop, J. Stenger, D. H. H. Sutter, and U. Keller, Appl. Phys. B Lasers Opt. **69**, 327 (1999).

[49] L. Xu, C. Spielmann, A. Poppe, T. Brabec, F. Krausz, and T. W. Hänsch, Opt. Lett. **21**, 2008 (1996).

[50] T. Wittmann, B. Horvath, W. Helml, M. G. Schätzel, X. Gu, A. L. Cavalieri, G. G. Paulus, and R. Kienberger, Nat. Phys. **5**, 357 (2009).

[51] G. G. Paulus, F. Grasbon, H. Walther, P. Villoresi, M. Nisoli, S. Stagira, E. Priori, and S. De Silvestri, Nature **414**, 182 (2001).

[52] G. G. Paulus, F. Lindner, H. Walther, A. Baltuška, E. Goulielmakis, M. Lezius, and F. Krausz, Phys. Rev. Lett. **91**, 253004 (2003).

[53] T. Paasch-Colberg, A. Schiffrin, N. Karpowicz, S. Kruchinin, Ö. Sağlam, S. Keiber, O. Razskazovskaya, S. Mühlbrandt, A. Alnaser, M. Kübel, V. Apalkov, D. Gerster, J. Reichert, T. Wittmann, J. V Barth, M. I. Stockman, R. Ernstorfer, V. S. Yakovlev, R. Kienberger, and F. Krausz, Nat. Photonics **8**, 214 (2014).

[54] T. Rybka, M. Ludwig, M. F. Schmalz, V. Knittel, D. Brida, and A. Leitenstorfer, Nat. Photonics **10**, 667 (2016).

[55] W. P. Putnam, R. G. Hobbs, P. D. Keathley, K. K. Berggren, F. X. Kärtner, F. X. Kartner, and F. X. Kärtner, Nat. Phys. **13**, 335 (2017).

[56] S. H. Chew, A. Gliserin, J. Schmidt, and U. Kleineberg, Phys. Rev. Appl. **11**, 054080 (2019).

[57] H. Park, A. K. L. Lim, A. P. Alivisatos, J. Park, and P. L. McEuen, Appl. Phys. Lett. **75**, 301 (1999).

[58] S. Karim, K. Maaz, G. Ali, and W. Ensinger, J. Phys. D. Appl. Phys. **42**, 185403 (2009).

[59] J. C. Prangsma, J. Kern, A. G. Knapp, S. Grossmann, M. Emmerling, M. Kamp, and B. Hecht, Nano Lett. **12**, 3915 (2012).

[60] J. Kern, R. Kullock, J. Prangsma, M. Emmerling, M. Kamp, and B. Hecht, Nat. Photonics **9**, 582 (2015).

[61] U. Guler, A. Boltasseva, and V. M. Shalaev, Science (80-.). **344**, 263 (2014).

[62] R. G. Hobbs, V. R. Manfrinato, Y. Yang, S. A. Goodman, L. Zhang, E. A. Stach, and K. K. Berggren, Nano Lett. **16**, 4149 (2016).

[63] S. A. Maier, *Plasmonics: Fundamentals and Applications* (Springer US, New York, NY, 2007).

[64] H. Duan, H. Hu, K. Kumar, Z. Shen, and J. K. W. Yang, ACS Nano **5**, 7593 (2011).

[65] J. Ye, F. Wen, H. Sobhani, J. B. Lassiter, P. Van Dorpe, P. Nordlander, N. J. Halas, P. Van Dorpe, P. Nordlander, and N. J. Halas, Nano Lett. **12**, 1660 (2012).

[66] A. V. Kabashin, P. Evans, S. Pastkovsky, W. Hendren, G. A. Wurtz, R. Atkinson, R. Pollard, V. A. Podolskiy, and A. V. Zayats, Nat. Mater. **8**, 867 (2009).

[67] S. Ostovar pour, L. Rocks, K. Faulds, D. Graham, V. Parchaňský, P. Bouř, and E. W. Blanch, Nat. Chem. **7**, 591 (2015).

[68] P. Zijlstra, P. M. R. R. Paulo, and M. Orrit, Nat. Nanotechnol. **7**, 379 (2012).

[69] X. Hu, E. A. Dauler, R. J. Molnar, and K. K. Berggren, Opt. Express **19**, 17 (2011).

[70] M. W. Knight, H. Sobhani, P. Nordlander, and N. J. Halas, Science (80-.). **332**, 702 (2011).

[71] H. A. Atwater and A. Polman, Nat. Mater. **9**, 205 (2010).

[72] S. Linic, P. Christopher, and D. B. Ingram, Nat. Mater. **10**, 911 (2011).

[73] T. F. Villesen, C. Uhrenfeldt, B. Johansen, and A. Nylandsted Larsen, Nanotechnology **24**, 275606 (2013).

[74] A. Ono, M. Kikawada, R. Akimoto, W. Inami, and Y. Kawata, Opt. Express **21**, 17447 (2013).

[75] G. Maidecchi, G. Gonella, R. Proietti Zaccaria, R. Moroni, L. Anghinolfi, A. Giglia, S. Nannarone, L. Mattera, H. L. Dai, M. Canepa, and F. Bisio, ACS Nano (2013).

[76] S. K. Jha, Z. Ahmed, M. Agio, Y. Ekinci, and J. F. Löffler, J. Am. Chem. Soc. **134**, 1966 (2012).

[77] C. Langhammer, M. Schwind, B. Kasemo, and I. Zorić, Nano Lett. **8**, 1461 (2008).

[78] M. W. Knight, N. S. King, L. Liu, H. O. Everitt, P. Nordlander, and N. J. Halas, ACS Nano **8**, 834 (2014).

[79] L. Zhou, C. Zhang, M. J. McClain, A. Manjavacas, C. M. Krauter, S. Tian, F. Berg, H. O. Everitt, E. A. Carter, P. Nordlander, and N. J. Halas, Nano Lett. **16**, 1478 (2016).

[80] J. Nelayah, M. Kociak, O. Stéphan, F. J. García de Abajo, M. Tencé, L. Henrard, D. Taverna, I. Pastoriza-Santos, L. M. Liz-Marzán, C. Colliex, F. J. G. De Abajo, M. Tencé, L. Henrard, D. Taverna, I. Pastoriza-Santos, L. M. Liz-Marzán, C. Colliex, F. J. García de Abajo, M. Tencé, L. Henrard, D. Taverna, I. Pastoriza-Santos, L. M. Liz-Marzán, and C. Colliex, Nat. Phys. **3**, 348 (2007).

[81] F. J. García De Abajo and M. Kociak, Phys. Rev. Lett. **100**, 1 (2008).

[82] F.-P. Schmidt, H. Ditlbacher, U. Hohenester, A. Hohenau, F. Hofer, and J. R. Krenn, Nano Lett. **12**, 5780 (2012).

[83] F. P. Schmidt, H. Ditlbacher, U. Hohenester, A. Hohenau, F. Hofer, and J. R. Krenn, Nat. Commun. **5**, 1 (2014).

[84] F. P. Schmidt, H. Ditlbacher, F. Hofer, J. R. Krenn, and U. Hohenester, Nano Lett. **14**, 4810 (2014).

[85] O. Nicoletti, F. de la Peña, R. K. Leary, D. J. Holland, C. Ducati, and P. A. Midgley, Nature **502**, 80 (2013).

[86] F. J. García De Abajo, Rev. Mod. Phys. **82**, 209 (2010).

[87] D. T. Schoen, A. C. Atre, A. García-Etxarri, J. a. Dionne, and M. L. Brongersma, Nano Lett. **15**, 120 (2015).

[88] H. Duan, A. I. Fernández-Domínguez, M. Bosman, S. a Maier, and J. K. W. Yang, Nano Lett. **12**, 1683 (2012).

[89] A. L. ; B. Koh, K. Bao, I. Khan, W. E. Smith, G. Kothleitner, P. Nordlander, S. A. Maier, D. W. McComb, K. ; Khan, I. E. Smith, W. E. ; Kothleitner, G. P. Nordlander, P. A. Maier, S. A. ; McComb, and D. W., ACS Nano **3**, 3015 (2009).

[90] E. P. Bellido, A. Manjavacas, Y. Zhang, Y. Cao, P. Nordlander, and G. A. Botton, ACS Photonics **3**, 428 (2016).

[91] E. P. Bellido, Y. Zhang, A. Manjavacas, P. Nordlander, and G. A. Botton, ACS Photonics **4**, 1558 (2017).

[92] A. Campos, A. Arbouet, J. Martin, D. Gérard, J. Proust, J. Plain, and M. Kociak, ACS Photonics **4**, 1257 (2017).

[93] S. Raza, S. Kadkhodazadeh, T. Christensen, M. Di Vece, M. Wubs, N. A. Mortensen, and N. Stenger, Nat. Commun. **6**, 8788 (2015).

[94] A. Wiener, H. Duan, M. Bosman, A. P. Horsfield, J. B. Pendry, J. K. W. Yang, S. A. Maier, and A. I. Fernández-Domínguez, ACS Nano **7**, 6287 (2013).

[95] A. D. Rakic, A. B. Djurišic, J. M. Elazar, and M. L. Majewski, Appl. Opt. **37**, 5271 (1998).

[96] F. P. Schmidt, A. Losquin, F. Hofer, A. Hohenau, J. R. Krenn, and M. Kociak, ACS Photonics **5**, 861 (2018).

[97] L. Novotny, Phys. Rev. Lett. **98**, 266802 (2007).

[98] M. a. Kats, R. Blanchard, P. Genevet, and F. Capasso, Nat. Mater. **12**, 20 (2013).

[99] J. A. Scholl, A. L. Koh, and J. A. Dionne, Nature **483**, 421 (2012).

[100] V. Kulkarni, E. Prodan, and P. Nordlander, Nano Lett. **13**, 5873 (2013).

[101] R. Esteban, A. G. Borisov, P. Nordlander, and J. Aizpurua, Nat. Commun. **3**, 825 (2012).

[102] C. Ciraci, R. T. Hill, J. J. Mock, Y. Urzhumov, a. I. Fernandez-Dominguez, S. a. Maier, J. B. Pendry, a. Chilkoti, D. R. Smith, C. Ciracì, R. T. Hill, J. J. Mock, Y. Urzhumov, a I. Fernández-Domínguez, S. a. Maier, J. B. Pendry, a. Chilkoti, D. R. Smith, C. Ciraci, R. T. Hill, J. J. Mock, Y. Urzhumov, a. I. Fernandez-Dominguez, S. a. Maier, J. B. Pendry, a. Chilkoti, and D. R. Smith, Science (80-.). **337**, 1072 (2012).

[103] Y. Yang, D. Zhu, W. Yan, A. Agarwal, M. Zheng, J. D. Joannopoulos, P. Lalanne, T. Christensen, K. K. Berggren, and M. Soljačić, (2019).

[104] S. F. Tan, L. Wu, J. K. W. Yang, P. Bai, M. Bosman, and C. A. Nijhuis, Science (80-.). **343**, 1496 (2014).

[105] K. J. Savage, M. M. Hawkeye, R. Esteban, A. G. Borisov, J. Aizpurua, and J. J. Baumberg, Nature **491**, 574 (2012).

[106] J. a Scholl, A. García-Etxarri, A. L. Koh, and J. a Dionne, Nano Lett. **13**, 564 (2013).

[107] J. R. Pierce, Bell Syst. Tech. J. **29**, 390 (1950).

[108] H. Motz, J. Appl. Phys. **22**, 527 (1951).

[109] P. D. Coleman and C. Enderby, J. Appl. Phys. **31**, 1695 (1960).

[110] R. Ulrich, Zeitschrift Für Phys. **199**, 171 (1967).

[111] F. S. Rusin and G. D. Bogomolov, Proc. IEEE **57**, 720 (1969).

[112] L. R. Elias, W. M. Fairbank, J. M. J. Madey, H. A. Schwettman, and T. I. Smith, Phys. Rev. Lett. **36**, 717 (1976).

[113] K. L. Felch, K. O. Busby, R. W. Layman, D. Kapilow, and J. E. Walsh, Appl. Phys. Lett. **38**, 601 (1981).

[114] S. Von Laven, J. Branscum, J. Golub, R. Layman, and J. Walsh, Appl. Phys. Lett. **41**, 408 (1982).

[115] S. J. Smith and E. M. Purcell, Phys. Rev. **92**, 1069 (1953).

[116] J. V. Jelley, Br. J. Appl. Phys. **6**, 227 (1955).

[117] W. W. Salisbury, Science (80-.). **154**, 386 (1966).

[118] M. A. Piestrup, R. A. Powell, G. B. Rothbart, C. K. Chen, and R. H. Pantell, Appl. Phys. Lett. **28**, 92 (1976).

[119] H. G. Kosmahl, Proc. IEEE **70**, 1325 (1982).

[120] J. Urata, M. Goldstein, M. F. Kimmitt, A. Naumov, C. Platt, and J. E. Walsh, Phys. Rev. Lett. **80**, 2 (1998).

[121] F. A. Hopf, P. Meystre, M. O. Scully, and W. H. Louisell, Opt. Commun. **18**, 413 (1976).

[122] M. V. Bashevoy, F. Jonsson, a. V. Krasavin, N. I. Zheludev, Y. Chen, and M. I. Stockman, Nano Lett. **6**, 1113 (2006).

[123] A. Massuda, C. Roques-Carmes, Y. Yang, S. E. Kooi, Y. Yang, C. Murdia, K. K. Berggren, I. Kaminer, and M. Soljačić, ACS Photonics **5**, 3513 (2018).

[124] G. Adamo, K. F. MacDonald, Y. H. Fu, C.-M. Wang, D. P. Tsai, F. J. García de Abajo, and N. I. Zheludev, Phys. Rev. Lett. **103**, 113901 (2009).

[125] G. Adamo, J. Y. Ou, J. A. So, S. D. Jenkins, F. Deaangelis, K. F. MacDonald, E. Diafabrizio, J. Ruostekoski, and N. I. Zheludev, Phys. Rev. Lett. **109**, 1 (2012).

[126] J.-K. So, F. J. García de Abajo, K. F. MacDonald, and N. I. Zheludev, ACS Photonics **2**, 1236 (2015).

[127] G. Li, B. P. Clarke, J.-K. So, K. F. MacDonald, and N. I. Zheludev, Nat. Commun. **7**, 13705 (2016).

[128] L. J. Wong, I. Kaminer, O. Ilic, J. D. Joannopoulos, and M. Soljačić, Nat. Photonics **10**, 46 (2015).

[129] I. Kaminer, Y. T. Katan, H. Buljan, Y. Shen, O. Ilic, J. J. López, L. J. Wong, J. D.

Joannopoulos, and M. Soljačić, Nat. Commun. **7**, ncomms11880 (2016).

[130] F. Liu, L. Xiao, Y. Ye, M. Wang, K. Cui, X. Feng, W. Zhang, and Y. Huang, Nat. Photonics **11**, 289 (2017).

[131] I. Kaminer, S. E. Kooi, R. Shiloh, B. Zhen, Y. Shen, J. J. López, R. Remez, S. A. Skirlo, Y. Yang, J. D. Joannopoulos, A. Arie, and M. Soljacic, Phys. Rev. X **7**, 011003 (2017).

[132] Y. Inoue, H. Hayano, Y. Honda, T. Takatomi, T. Tauchi, J. Urakawa, S. Komamiya, T. Nakamura, T. Sanuki, E. S. Kim, S. H. Shin, and V. Vogel, Phys. Rev. Spec. Top. - Accel. Beams **11**, 062801 (2008).

[133] T. M. Shaffer, E. C. Pratt, and J. Grimm, Nat. Nanotechnol. **12**, 106 (2017).

[134] Y. Fang, R. Verre, L. Shao, P. Nordlander, and M. Käll, Nano Lett. **16**, 5183 (2016).

[135] C. I. Osorio, T. Coenen, B. J. M. M. Brenny, A. Polman, and A. F. Koenderink, ACS Photonics **3**, 147 (2016).

[136] T. Han, S. Zu, Z. Li, M. Jiang, X. Zhu, and Z. Fang, Nano Lett. **18**, 567 (2018).

[137] B. P. Clarke, B. Gholipour, K. F. MacDonald, and N. I. Zheludev, Appl. Phys. Lett. **113**, 241902 (2018).

[138] N. Yu, P. Genevet, M. A. Kats, F. Aieta, J.-P. P. Tetienne, F. Capasso, and Z. Gaburro, Science (80-.). **334**, 333 (2011).

[139] X. Ni, N. K. Emani, A. V. Kildishev, A. Boltasseva, and V. M. Shalaev, Science **335**, 427 (2012).

[140] A. V Kildishev, A. Boltasseva, and V. M. Shalaev, Science (80-.). **339**, 12320091 (2013).

[141] P. Genevet, F. Capasso, F. Aieta, M. Khorasaninejad, and R. Devlin, Optica **4**, 139 (2017).

[142] C. Luo, M. Ibanescu, S. G. Johnson, and J. D. Joannopoulos, Science (80-.). **299**, 368 (2003).

[143] J. R. M. Saavedra, D. Castells-Graells, and F. J. García De Abajo, Phys. Rev. B **94**, 35418 (2016).

[144] R. Remez, N. Shapira, C. Roques-Carmes, R. Tirole, Y. Yang, Y. Lereah, M. Soljačić, I. Kaminer, and A. Arie, Phys. Rev. A **96**, (2017).

[145] G. Rosolen, L. J. Wong, N. Rivera, B. Maes, M. Soljačić, and I. Kaminer, Light Sci. Appl. **7**, 64 (2018).

[146] Z. Wang, K. Yao, M. Chen, H. Chen, and Y. Liu, Phys. Rev. Lett. **117**, 157401 (2016).

[147] J. Verbeeck, H. Tian, and P. Schattschneider, Nature **467**, 301 (2010).

[148] M. Uchida and A. Tonomura, Nature **464**, 737 (2010).

[149] B. J. McMorran, A. Agrawal, I. M. Anderson, A. A. Herzing, H. J. Lezec, J. J. McClelland, and J. Unguris, Science **331**, 192 (2011).

[150] N. Voloch-Bloch, Y. Lereah, Y. Lilach, A. Gover, and A. Arie, Nature **494**, 331 (2013).

[151] R. Shiloh and A. Arie, Ultramicroscopy **177**, 30 (2017).

[152] R. Shiloh, Y. Lereah, Y. Lilach, and A. Arie, Ultramicroscopy **144**, 26 (2014).

[153] J. Verbeeck, A. Béché, K. Müller-Caspary, G. Guzzinati, M. A. Luong, M. Den Hertog, K. Müller-Caspary, M. A. Luong, G. Guzzinati, J. Verbeeck, A. Béché, K. Müller-Caspary, G. Guzzinati, M. A. Luong, and M. Den Hertog, Ultramicroscopy **190**, 58 (2018).

[154] T. R Harvey, J. S Pierce, A. K Agrawal, P. Ercius, M. Linck, and B. J. McMorran, New J. Phys. **16**, 093039 (2014).

[155] V. Grillo, G. Carlo Gazzadi, E. Karimi, E. Mafakheri, R. W. Boyd, and S. Frabboni, Appl. Phys. Lett. **104**, 043109 (2014).

[156] R. Flatabø, M. M. Greve, S. D. Eder, M. Kalläne, A. S. Palau, K. K. Berggren, and B. Holst, J. Vac. Sci. Technol. B, Nanotechnol. Microelectron. Mater. Process. Meas. Phenom. **35**, 06G502 (2017).

[157] B. Brezger, L. Hackermüller, S. Uttenthaler, J. Petschinka, M. Arndt, and A. Zeilinger, Phys. Rev. Lett. **88**, 100404 (2002).

[158] J. Kirz, J. Opt. Soc. Am. **64**, 301 (1974).

[159] J. O. Grepstad, P. Kaspar, O. Solgaard, I.-R. Johansen, and A. S. Sudbø, Opt. Express **20**, 7954 (2012).

[160] I. Vlassiouk, P. Y. Apel, S. N. Dmitriev, K. Healy, and Z. S. Siwy, Proc. Natl. Acad. Sci. U. S. A. **106**, 21039 (2009).

[161] L. Q. Gu and J. W. Shim, Analyst **135**, 441 (2010).

[162] C. B. Carter and D. B. Williams, *Transmission Electron Microscopy: Diffraction, Imaging, and Spectrometry* (2016).

[163] H. Reimer, L, Kohl, *Transmission Electron Microscopy: Physics of Image Formation* (2005).

[164] B. McMorran, J. D. Perreault, T. A. Savas, and A. Cronin, Ultramicroscopy **106**, 356 (2006).

[165] Y. Yang, C.-S. Kim, R. G. Hobbs, P. Kruit, and K. K. Berggren, Phys. Rev. A **98**, 043621 (2018).

[166] F. Hasselbach, Reports Prog. Phys. **73**, 016101 (2010).

[167] A. Tonomura, Rev. Mod. Phys. **59**, 639 (1987).

[168] P. Kruit, R. G. Hobbs, C.-S. C.-S. Kim, Y. Yang, V. R. Manfrinato, J. Hammer, S. Thomas, P. Weber, B. Klopfer, C. Kohstall, T. Juffmann, M. A. Kasevich, P. Hommelhoff, and K. K. Berggren, Ultramicroscopy **164**, 31 (2015).

[169] G. Möllenstedt and H. Düker, Zeitschrift Für Phys. **145**, 377 (1956).

[170] L. Marton, Phys. Rev. **85**, 1057 (1952).

[171] H. Batelaan, Rev. Mod. Phys. **79**, 929 (2007).

[172] G. Gronniger, B. Barwick, H. Batelaan, T. Savas, D. Pritchard, and A. Cronin, Appl. Phys. Lett. **87**, 124104 (2005).

[173] A. Caprez, R. Bach, S. McGregor, and H. Batelaan, J. Phys. B At. Mol. Opt. Phys. **42**, 165503 (2009).

[174] G. Matteucci, G. F. Missiroli, and G. Pozzi, Ultramicroscopy **6**, 109 (1981).

[175] W. P. Putnam and M. F. Yanik, Phys. Rev. A **80**, 040902 (2009).

[176] D. L. Freimund and H. Batelaan, Phys. Rev. Lett. **89**, 283602 (2002).

[177] A. C. Elitzur and L. Vaidman, Found. Phys. **23**, 987 (1993).

[178] P. Kwiat, H. Weinfurter, T. Herzog, A. Zeilinger, and M. A. Kasevich, Phys. Rev. Lett. **74**, 4763 (1995).

[179] D. B. Williams and C. B. Carter, *Transmission Electron Microscopy: A Textbook for Materials Science* (Springer Science & Business Media, 2009).

[180] Z. L. Wang, *Elastic and Inelastic Scattering in Electron Diffraction and Imaging* (2013).

[181] H. A. Haus, *Waves and Fields in Optoelectronics* (Prentice Hall, Incorporated, 1984).

[182] C. B. Chiu, E. C. G. Sudarshan, and B. Misra, Phys. Rev. D **16**, 520 (1977).

[183] T. Nakanishi, K. Yamane, and M. Kitano, Phys. Rev. A **65**, 4 (2001).

[184] R. F. Egerton and T. Edition, *Electron Energy-Loss Spectroscopy in the Electron Microscope* (Springer US, Boston, MA, 2011).

[185] E. Völkl, L. F. Allard, and D. C. Joy, *Introduction to Electron Holography* (Springer US, 1999).

[186] M. Wanner, D. Bach, D. Gerthsen, R. Werner, and B. Tesche, Ultramicroscopy **106**, 341 (2006).

[187] Z. G. Pinsker, *Electron Diffraction* (Butterworths Scientific Publ., 1953).

[188] A. Goswami and N. D. Lisgarten, J. Phys. C Solid State Phys. **13**, 1381 (1980).

[189] D. E. Ashenford and N. D. Lisgarten, Acta Crystallogr. Sect. A **39**, 311 (1983).

[190] D. Alcaraz Iranzo, S. Nanot, E. J. C. Dias, I. Epstein, C. Peng, D. K. Efetov, M. B. Lundeberg, R. Parret, J. Osmond, J.-Y. Hong, J. Kong, D. R. Englund, N. M. R. Peres, and F. H. L. Koppens, Science (80-.). **360**, 291 (2018).

[191] V. Kumar and K.-J. Kim, Phys. Rev. E **73**, 026501 (2006).

[192] H. L. Andrews, C. H. Boulware, C. A. Brau, and J. D. Jarvis, Phys. Rev. Spec. Top. -

Accel. Beams **8**, 110702 (2005).